ALMA MATER STUDIORUM – UNIVERSITÀ DI BOLOGNA

DOTTORATO DI RICERCA IN

GEOFISICA

Ciclo: XXX

Settore Concorsuale di afferenza: 04/A4 - GEOFISICA

Settore Scientifico Disciplinare: GEO/10 – GEOFISICA DELLA TERRA SOLIDA

UNIVERSALITY OF GR B-VALUE GRADIENTS FOR DIFFERENT TECTONIC REGIMES AND INFERENCES ON A DIFFERENTIAL STRESS DEPENDENCE

Presentata da: **ANTONIO PETRUCCELLI**

Coordinatore Dottorato: **PROF.SSA NADIA PINARDI**

Supervisore: **PROF. PAOLO GASPERINI**

Esame finale anno 2018

Abstract

Variations in earthquakes size-distribution (*b*-value) have a central importance in modern seismology. Starting from the late 60's, the possible explanation of such variations has been found into the Earth's crust stress differences, going far from the classical view of a constancy of the *b*-value itself. In fact, stress is the determinant parameter controlling the faulting mechanisms of earthquakes: compressions (thrust faults) accompany higher stresses with respect to extensive (normal faults) mechanisms, with transcurrences (strike-slip faults) in the middle of them. In this thesis, it is showed that earthquakes size-distribution, stress and faulting styles have a clear and straightforward connection both on global and local scale: if the magnitude of *b* is inversely related to differential stress (as confirmed by laboratory experiments), which, in turn, depends on faulting styles, *b*-value is expected to vary systematically. By using classical formulations of Anderson and Mohr-Coulomb, the different behaviors of *b*-value on tectonic styles as due to stress are modeled in new, unreported ways. A sinusoidal behavior of *b*-value on the rake angle of the focal mechanisms is thought to be a good first-order model for expressing the dependence on tectonic style. Moreover, using a ternary scheme of the focal mechanisms, a second-order effect of differential stress on *b*-value for dip-slip mechanisms is detected. Finally, using high-quality local dataset for Southern California, the single dependences of *b* (inverse linearity on depth and separation on faulting styles) are modeled, firstly on their own and then together in a single, universal model, able to be the best explicator of the physical reality. All the analyses shown in this thesis result in a big improvement for supporting the theory of the variations of b connected to stress differences.

Contents

Part 1

INTRODUCTION

This introductory part offers an overview over the main topics and targets of the thesis. It introduces the GR law and the statistical methods for the estimation of M_c and b-value. The issue relative to the variability of frequency-magnitude distribution on different tectonic styles is then exposed through examples from the literature, explained with the Anderson's theory of faulting and with all the stress-based physical interpretations.

1. GR law: b-value and M_c

The Gutenberg and Richter law (now on referred as GR) [*Gutenberg and Richter*, 1944] represents one of the basis of modern seismology. It results in a very simple model describing the occurrence N of earthquakes, within a certain time - space window interval, as a function of magnitude M (red line in Fig. 1.1). It is presented in its common form as log-linear decrease of N with increasing M

$$log\, N(M) = a - bM \tag{1.1}$$

The data visualization is done through the so-called frequency-magnitude distribution (FMD) curve, in which the logarithms of the frequencies for each magnitude bin M are reported. In a FMD plot, two different kinds of data can be distinguished: non-cumulative data (number of occurrences in the $\left[M - \frac{dM}{2}, M + \frac{dM}{2}\right]$ interval, where dM is the bin value, displayed with green circles in Fig. 1.1) and cumulative-data (number of earthquakes occurrences with magnitude $m > M$, displayed as blue triangles in Fig. 1.1).

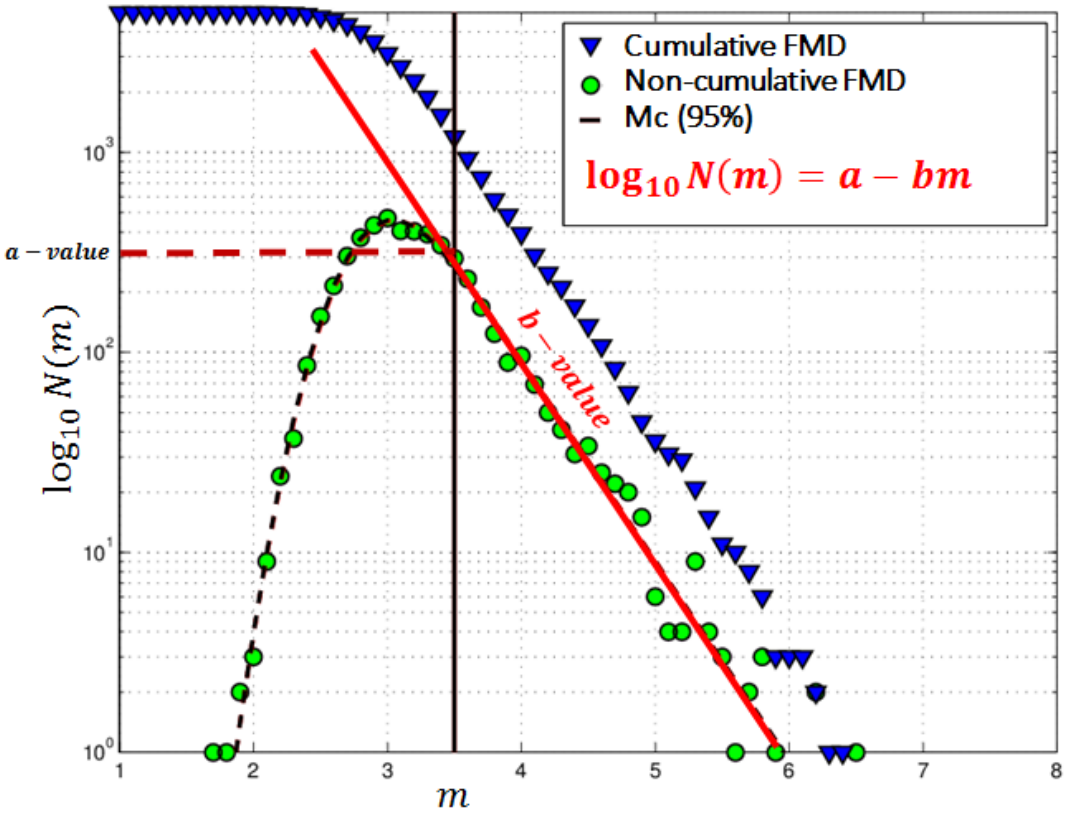

Figure 1.1: FMD (cumulative and non-cumulative) and GR law (red line). Data are synthetic and are generated according to the EMR method (see 1.2). M_c at 95% level is shown with a black vertical line.

The GR law provides useful information about seismic phenomenology. In fact, while constant a in equation (1.1) refers to seismic productivity (rate), b parameter, commonly known as b-value, has important consequences in seismic analyses. In fact, it is the log-linear proportionality constant in the GR model, i.e. the slope of the exponential decay of N with increasing magnitude: its quantification means to establish the proportion of high (low slope) and low (high slope) magnitude events in an earthquake dataset.

1.1 The Maximum Likelihood Estimation method (MLE): analytical and numerical approach

The Maximum Likelihood Method (MLE) is the most common methodology currently used in *b*-value estimations. According to GR model, the MLE probability density function (PDF) of detecting an earthquake of magnitude M [*Aki*, 1965; *Utsu*, 1965] can be written as

$$f(M) = b \log 10 \, \frac{\exp[-bM]}{\exp[-bM_{min}] - \exp[-bM_{max}]} \tag{1.2}$$

Where M_{min} and M_{max} are the minimum and maximum magnitude in the dataset. In most of cases ($M_{max} >> M_{min}$) equation 1.2 reduces to (see Appendix A)

$$f(M|\, b) \approx b \log 10 \exp\,[-b(M - M_{min})] \tag{1.3}$$

Given a set of magnitude observation, function f is the PDF assumed for those observations with that *b*-value. The Loglikelihood function $L(\theta)$, where θ variable refers to k possible parameters in a statistical model, is defined as the natural logarithm of the product of the individual likelihoods f of i statistically independent observations ($i = 1, \dots, N$)

$$L(\theta) = \log\left\{\prod_{i=1}^{N} f_i\right\} = \sum_{i=1}^{N} \log\{f_i\} \tag{1.4}$$

The MLE approach consists in choosing the optimal parameter θ which maximizes L [*Fisher*, 1950]. In our specific case, we are interested in the optimal *b*-value which maximize the L function, given a set of magnitudes. The analytical solution to our problem is provided by the formula of *Aki* [1965] (analytically derived in Appendix A, eq. A10)

$$b = \frac{1}{\log 10\,[\bar{M} - M_{min}]}$$

where $\bar{M}$ is the mean magnitude of the dataset. Since *Aki* [1965] assumes a continuum of earthquake magnitudes, the use of binned magnitudes in FMD introduces a correction term $-\frac{\Delta M}{2}$ in the original formula [*Bender*, 1983], if ΔM represents the magnitude binning, otherwise results would be biased

$$b = \frac{1}{\log 10\,\left[\bar{M} - \left(M_{min} - \frac{\Delta M}{2}\right)\right]} \tag{1.5}$$

Equation (1.5) is widely used in statistical seismology. Although the exact statistical distribution of *b*-values derived by *Utsu* [1966] is asymmetrical, it tends to the Normal distribution for large samples [*Aki*, 1965; *Shi and Bolt*, 1982]. In fact, the standard error associated by *Aki* [1965] was $\sigma_b = \frac{b}{\sqrt{N}}$, but it is of common practice to use the estimation provided by *Shi and Bolt* [1982]

$$\sigma_b = 2.30 b^2 \sqrt{\frac{\sum_{i=1}^{N}(M_i - \bar{M})^2}{N(N-1)}} \tag{1.6}$$

Nevertheless, the MLE technique assumes as hypothesis both that the FMD follows an exponential decay model with the magnitude and that the maximum magnitude value is at infinity (more likely is that the dataset on which the b-value is being estimated is not large enough to sample the maximum magnitude). However, the success of the analytical computation of b does not imply that the data itself is exponentially distributed. The application of equation 1.5, indeed, requests that the data we are dealing with are effectively described by an exponential model. The alternative route that one might take is to try to numerically maximize equation (1.4), which means that we are interested in finding the optimal b-value $\hat{b}$ by minimizing the sign-reversed Loglikelihood function

$$L(\hat{b}) = \max\{L(b)\} = \min\{-L(b)\} \tag{1.7}$$

1.2 Magnitude of completeness: modeling and technique overview

As clear from Figure 1.1, the validity of GR model (red line) is not extended to the entire magnitude range. In fact, in proximity of lower magnitude values, the GR line starts departing from data distribution, as if indicating that some events were "missing" according to the model. This part of the dataset is defined *incomplete* according to GR, while the other one, for which the linear decay of the GR holds, is defined *complete*. Magnitude of completeness M_c is the threshold magnitude that separates these two parts of the distribution. It is physically defined as the magnitude threshold for which there is a certain sureness (completeness) level to detect earthquakes in a spatio-temporal domain [*Rydelek and Sacks*, 1989; *Taylor et al.*, 1990; *Wiemer and Wyss*, 2000].

The overall seismicity rate (a-value) and the b-value are used in seismic hazard studies [*Wiemer et al.*, 2009] and in developing earthquake forecast models [*Wiemer and Schorlemmer*, 2007]. Moreover, as shown in this thesis, b-value can be used to interpret and understand the properties and the physics of the Earth's crust. GR model can be applied only to the complete part of the dataset. Hence, equation (1.5) can be rewritten as

$$b = \frac{1}{\log 10 \left[\bar{M} - \left(M_c - \frac{\Delta M}{2}\right)\right]} \qquad M \geq M_c \tag{1.8}$$

The choice of an appropriate M_c has a direct impact on the evaluation of GR parameters: in fact, for $M < M_c$, the b-value is underestimated because the GR model wouldn't fit the data. For $M \geq M_c$ the b-value is instead stable (in most cases around 1.0) before fluctuating at higher magnitudes as events occurrence reduces drastically. Compared to the complete part of the dataset, well described by the GR model, the incomplete part modeling is not so straightforward. According to *Ringdal* [1975] and *Ogata and Katsura* [1993; 2006], the incompleteness of the catalog can be modeled by a cumulative Gaussian function $q(m|\xi,\sigma)$ with parameters ξ and σ representing the magnitude (median) corresponding to which the detectability level is 50% and the standard deviation within which earthquakes are partially detected respectively. In this sense, completeness levels are defined as $M_c = \xi + j\sigma$ (with integer j): increases in j determine an increase in magnitudes detection level. This method, called Entire Magnitude Range (EMR) by *Mignan and Woessner* [2012], tries to reproduce the entire magnitude domain on the basis of the fit of the complete and incomplete parts contemporary (see Fig. 1.1). The corresponding PDF is reported as a solid black line in Fig 1.1 and it

is used to generate the synthetic data. EMR method seems to provide an overall complete FMD model. However, it has the disadvantages to make assumptions beneath the completeness thresholds, where sometimes significant variations are reported [*Kagan*, 2002a, 2002b], and to obtain simultaneous estimations on three different parameters [*Mignan and Woessner*, 2012]. However, different modeling approaches can be used for the incomplete part of the FMD, like for example a triangular FMD shape [*Mignan*, 2012].

The wider M_c estimation method currently used, because of its computational fastness, is the Maximum Curvature method [*Wyss et al.*, 1999; *Wiemer and Wyss*, 2000]. It defines the point of maximum curvature by computing the maximum value of the first derivative of the frequency-magnitude curve. In practice, this matches the magnitude bin with the highest frequency of events in the non-cumulative FMD. However, in absence of a corrective term on M_c (typically of one or two bins) this method might provide underestimations in b-values. After having been tested it properly, this method has been used for several elaborations on Global CMT catalog (see Section 6.1 and Part 2) in this thesis.

Another method used in the context of the thesis (see Part 3) is the Mc-to-B-value-Stability [MBS], firstly proposed by *Cao and Gao* [2002]. It estimates M_c using the stability of the b-value as a function of a cutoff magnitude M_{c_o}. As M_{c_o} approaches the true M_c, the b-value approaches its true value and remains constant, forming a plateau.

Other several methods have been developed [*Wiemer and Wyss*, 2000; *Amorese*, 2007] and, currently, no one is to prefer with respect to the others. All such M_c estimation techniques are equally valid. They only have to be used carefully in order to avoid incompleteness effects that can somehow affect b-value behavior.

1.3 Magnitude of completeness: spatio-temporal variations

In this thesis, we will refer to M_c always in a "GR model" sense, as explained above. Completeness can also be assessed from a network detection perspective, not defining the completeness level of the dataset but defining the probability level with which an earthquake can be detected on the basis of the single station properties, like the PMC method by *Schorlemmer and Woessner* [2008] and others. In fact, an important challenge for modern seismology is to assess possible spatiotemporal variations in M_c [*Wiemer and Wyss*, 2000].

Temporal changes in M_c origin from the evolution of the seismic network or due to transient changes (like aftershock sequences or swarm activities). Changes in seismic networks often correspond to the addition of new stations, so a decrease in M_c should be expected [*Hutton et al.*, 2010]. Transitional phases in a network are usually identified by shifts in M_c, while aftershocks sequences determine larger fluctuations in M_c. If the events are too small to be detected with respect to larger events (as happens within the coda of a mainshock), M_c increases.

Spatial variations in M_c consist in estimating a $M_c(x, y)$ from events located in fixed volumes centered on each node of a spatial grid [*Wyss et al.*, 1999; *Wiemer and Wyss*, 2000]. In each box, some criterion should be established (on size or on number of events) for avoiding unstable M_c results: for

example, if we choose cylindrical volumes, the radius R mush be large enough to have sufficient number of nodes but small enough to avoid over-smoothing. This mapping approach is widely used on regular grid points [*Woessner and Wiemer*, 2005; *Hutton et al.*, 2010; *Schorlemmer et al.*, 2010a, *Nanjo et al.*, 2010a; *Mignan et al.*, 2011; *Thormann et al.*, 2012; 2015].

2. Anderson theory of faulting and tectonic styles

2.1 The tectonic regimes: normal, thrust and strike-slip faults

Anderson [1905] developed the modern basic concepts for the origin of faulting events, emphasizing their important role for seismotectonic. His key role was in recognizing that faults result from brittle fractures for which Coulomb-criterion and Amonton law can be applied: when the stress applied on a fault reaches a critical value, the fault slips giving rise to an earthquake. Earthquakes are displayed as displacements on conjugate surfaces (Fig. 1.2). In a xyz reference system, such surfaces, known as fault planes, origin at angles (depending on friction properties) from minimum/maximum principal directions. By applying the conditions that faulting occurs near the Earth's surface and that one of the principal stresses is vertical (and equal to the lithospheric pressure), three major classes of faults can be defined: *normal* faults, *reverse* faults and *strike-slip* faults. Each kind of faults corresponds to a specific *faulting style*. Normal faulting (NR) accommodates horizontal *extensional* strain. Normal faulting occurs for example along oceanic ridges, when new lithosphere is created, or in continental rift valleys, where lithosphere is instead stretched. Reverse faulting (TH) accommodates horizontal *compressional* stress. Thrust faulting occurs in subduction zones, when oceanic lithosphere thrusts underneath the continental one, or during compressions in continental collisions. Both normal and thrust faults are known as *dip-slip* faults, because displacement takes place along a dipping fault plane at an angle β to the horizontal. In absence of friction, "pure" dip-slip faults dip at 45° from the horizontal, while the presence of friction increases and decreases β for normal and thrust faults respectively (see 2.3).

Along a strike-slip fault (SS) the displacement is instead strictly horizontal: the state of stress consists of a vertical lithostatic stress and horizontal tectonic stresses $\Delta\sigma$ that are compressional in one direction and extensional in the other one, inclined of an angle Ψ with respect to the principal stress directions. Strike-slip are also known *transcurrent* (or *transform*) faults, as the San Andreas Fault in California or faults dislocating sections of oceanic ridges respectively.

Earthquakes that results from such schemes produce a four-lobes radiation pattern that can be determined by a variety of seismological techniques, that are called *focal mechanisms* (or *fault plane solutions*) (now on FM). These provide the seismic moment tensor, representing all the possible orientations of the double-couple of forces originating the earthquake. The four lobes are subdivided by the two conjugate surfaces (nodal planes), one of which corresponds to the *real* fault plane (principal plane) while the other one (auxiliary plane) corresponds to a plane where the slip could have been occurred (but had not) and has the real slip versor as its normal versor. From the focal mechanism alone, it is impossible to determine the real fault plane among the two possibilities, if no

extra information (geological setting, aftershock distribution, …) is known. This ambiguity is crucial in the interpretation of the focal mechanisms.

2.2 Rake angle λ representation for faulting styles

The orientation of a fault is defined by a set of two angles: the *strike* φ, or the azimuth (measured counterclockwise) of the fault respect to the North direction and the *dip* β, or the angle (measured on the vertical plane) between the horizontal plane and fault plane. A third angle, the *rake* λ (measured on the fault plane), gives the direction of the slip vector d, indicating the movement of the hanging-wall with respect to the foot-wall (Fig 1.3). Rake angles allow for a unique definition of the tectonic style:

- λ of 90° indicates "pure" inverse mechanisms (thrust faulting / compressive regime);
- λ of -90° indicates "pure" direct mechanisms (normal faulting / extensive regime);
- λ of 0° and $\pm$180° indicate "pure" transcurrent mechanisms (strike-slip faulting / transcurrent regime), left and right lateral respectively.

Anderson [1905]'s theory of faulting predicts that faults are optimally oriented within the stress field. Furthermore, if we assume that crust is pervaded with faults of any direction, only optimally oriented faults should be active, as suggested by laboratory experiments [*Byerlee*, 1978]. In fact, it is generally accepted that crustal earthquakes are caused by sudden movements on preexisting faults. A common assumption, for fault modeling, is that, during slip, fault orientation remains unchanged and fixed in the space respect to the principal axes directions. However, fault slip (and rake as well) may change, sometimes dramatically, giving rise to unfavorably fault oriented faults.

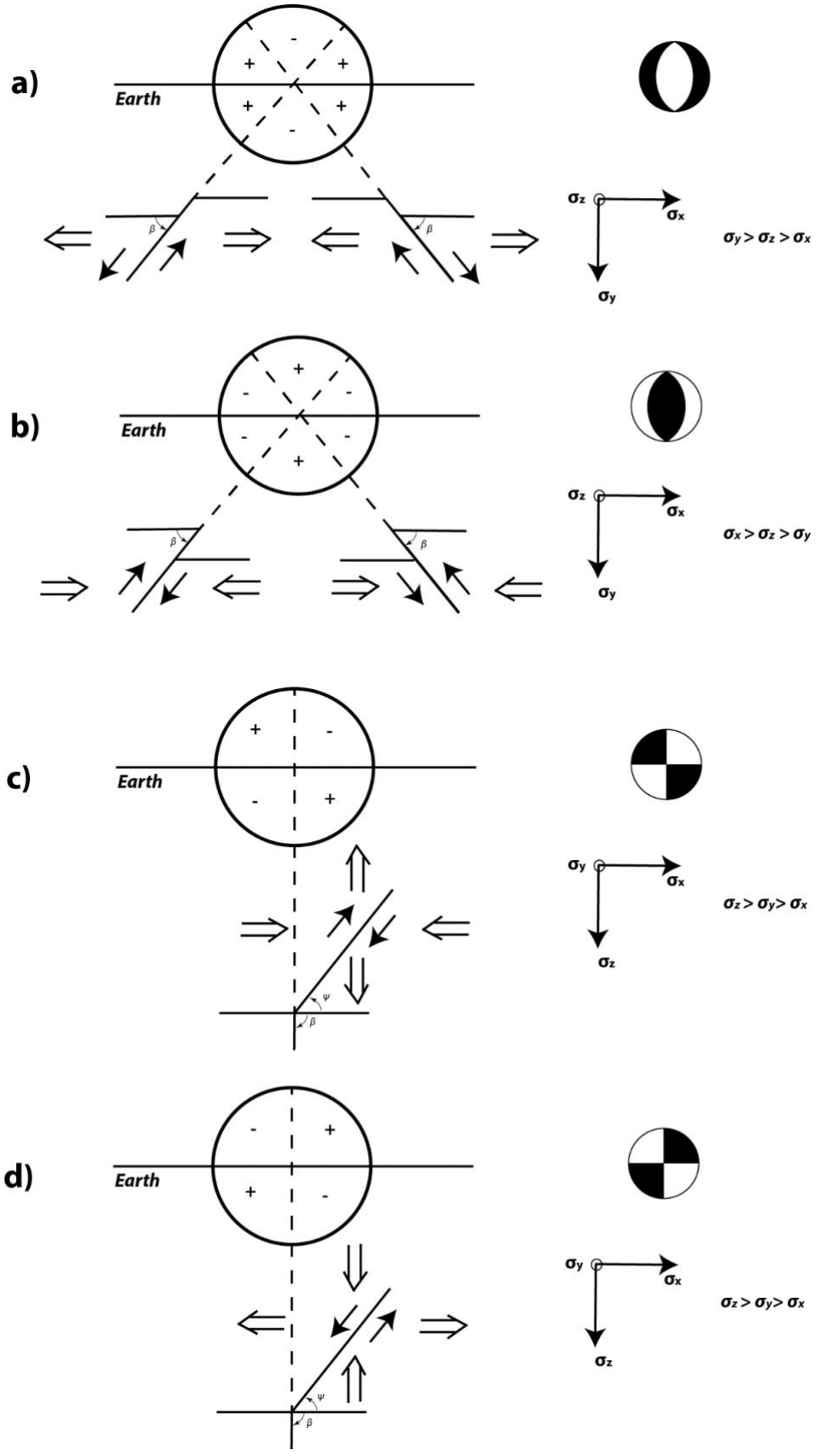

Figure 1.2: Anderson faulting styles, principal axes orientations and focal mechanisms. a) Normal faulting and b) Thrust faulting: the two conjugate dip-slip faults dip with an angle β. **Right (c) and left (d) lateral strike-slip faulting:** the two conjugate faults are inclined with an angle Ψ to the direction of the principal stress σ_x.

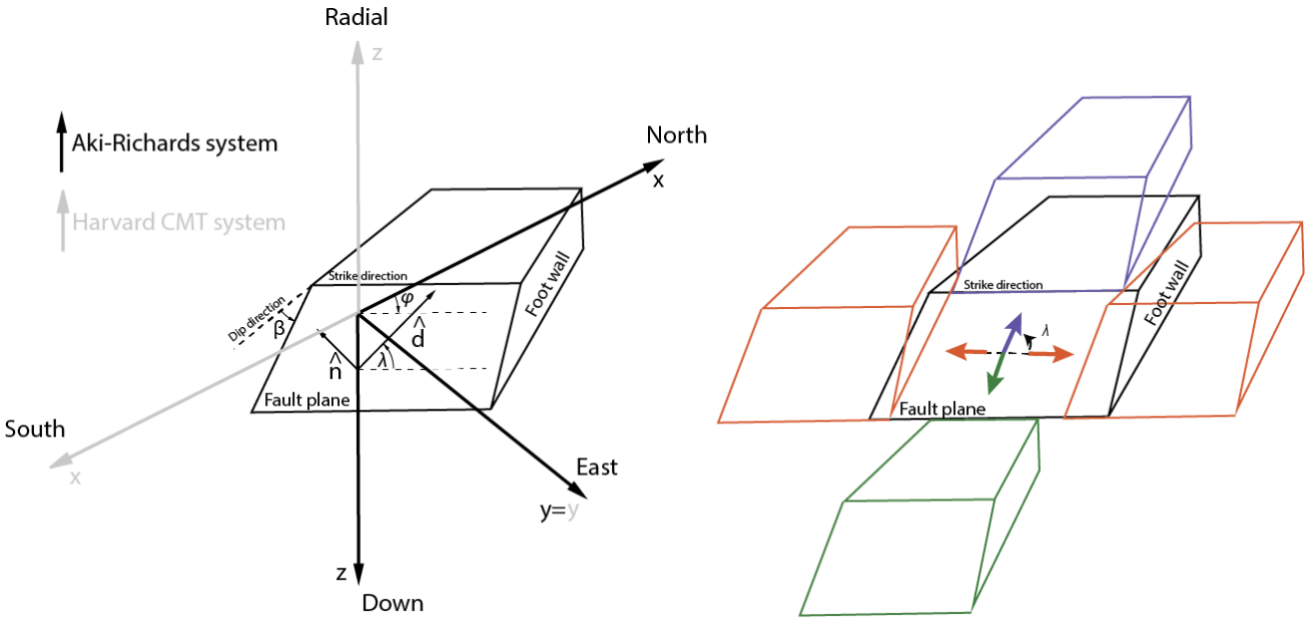

Figure 1.3: Anderson faulting scheme. a) Strike, dip and rake definition and b) tectonic styles definition according to rake angle λ: colored boxes (green for normal, blue for thrust and red for strike-slip) denote hanging walls moving respect to foot wall, according to respective arrows.

2.3 Anderson's theory of faulting: the differential stress $\sigma_1 - \sigma_3$

Anderson [1905]'s faulting schemes of Fig. 1.2 assumes that both the horizontal stresses (σ_x and σ_z) both the vertical stress σ_y are principal stresses, $\{\sigma_1, \sigma_2, \sigma_3\}$, where σ_1 refers to the maximum eigenvalue and σ_3 to the minimum one. The vertical stress σ_y is always assumed as the lithospheric pressure $\rho g y$ (where ρ is the rock density, g is the gravity and y is the depth) while the horizontal stresses result in a perturbation of the lithostatic pressure by the tectonic stress $\Delta\sigma$. The difference (always positive) $\sigma_1 - \sigma_3$ is called *differential stress* and quantifies the stress accumulation around the source. For dip-slip faults (normal and thrust faulting styles) the state-stress can be expressed as

$$\begin{aligned} \sigma_x &= \rho g y \pm \Delta\sigma \\ \sigma_y &= \rho g y \\ \sigma_z &= \rho g y \pm \nu\Delta\sigma \end{aligned} \tag{1.9}$$

The *upper* sign (+) applies to *thrust* faults, which exceed the vertical lithostatic stress in one horizontal direction, while the *lower* sign (-) applies to *normal* faults, which suffer a stress decrease in one horizontal direction. The stress on the other horizontal direction σ_z is always compressional/extensional but its magnitude is scaled by a factor $\nu \approx 0.25$.

As anticipated before, slip faulting occurs when shear stress τ overcomes a static frictional value. For Earth's crust, it is experimentally found that

$$|\tau| = \mu\sigma_n \tag{1.10}$$

where μ is the friction coefficient and σ_n is the normal stress acting on the fault. This relation is also known as Amonton's law: the greater the normal stress, the harder to initiate sliding. The presence of fluids affects the frictional behavior of faults decreasing the effective normal stress. By referring to the pressure of water as $p_w = \rho_w g y$, Amonton's law can be corrected as

$$|\tau| = \mu(\sigma_n - p_w) \tag{1.11}$$

Normal stress and shear stress can be written as a function of σ_x, σ_y and $\theta = \frac{\pi}{2} - \beta$ (β-complementary angle, see *Turcotte and Schubert* [2002]), and using equations (1.9)

$$\begin{aligned} \sigma_n &= \frac{1}{2}(\sigma_x + \sigma_y) + \frac{1}{2}(\sigma_y - \sigma_x)\cos 2\theta = \rho g y \pm \frac{\Delta\sigma}{2}(1 + \cos 2\theta) \\ \tau &= -\frac{1}{2}(\sigma_x - \sigma_y)\sin 2\theta = \mp\frac{\Delta\sigma}{2}\sin 2\theta \end{aligned} \tag{1.12}$$

By inserting such expressions in the Amonton's corrected law, we obtain an expression for the dip-slip tectonic stress

$$|\Delta\sigma_{dip-slip}| = \frac{2\mu(\rho - \rho_w)gy}{|\sin 2\theta| \mp \mu(1 + \cos 2\theta)} \tag{1.13}$$

For strike-slip faulting, the state of stress describes horizontal motion in the xy plane and σ_z is the lithospheric load

$$\begin{aligned} \sigma_x &= \rho g y + \frac{\Delta\sigma}{2} \\ \sigma_y &= \rho g y - \frac{\Delta\sigma}{2} \\ \sigma_z &= \rho g y \end{aligned} \tag{1.14}$$

Hence the normal and shear stresses are

$$\begin{aligned} \sigma_n &= \frac{1}{2}(\sigma_x + \sigma_y) + \frac{1}{2}(\sigma_y - \sigma_x)\cos 2\psi = \rho g y - \frac{\Delta\sigma}{2}\cos 2\psi \\ \tau &= -\frac{1}{2}(\sigma_x - \sigma_y)\sin 2\psi = -\frac{\Delta\sigma}{2}\sin 2\psi \end{aligned} \tag{1.15}$$

So, the strike-slip tectonic stress results

$$|\Delta\sigma_{strike-slip}| = \frac{2\mu(\rho - \rho_w)gy}{|\sin 2\psi| + \mu\cos 2\psi} \tag{1.16}$$

In Fig. 1.4 the dependence of the tectonic stresses for dip-slip (normal and thrust reported in green and blue respectively) and for strike-slip (reported in red) on the friction coefficient are showed. Anderson's theory argues then that normal faulting is accompanied by lower stresses with respect to thrust faulting, which requires higher stresses. Strike-slip regimes lies in the middle between them. Deeper analytical details can be found in Appendix C.

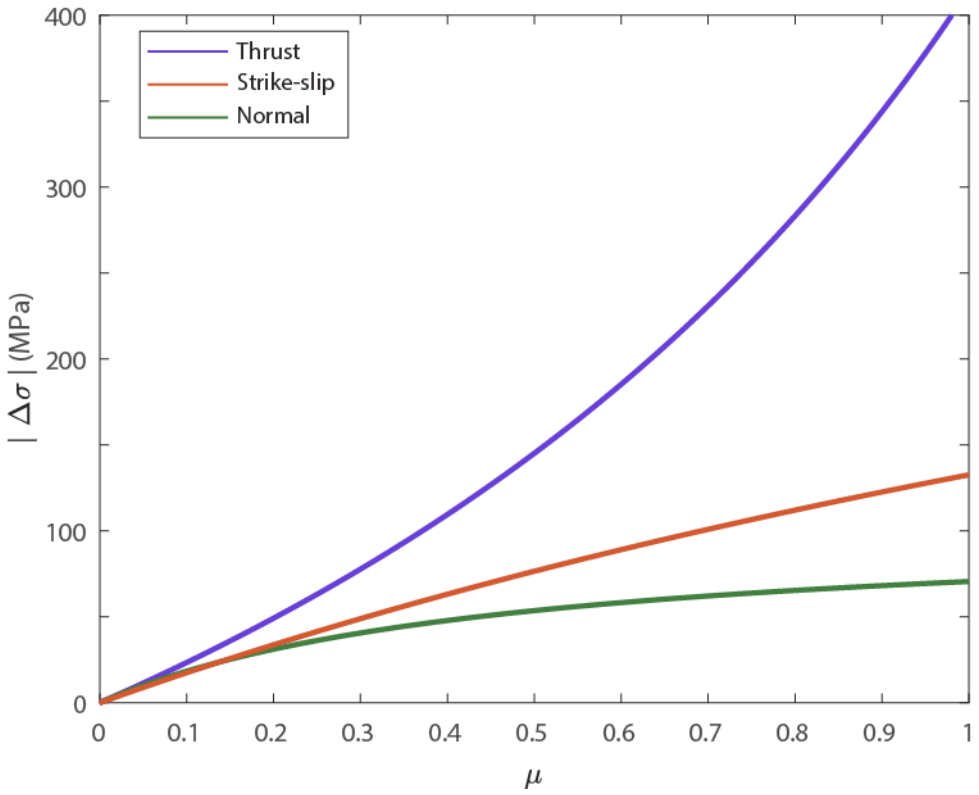

Figure 1.4: Anderson tectonic stresses as function of the static friction coefficient of the crust for different tectonic regimes: $p_w = \rho_w g y$, $\rho = 2700 \frac{kg}{m^3}$, $\rho w = 1000 \frac{kg}{m^3}$, $g = 10 \frac{m}{s^2}$, $y = 5000\ m$, $\theta_{norm} = 24.8°$, $\theta_{thr} = 65.2°$, $\psi = 35°$ (see *Turcotte and Schubert* [2002]).

By hypothesizing that crust is pervaded by preexisting faults with different dip angles, one of them could reactive as soon as the tectonic stress satisfies Amonton's condition. Then, dip–slip/strike-slip faulting events happen at angles θ or ψ which require the minimum value of the tectonic stress $|\Delta\sigma|$, i.e. if $\frac{d|\Delta\sigma|}{d\theta} = 0$ or $\frac{d|\Delta\sigma|}{d\psi} = 0$. The geometrical conditions are

$$\tan 2\beta = \pm\frac{1}{\mu}$$
$$\tan 2\psi = \mp\frac{1}{\mu} \tag{1.17}$$

The first condition applies to dip-slip faults (upper sign refers to thrust while lower sign refers to normal ones). The second condition applied to strike-slip faults (upper sign refers to left strike-slip while lower sign refers to right strike-slip). Thrust faults dip less than normal faults (Fig. 1.5). Moreover, there is no effect on dipping of strike-slip since the motion in this case is purely horizontal.

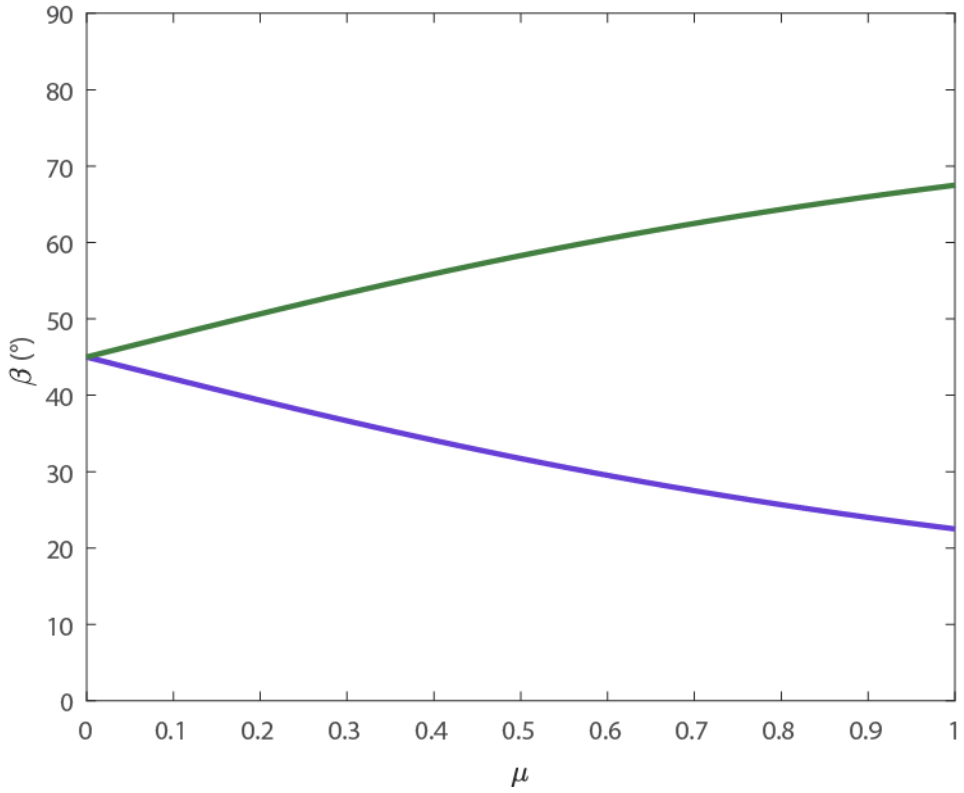

Figure 1.5: Anderson dip angles as function of the static friction coefficient of the crust for dip-slip faults: green line indicates normal faulting ($\beta = \frac{1}{2}\left(\pi - atan\frac{1}{\mu}\right)$) solution, blue line indicated thrust faulting $\left(\beta = \frac{1}{2}atan\frac{1}{\mu}\right)$ solution.

The shear stress represents the anisotropic part of the stress tensor, which is responsible of the shear stresses and of the deformations. In absolute value, for dip-slip faults

$$|\tau_{dip-slip}| = |-\frac{1}{2}(\sigma_x - \sigma_y)\sin 2\theta| \approx \frac{1}{2}(\sigma_1 - \sigma_3) \tag{1.18}$$

The shear stress can be expressed through $\sigma_1 - \sigma_3$, if we assume that the vertical stress σ_y is equal to σ_1 for normal faults (and $\sigma_x = \sigma_3 < \sigma_1$) and equal to σ_3 for thrust faults (and $\sigma_x = \sigma_1 > \sigma_3$). The differential stress is then a reasonable estimate of the shear stress, and as a reasonable approximation for the stress state around the source volume. The same comes from strike-slip equation

$$|\tau_{strike-slip}| = |-\frac{1}{2}(\sigma_x - \sigma_y)\sin 2\psi| \approx \frac{1}{2}(\sigma_1 - \sigma_3) \tag{1.19}$$

since in both cases (left or right strike-slip faulting) the principal stresses σ_1 and σ_3 are horizontals. Remarking, according to Anderson's theory, thrust faults have higher differential stresses and low dip angles, normal faults have lower differential stresses and high dip angles, while strike-slip faults lie in the middle and are not affected by dipping, because the motion is purely horizontal.

2.4 PTB axes representation of the focal mechanisms: the triangular diagram

The focal mechanism results in the graphical expression of the seismic moment tensor, which represents the equivalent forces system acting on a point seismic source (double-couple model). In this configuration, the seismic moment tensor is symmetric on a three-dimensional space with 6 independent components. The most used representation for displaying it is the stereographic projection, or "beach-ball" (Fig. 1.6): the two nodal planes (Plane 1 and Plane 2) separate the observed positive polarities from the negative ones into four quadrants. The seismic moment tensor can be defined also by the orientation of its principal axes (eigenvectors) P, B, T and by its magnitudes (eigenvalues). The P-axis describes the highest eigenvalue, the T-axis the lowest one and the B-axis the intermediate-one. In the stereographic representation, the T-axis is the extensive quadrant and it indicates the direction of minimum compression (maximum extension) while the P-axis is in the compressive quadrant and it indicates the direction of maximum compression (minimum extension). The null axis B lies in correspondence of the intersection of the two nodal planes. Both P and T axes point at 45° direction from the nodal planes (dotted line in Fig. 1.6).

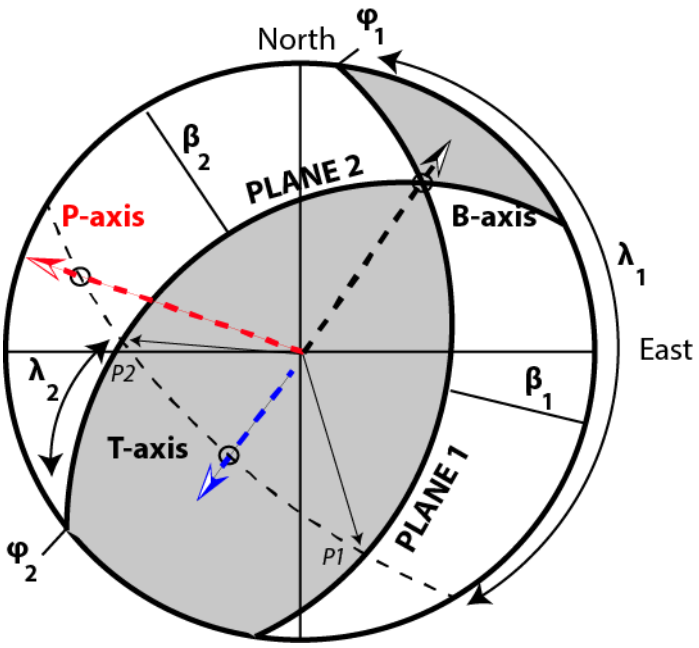

Figure 1.6: Focal sphere plot on a stereographic projection (lower hemisphere). Re-adapted from *Alvarez* [2014]. Strike angle φ_1 defines the positions of one possible plane (1) with respect to North direction. Such plane dips at an angle β_1 with respect to the maximum dip direction. The slip versor direction (p_1) indicates the rake angle λ_1 (computed with respect to strike φ_1). The alternative plane (2) is perpendicular to the first one, since it has the as slip vector direction (p_2) the normal to the first plane.

Each of the moment tensor principal axes P, T, B is located in space through two angles: its azimuth (*trend* η, from 0° to 360°) with respect to North, and its *plunge* δ (from 0° to 90°), the dip with respect to the horizontal direction. The focal mechanisms can also be displayed as function of P, T, B axes. *Fröhlich* [1992, 2001] and *Fröhlich and Apperson* [1992] developed a ternary diagram to represent focal mechanisms into a plunge-angles space domain $[\delta_P, \delta_T, \delta_B]$. A vector $\vec{v}$ of this space has components $[\sin\delta_P, \sin\delta_T, \sin\delta_B]$ and, since the PTB are mutually orthogonal, the relation

$$sin^2\,\delta_P + sin^2\,\delta_T + sin^2\,\delta_B = 1 \qquad (1.20)$$

holds.

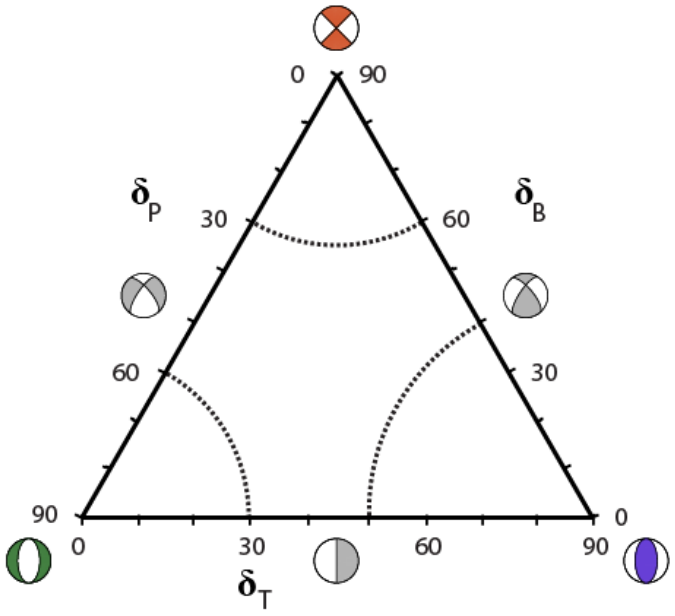

Figure 1.7: Focal mechanisms ternary plot. Dotted black lines delineate "pure" styles branch according to *Fröhlich* [1992] classification.

A planar representation of (1.20) provides a triangular diagram (Fig. 1.7). Each point (single focal mechanism) of the diagram is univocally identified by a tern of plunge angles $[\sin\delta_{P_0}, \sin\delta_{T_0}, \sin\delta_{B_0}]$. Each vertex of the diagram corresponds to a tectonic style: recalling what said before, "pure" reverse and normal faulting have as vertical axes T and P respectively, i. e. δ_T and δ_P are near 90°. Strike-slip mechanisms accompany horizontal deformation, so the vertical axis is B and δ_B is near 90°.

Advantages in using this representation are the focal mechanisms unicity, simplicity and straightforward visualization of the tectonic style, clustering information of earthquakes with similar mechanism, and, most of all, the guaranty of avoiding possible mistakes in the detection of the real fault plane for an earthquake.

According to *Fröhlich* [1992], in the ternary diagram the tectonic styles "branches" are defined as follow:

- *normal faulting*: mechanisms for which $\delta_P \geq 60°$;

- *thrust faulting*: mechanisms for which $\delta_T \geq 50°$;

- *strike-slip faulting*: mechanisms for which $\delta_B \geq 60°$.

These choices leave parts of the diagram outside the classification: the mechanisms are classified as "*odd*" resulting from combinations of two tectonic styles.

2.5 Anderson's faulting conditions in focal mechanisms triangular representation

Apart from nodal planes ambiguity, another uncertainty arises when P and T axes are tried to be related to the maximum and minimum stress directions, i.e. to σ_1 and σ_3. This would be correct only if the stress-drop tensor is the same as the stress tensor. Moreover, P and B axes lie at 45° to the fault plane, which is not the correct direction for Coulomb failure criterion $|\tau| = S_0 + \mu\sigma_n$, motion is assumed to be resisted by a frictional type force whose magnitude equal the normal stress and by an internal cohesive force of the material S_0. The Coulomb failure criterion represents a straight line in the $\{\sigma, \tau\}$ space: the coefficient of internal friction μ is related to the angle of internal friction f_0 by the relation $\mu = \tan f_0$. Faulting occurs along the most favorably plane when the applied stress reaches the Coulomb rupture criterion: this requires a stress difference threshold $\sigma_1 - \sigma_3$ to be reached. Then, there is a wide range of possible orientations for σ_1 and σ_3, depending on the friction properties of the medium [*McKenzie*, 1969]. In fact, stress must change both in orientation and magnitudes if we relax the assumption that fault orientation remains unchanged and fixed in the space respect to the principal axes directions. In case of slip on optimally oriented faults with a typical friction angle f_0 of 30°, the principal stress directions are deduced from the P, T, B axes directions by a rotation of $\frac{f_0}{2} = 15°$ around the B axes [*Raleigh et al.*, 1972; *Cèlérier*, 1988; 2008] (Fig. 1.8). Under these conditions, together with *Anderson* [1905]'s assumptions, the PTB axes directions can be considered a reasonable estimate of principal stress directions, if an error of 15° is admitted [*Cèlérier*, 2010]. With this approximation, two dip angles ω_1 and ω_2 of the maximum/minimum principal stress directions can be defined

$$\omega_{1,2} = \frac{\pi}{4} \pm \frac{f_0}{2} \tag{1.21}$$

(for dip-slip faults, while this has no effect for the strike-slip faults). With a typical value of f_0=30° two values are inferred $\omega_{1,2} = 60°, 30°$. *Anderson* [1905]'s faulting styles are therefore to be expected in plunges of the P and T axes of $\delta_P, \delta_T \approx \frac{\pi}{2} - \frac{f_0}{2} = 75°$ (along the lower bottom in Fig. 1.7), in case of normal and reverse faulting, and not where nodal planes dipping is 45° (nearby the normal and thrust vertices).

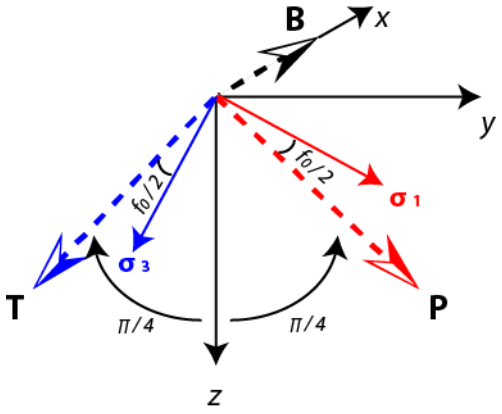

Figure 1.8: PTB axes and principal stress directions. (σ_2 direction coincides with B direction)

2.6 Focal mechanisms quantification: the Kostrov method

In addition to seismic moment geometry, also the magnitude of seismic moment can be considered for estimating the contribution of each mechanism to the deformation. If we consider a volume V within which N moment tensors are included, we can compute the strain rates inside V by summing the 6 independent components of single moments occurring within a certain time T according to the *Kostrov* [1974] formula

$$\dot{\epsilon}_{ij} = \frac{1}{2\mu VT}\sum_{k=1}^{N} m_{ij}^{k} \tag{1.22}$$

Consequently, the total brittle strain [*Scholz and Cowie*, 1990] can be quantified as

$$\epsilon_{ij} = \frac{1}{2\mu V}\sum_{k=1}^{N} m_{ij}^{k} \tag{1.23}$$

Since earthquake-size distribution and fault dimensions are both power laws, the moment summation favors the few largest members of the population in respect to the many littlest ones [*Brune*, 1968; *Scholz and Cowie*, 1990]. *Kostrov* [1974] moments summation method has been demonstrated to represent a valuable way to map and synthesize the kinematic properties of a given area [*Jackson and McKenzie*, 1988; *Ekström and England*, 1989; *Westaway*, 1992; *Pondrelli et al.*, 1995; *Vannucci et al.*, 2004].

3. The b-value variability issue

3.1 A constant or variable b-value?

The importance of studying FMD and b-value lies in providing the relative proportion of small and big earthquakes. Previously, it has been reported that the b-value of the GR law is near to the unity. Nevertheless, despite some oppositions [*Kagan*, 1999; *Bird and Kagan*, 2004; others] claiming of the constancy of such parameter, it is widely reported in literature that b-value can suffer fluctuations. It is true that over large areas and large time periods, b-value is close to one in most cases, but significant variations are documented in limited areas and over shorter time intervals. Little variations for the b-value parameter could provide great changes in projected numbers of earthquakes. Before going on, it is reasonable analyze both sides of view.

Kagan [1999, 2002a, 2005, 2010] argues about universality of the seismic moment-frequency relation

$$N(m) \propto m^{-b^*} \tag{1.24}$$

which is a transformation of GR relation, with slope $b^* = \frac{2}{3}b \approx 0.66$. He documented worldwide constant b^*-values of about 0.6 for shallow, intermediate and deep mainshocks in compressive tectonic environments. Then, reported regional differences are to be attributed to:

- random fluctuations due to an insufficient number of earthquakes in some seismic zones (mid-oceanic ridges b^*-values are unsuitable for determining size-distributions);
- systematic errors bias the b^*-values estimates, such as insufficient knowledge of Earth's structure, non-uniform distribution of seismic stations, biases in magnitude detection techniques, variable cut-off magnitudes in different areas.

Bird and Kagan [2004] used a *tapered* GR model (see Appendix A) [*Jackson and Kagan*, 1999; *Kagan and Jackson*, 2000, *Kagan*, 2002a and others] for studying the seismicity along a global plate boundary model [*Bird*, 2003]. The GR tapered can be written as

$$N(m, m_T, m_c, b^*) = \left(\frac{m}{m_T}\right)^{-b^*} \exp\left[\frac{m_T - m_0}{m_c}\right] \tag{1.25}$$

where N is the fraction of earthquake exceeding moment m, m_T is the threshold moment for the completeness of the catalog and m_c is the corner moment, above which earthquakes become unlikely. The first term $\left(\frac{m}{m_T}\right)^{-b^*}$ is equivalent to the simple cumulative GR while the second (the taper) provides reduction in frequency of very large earthquakes $\lim_{m_c \to +\infty} \exp\left(\frac{m_T - m}{m_c}\right) = 0$.

According to *Kagan* [2002a] the usage of classical GR law should be limited to small to medium earthquake datasets, while it becomes unsuitable for higher magnitudes, for which the corner magnitude must be considered. *Kagan* [2004] found b^*-values consistent with a common value of 0.61- 0.66 ($b \approx 0.9 - 1.0$), within a confidence interval of 95%. Outside this range, higher b^* are found on oceanic spreading ridges/normal faulting events and lower b^* results for oceanic convergent boundary/thrust mechanisms. Moreover, they evidenced differences in seismic coupling

(fraction of frictional sliding) emerging between continental settings and oceanic settings, while subduction, which have mixed and complex characteristics, appear more similar to the continental settings.

An inner degree of variability of *b*-value, although limited, exists even in *Kagan* [1999] and *Bird and Kagan* [2004]. While *Kagan* [1999] analyses bring the question back to artifacts in magnitude techniques, in *Birds and Kagan* [2004] different behaviors for different tectonic contexts started to emerge. Moreover, both works are performed on a global scale, where from moderate to strong seismicity occurs, while, on local scale, where lower magnitude seismicity can be important, *b*-value variations can be significant.

On the other side, there are several plausible reasons through which the variability of *b*-value can be explained. Currently, the most accepted explanation, supported in this thesis, is that differences in stress levels around the source volume can cause variations of *b*-value, according to *Scholz* [1968] and *Wyss* [1973] (see Paragraphs 4.2 - 4.3). In particular, portions of the highly stressed crust (compressive regimes, subduction zones and deep crust) result in lowering of the *b*-value, while low stress zones (normal regimes, oceanic ridges and shallower crust) result in increasing of *b*-value. The functional form of the relation $b - \sigma$ is analyzed in paragraph 4.1. The reasons of this behavior are consistent with what anticipated by *Anderson* [1905]'s theory: thrust faults are under higher stresses than normal faults (see 2.3).

The *b*-value can be hence considered as a stress-meter for the Earth's crust. Spatial and temporal analyses of *b*-values are widely used for studying the spatial and temporal evolution of the stress field [*Wiemer and Wyss*, 1997; *Wyss et al., 2000; Schorlemmer and Wiemer*, 2005; *Tormann et al.*, 2012, 2013 and others]. Higher stress explains the relatively low *b*-values of foreshocks around the source region (vice versa for aftershocks). Low *b*-values are then used as guides to find earthquakes with unusually stress-drops. The pore-pressure p_w has also important effects on b-value: an increase in p_w decreases the normal stress σ_n on the rock volume, resulting in a lower effective stress. Consequently, decreases in pore pressure might imply induced seismicity events (micro-earthquakes) and increase the seismic hazard [*Bachmann et al.*, 2012]. Dehydration zones along the subducting slab correspond to the location of magma chambers: at this depth, dehydration may increase the pore pressure giving rise to volcanism phenomena. These structures can be localized through the detection of anomalous high *b*-values zones in the crust [*Schorlemmer et al.*, 2003]. Similarly, low *b*-value anomalies along asperity structures correspond to higher stressed portion of the crust, where for example subducting and overriding plates are strongly coupled [*Tormann et al.*, 2015].

On the other side, laboratory experiments confirmed that microfractures frequency-magnitude distributions obey to a power law [*Scholz*, 1968], proving that the FMD exhibits scale invariance. In fact, the GR formulation of the frequency magnitude relation was originally derived from a statistical model of rock and crustal deformation [*Ishimoto and Ida*, 1939]. Acoustic emissions with granite samples results in a decreasing of *b*-values with confining pressure and differential stress [*Amitrano*, 2003] while heterogeneities in material results in increasing *b*-values [*Mogi*, 1962]. Laboratory tests also showed that increases in thermal gradients cause strong increases in *b*-value [*Warren and Latham*, 1970].

3.2 The influence of tectonic styles on frequency-magnitude distribution: updating and rising questions

The general validity of the GR law has been tested by several studies concerning different distance scales and different tectonic situations. *Schorlemmer et al.* (2005) and *Gulia and Wiemer* (2010) showed that the b-value varies as a function of the faulting style and, in particular, that thrust fault events are associated with lower b-values when compared with normal fault events, while strike-slip faults stay about in the middle between them. We have seen that the usage of rake λ is very practical for the representation of the deformation style of an earthquake: $\lambda = -90°$ indicates a pure normal extensional fault, $\lambda = 90°$ a pure reverse thrust fault and $\lambda = 0°$ and $\lambda = \pm 180°$ pure strike-slip faults, left-lateral and right-lateral respectively. Other values indicate mixed mechanisms: trans-tensive or trans-pressive, depending on the sign of λ (negative or positive respectively). *Schorlemmer et al.* [2005] analyzed various focal mechanisms datasets (worldwide, California, Japan) by selecting, for each of the two nodal planes, sub-catalogs of earthquakes with λ within moving windows with width γ ranging from 60° to 120°, depending on the used datasets (Fig. 1.9). Then, they estimated the b-value of each subcatalog using the maximum likelihood estimation MLE approach [*Aki*, 1965] and plotted it versus the central value of rake λ of each moving window. They found, for both nodal planes, smoothed oscillating behaviors with maximum at or close to $\lambda = -90°$ and minimum at or close to $\lambda = 90°$. The b-value can vary systematically for different styles of faulting because of the *Anderson* [1905]'s theory, according to which thrust faulting requires somewhat larger stresses, in absolute magnitude, than normal faulting. Then, b-value is expected to be higher for normal mechanisms and lower for the thrust ones.

The work of *Schorlemmer et al.* [2005] represents the starting point of the analysis of the FMDs for different tectonic styles. An update and an extension of the original work might be reasonable: in fact, the addition of more than 10 years of data would be of great improvement for the strengthening of the previous results. In the original work, a spatial analysis was missing: b-values of focal mechanisms were gathered in similar-style datasets only on the basis of the rake angle λ.

Nevertheless, the selections based on λ do not resolve the ambiguity of the nodal planes, as reported before. If the separation between principal plane and auxiliary plane would be possible, both $b - \lambda$ trend in Fig. 1.9 would look equal. Instead, as clear from Fig. 1.9, some discrepancies (sometimes greater than the errors) exist for some particular λ in b-values relative to different nodal planes. These differences are less evident in Global CMT catalog, they start to be on SCSN, FNET and Kanto-Tokai, and are remarkable for NCSN. Moreover, the chosen width for the γ parameter is determinant in establishing the smoothing of each $b(\lambda)$ trend. In *Schorlemmer et al.* [2005], in fact, it is only showed the γ-smoothing effect (ranging from 0° to 180°) on "pure" tectonic styles, while different $b(\lambda, \gamma)$trends are not reported. Usage of an alternative separation scheme of focal mechanisms on tectonic regimes, like the *Fröhlich* [1992, 2001] triangle diagram, might help. It avoids the nodal plane ambiguity and the γ-selection, since each mechanism is univocally identified by its plunge angles δ_{PTB}.

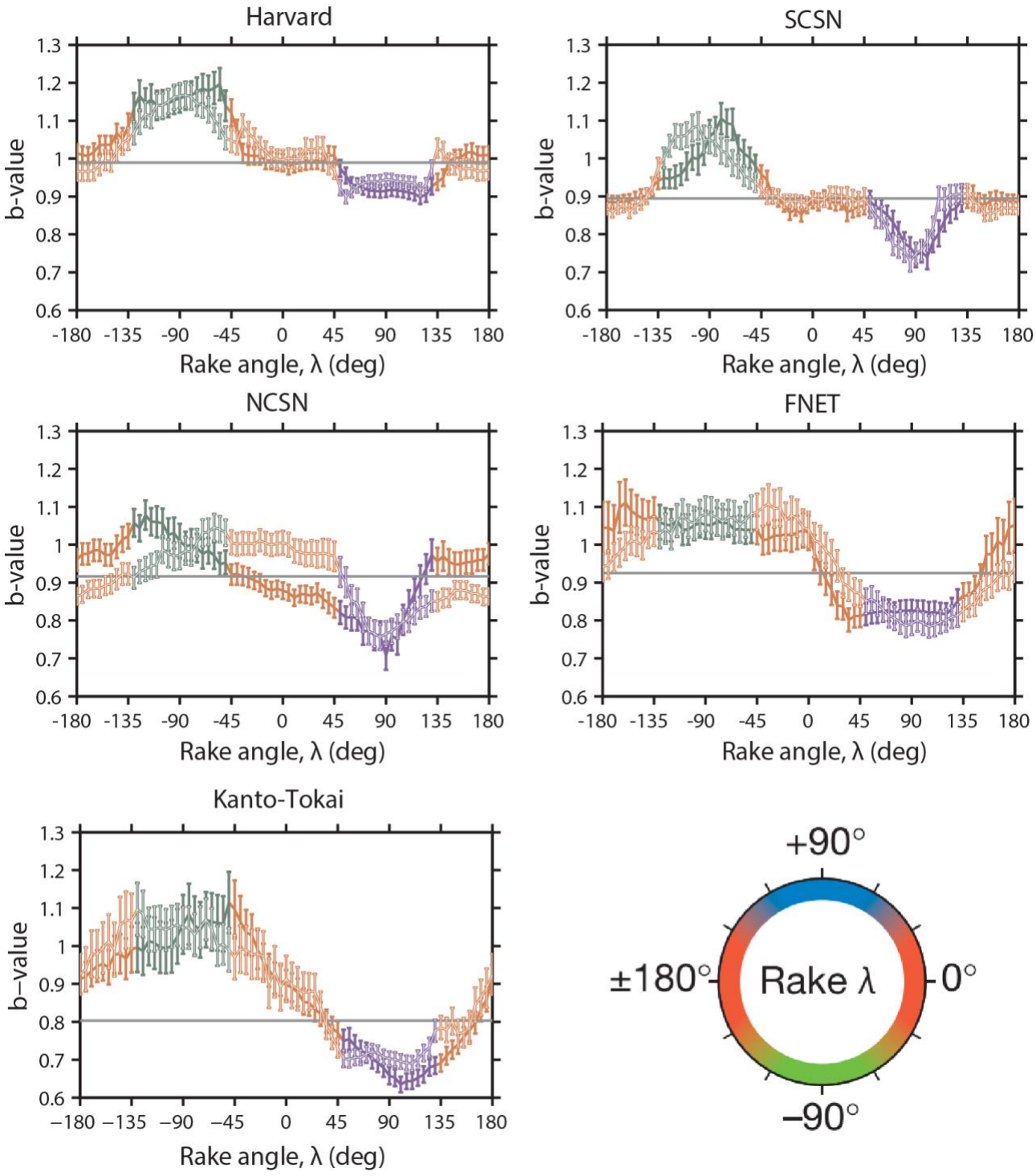

Figure 1.9: Variations of b-value as a function of rake angle λ [Schorlemmer et al., 2005]. Datasets: Harvard Global Centroid Moment Tensor GCMT ($\gamma = 40°$), Southern and Northern California Seismic Network SCSN and NCSN ($\gamma = 20°$ and $\gamma = 40°$ respectively), F-NET and Kanto-Tokai catalogs for Japan ($\gamma = 60°$ and $\gamma = 40°$).

The characteristic oscillating trend of the b-value as a function of rake angle reminds an "harmonic" one. Therefore, another step forward in such analysis could be to try a functional form for data fitting

$$b = F(\lambda) \tag{1.26}$$

A functional relation can be fitted to data only if the b-value estimations come from subsets that are independent each other, i.e. from disjointed selection of the rake angles λ. Furthermore, a functional form of b might provide some insightful understandings on the physics which states beyond the different behaviors of FMD.

4. Linear behaviors of b-value in the Earth's crust

4.1 Strength envelope for the crust: b - depth and b – differential stress

The theory of faulting can be used to obtain a strength envelope for the lithosphere. Equations (1.13) and (1.16) describe also the differential stress trends for the three main tectonic regimes (dip-slip and strike-slip faulting) as a function of depth y, if friction μ is fixed (Fig 1.10). In the upper part of the model the crust behaves like a brittle medium. The rheological behavior of the brittle crust can be modeled through Amonton's law and hydrostatic pore pressure [*Byerlee*, 1978], while the state of stress increases linearly with depth. Stress required for thrust faulting is higher than the one required for normal faulting, so the stress increase with depth is higher for thrust mechanisms with respect to normal ones. The strike-slip state of stress lies somewhere in between.

Although shallow crustal rocks show brittle behavior, greater depths result in higher temperature and pressures: consequently, there are many circumstances under which rocks behave as ductile materials and friction is strongly rock type-temperature-strain rate dependent. The intersection of these two zones determines the *brittle-ductile transition*. To model this behavior of crustal and mantle rocks, plastic rheology can be used. At temperatures that are slightly lower than the solidus temperature T_S, the atoms and dislocations in a crystalline solid become sufficiently mobile to result in creep when the solid is subjected to deviatoric stresses. At lower stresses, the crystalline solid behaves as a Newtonian fluid with a viscosity that depends exponentially on pressure and the absolute temperature (*diffusion creep*). At higher stresses, the motion of dislocations becomes the dominant creep process resulting in a non-Newtonian fluid behavior that also has an exponential pressure and inverse absolute temperature dependence (*dislocation creep*). Experiments and theory indicate that a general form of the relationship between strain-rate $\dot{\epsilon}$ and differential stress is

$$\dot{\epsilon} = C\left(\frac{\sigma_1 - \sigma_3}{G}\right)^n \left(\frac{l}{h}\right)^m \exp\left[-\frac{E_a + pV_a}{RT}\right] \tag{1.27}$$

where C is a pre-exponential factor, G is the shear modulus for the crust, h is the grain size, l is the lattice spacing, E_a is the activation energy, V_a is the activation volume, p is the pressure, R is the gas constant, n is a stress exponent (equal to 2.5), m a grain size exponent (see *Turcotte and Schubert* [2002]). For the temperature T, a gradient of $25\frac{K}{km}$ is assumed. Dislocation creep (black dotted line in Fig. 1.10) is then the applicable deformation mechanism for high stress levels and high temperatures, while diffusion creep (gray dotted line in Fig. 1.10) is dominant for low stress levels.

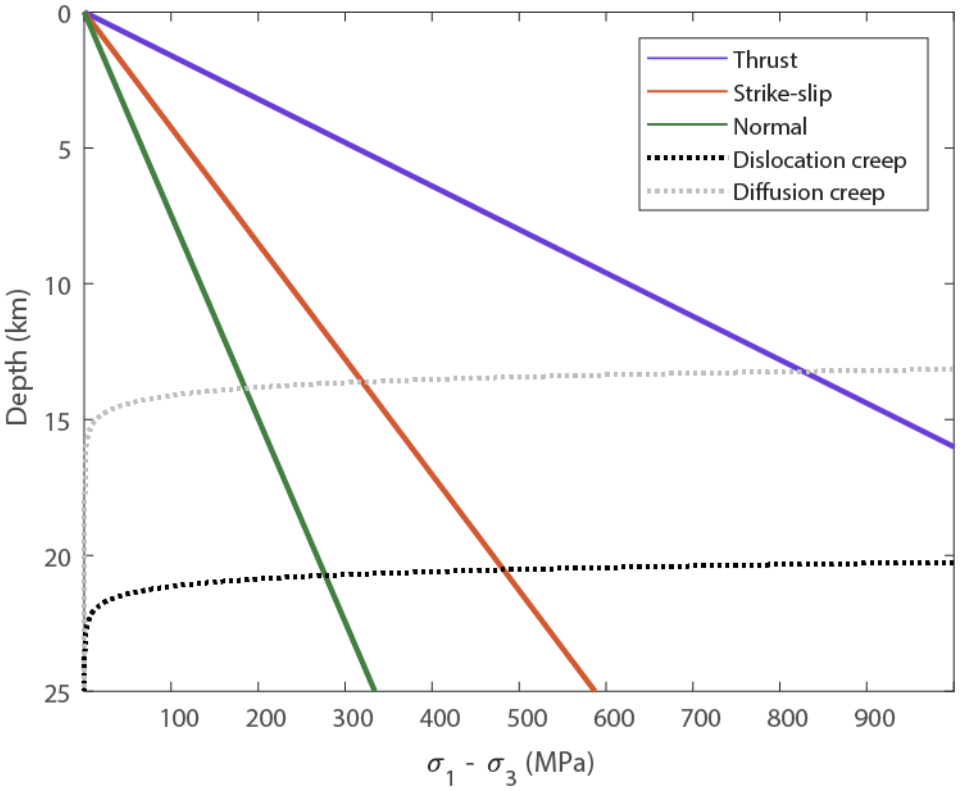

Figure 1.10: Strength profile for the Earth's crust according to Anderson's tectonic styles. Ductile behaviors of rocks result in a drastic decrease of differential stress.

By supposing that the relation between b-value and differential stress is then inversely linear [*Scholz*, 1968] and that the upper crust model described above is valid, b-value must decrease in the brittle upper crust [*Brace and Kohlstedt*, 1980; *Kirby*, 1980] and drastically increase after the brittle-ductile transition. This behavior of b-value as a function of depth has been evidenced by *Spada et al.* [2013] on several local datasets (Fig. 1.11a). Each b-value is estimated by selecting data from moving depth windows, similarly to *Schorlemmer et al.* [2005] for rake angle λ.

On the basis of *Spada et al.* [2013]'s data and results and assuming a frictional behavior for the upper crust ($\mu = 0.75$), *Scholz* [2015] obtained a linear experimental regression law of b-value with differential stress $\sigma_1 - \sigma_3$ (Fig. 1.11b)

$$b(\sigma_1 - \sigma_3) = b_r - k(\sigma_1 - \sigma_3) \tag{1.28}$$

where b_r and k are constants that he empirically estimated as to be $b_r = 1.23 \pm 0.06$ and $k = 0.0012 \pm 0.0003$ (with differential stress expressed in MPa), with a good level of correlation ($R = 0.77$).

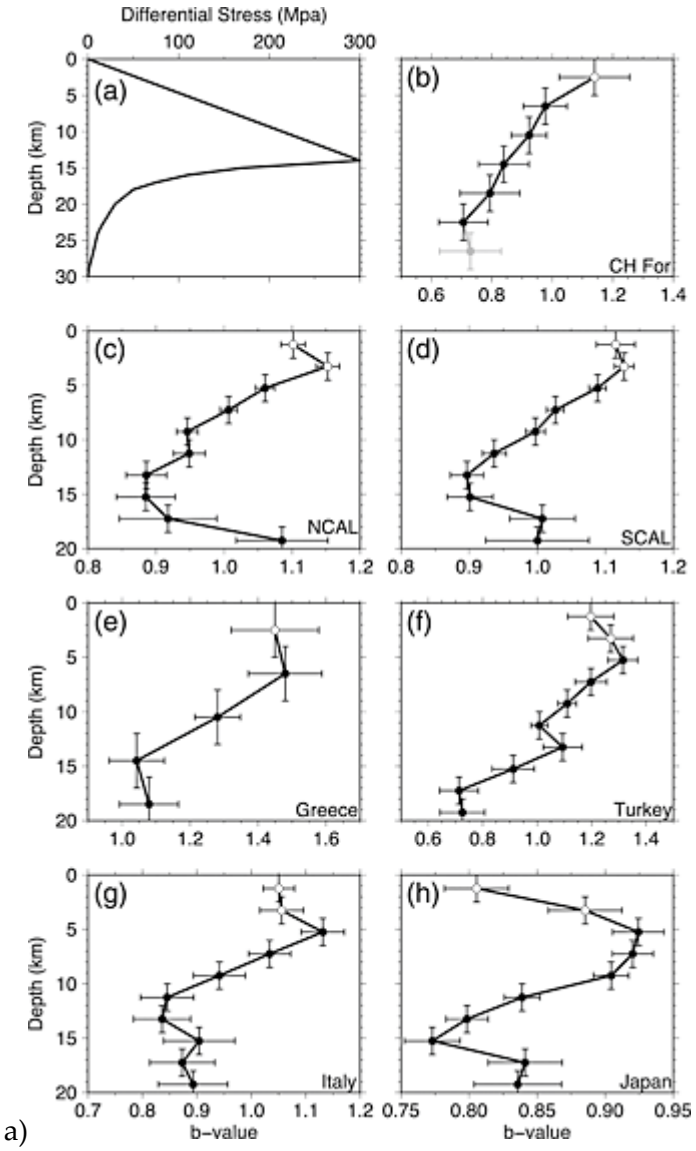

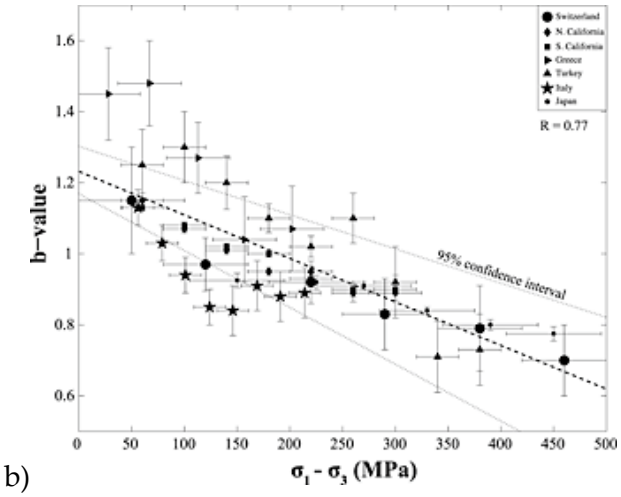

Figure 1.11: b-value as a function of depth [Spada et al., 2013] and differential stress [Scholz, 2015].

4.2 Towards a physical understanding of the earthquake-size distribution

Scholz [1968] analysis explains the basis of the similarity between rock deformation experiments in the laboratory and deformation of the crust: the frequency magnitude relation of micro fracturing events in the laboratory is indeed quite similar to that observed for earthquakes.

If a rock sample is subjected to a uniform applied normal stress $\bar{\sigma}$, the local stress inside the sample σ will vary in some complex way with respect to this mean value. The probability that the local stress is $\sigma(x, y, z)$ within a certain region (small enough such that the stress on it can be considered uniform) is described by $f(\sigma, \bar{\sigma})$ in terms of probability density function. Each region is also characterized by a strength threshold S: fracture will occur within the region if the local stress $\sigma > S$. Variations in S are equivalent to variations in σ within the medium. Fracture will propagate in the region where the local stress exceeds S, weakening the medium, if we assume that these fractures will be arrested if they propagate into adjacent regions of lower stress. The probability that the local stress exceeds the strength is uniform in space and is given by $F(S, \bar{\sigma}) = \int_{-\infty}^{S} f(\sigma, \bar{\sigma})$, so the probability that the fracture will be arrested within a certain area is $\frac{1-F(S,\bar{\sigma})}{A}$. On the other side, the probability that a fracture will stop as it grows from size A to $A + dA$, can be written as

$$g(A)\, dA = \frac{1 - F(S, \bar{\sigma})}{A} dA \tag{1.29}$$

Equations (1.29) states that the probability of incremental fracture varies linearly with the probability that the stress at a certain point is less than S, and inversely to the area swept out by the fracture A. This model takes into account two basic properties of fractures:

1) the definition of $F(S, \bar{\sigma})$ requires the presence of a previous fracture, implying that a fracture weakens the region it penetrates;
2) the probability of growing fracture $g(A)\, dA$ becomes always larger since it is sampling a larger number of regions.

Then,

$$g(A)dA = -\frac{dN(A)}{dA}\,, \qquad N(A) = \int_{A}^{+\infty} n(A)dA \tag{1.30}$$

where $N(A)$ is the cumulative frequency of number of fractures n greater than A. Rearranging of (1.30) provides

$$n(A)dA = [1 - F(S, \bar{\sigma})]A^{-[1-F(S,\bar{\sigma})]-1}dA \tag{1.31}$$

The transition probability of incremental fractures $n(A)dA$ lead to an increased probability of larger fractures with larger stresses. During uniaxial and triaxial compressional tests, *Ishimoto and Iida* [1939] derived a relation for the frequency-magnitude distribution of microfractures experiments

$$n(a)da = ka^{-m}da \tag{1.32}$$

where $n(a)$ is the frequency of amplitudes a and k and m are constant. The most important parameter among the two, m, is simply the slope of the line fitting plot. However, the above relation is equivalent to the GR relation, and *Suzuki* [1959] has shown that the b-value might is related to m as $b = m - 1$. Using the parameters of this model, the expression of coefficient m for *Ishimoto and Iida* [1939] relation is

$$m = \frac{2}{3}\nu[1 - F(S, \bar{\sigma})] + 1 \tag{1.33}$$

where ν is a constant. Consequently, the b-value for microfracture events is

$$b = \frac{2}{3}\nu[1 - F(S, \bar{\sigma})] \tag{1.34}$$

Since $F(S; \bar{\sigma})$ increases with increasing stress, b-value must decrease as stress is increased, in an inverse linear way. It is independent from the area of fracture A, proving that GR model is a scale-invariant process. Moreover, since $F(S; \bar{\sigma})$ is a distribution function, b-value is upper-limited by ν parameter. In fact, according to the general relation of seismology, the energy radiated by an earthquake is $E = \gamma a^{\nu}$, where a is the maximum trace amplitude and γ and ν are experimental constants. Compared to the relation of *Richter* [1958] for energy and magnitude, $\log E = 11 + 1.5\,M$, ν should be equal to 1.5, for a $b_{max} = 1$, corresponding to nihil applied stresses. By admitting higher values of ν, according to the model, higher b-values can be explained. Although b-values greater than 1 are documented both in literature both in this thesis, *Scholz* [1968] explanation well clarifies the role of stress in the frequency magnitude distributions of microfractures and its similarities with crustal earthquakes. However, the above calculations have been made for the special case of a single uniform component of mean stress.

Scholz [1968] showed that the b-value was primarily a function of applied stress σ. He offered a theoretical explanation of his observations, in which the number of fractures was a function of the rupture area distribution $F(S, \bar{\sigma})$, which in turn was governed by the applied stress $\bar{\sigma}$. The replacement of the magnitude by the moment, as a scale for earthquakes, leads to some corollaries which throw light on the physical meaning of the b-value [*Wyss*, 1973]. Seismic moment m and stress-drop $\Delta\sigma$ determinations for complete sets of earthquakes lead to a more complete physical understanding of the frequency-moment distribution of earthquakes. Recalling equations (1.24), and using the definition of the seismic moment, the general frequency relationships as a function of the fault area Σ, of the average displacement D is $N(A, D) \propto (AD)^{-b^*}$ or alternatively, using an expression for the stress drop $\Delta\sigma$ is

$$N(A, \Delta\sigma) \propto (A^{1.5}\Delta\sigma)^{-b*} \tag{1.35}$$

By making the assumption that the stress-drop is a known function of the source dimension r, $\Delta\sigma(r) \sim r^{\gamma}$, one source-parameter equations are obtained

$$N(\Delta\sigma) \propto \Delta\sigma^{-\frac{3+\gamma}{\gamma}b^*} \tag{1.36a}$$

$$\overline{\Delta\sigma} \propto \Delta\sigma_{min}\, exp\left[\frac{\gamma}{b^*(\gamma + 3)}\right] \tag{1.36b}$$

where γ is a constant to determine. Low b-values correlate with high stresses/stress-drops as in the microfracture experiments by *Scholz* [1968]. Earthquake sets with large b-values will have comparatively small stress-drops, also implies relatively small source dimensions.

The usage of the seismic moment m, as a scale for earthquakes, has great advantages and leads to several corollaries which throw light on the physical meaning and possible applications of the b-value. Here we have shown only one of it: it was shown that low b-values indicate high stress in the source region, as predicted by *Scholz* [1968]. Moreover, in *Wyss* [1973] it was also shown that higher stresses could explain the relatively low b-values of foreshocks and the decrease of b-values with focal depth observed for crustal earthquakes, as in *Spada et al.* [2013]. Again, low b-values can be used as a guide to find earthquakes with unusually high stress-drops, as reported in many b-value mapping works, or indicating high local tectonic stresses.

4.3 A first attempt for a unifying model

We have briefly reported *Scholz* [1968] and *Wyss* [1973] theories for different behaviors of FMD as due to stress differences. *Scholz* [1968]'s work explains how the phenomenology is independent from the scale: the linearity of b-value on stress is conserved and universal. *Wyss* [1973] confirmed and extended this concepts through seismic moment and stress drop views, deriving useful corollaries, as for example the variations of b-value with focal depth. The combination of these results with *Anderson* [1905]'s theory of faulting completes the overall picture: thrust faulting mechanisms have lower b-values because of higher differential stress, as compared to normal ones and strike-slip ones. Moreover, the *Anderson* [1905]'s strength solution for the Earth's crust assures linearity of the differential stress with depth, and consequently of the b-value [*Scholz*, 2015]. But, is it possible to combine these three different dependences in a unique one, from a statistical point of view? In part 4, the Maximum Likelihood Estimation method (MLE) is used to derive likelihood models, which consider simultaneous dependences (stress/depth and FM) together, in order to assess which is the "best" one to explain the reality.

5. Structure and targets of the thesis

The main object of this Ph.D. thesis is to validate both theoretically and experimentally the behavior of the GR law as function of tectonic style in terms of fault focal parameters, spatial patterns and hypocentral depth, as a direct consequence of the stress differences in the Earth's crust.

The thesis is structured into three parts, plus a final one resuming all the obtained results.

In part 2 the frequency-magnitude distribution dependence on tectonic styles is recalled, updated and extended using the GCMT dataset. Global maps of M_c and b-value are showed and linked with the main seismotectonic structures: thrust-faulting (subduction zones, continental collisions, deep crust) should correlate with lower b-values, normal-faulting (oceanic trenches, rift zones, shallower crust) should exhibit instead higher b-values. Then, the b-value behavior on rake angle λ should be proved to be time-independent, because more data are available also trying with a stricter selection of mechanisms (lower γ). Moreover, an alternative representation of b-value dependence on tectonic styles (based on plunge angles δ [*Fröhlich* 1992; 2001] is used to show a picture which is consistent with previous results and consequently confirming what expected by *Anderson* [1905]'s theory of faulting.

Part 3 goes much more into the statistical detail of the rake dependence of the b-value: a functional form of b-value as a function of rake with a harmonic function of the type $\Delta b \sim -\sin\lambda$ is fitted to data. The b-value modulation is guaranteed by disjointed subdivisions on rake of the starting datasets, and statistical tests between all possible different rake windows are performed. The existence of a spatial link between variations of the style of faulting and of the b-value is checked here in a different way: a spatial tessellation of the Earth's surface allows to determine the rake and the b-value separately from the GCMT catalog and from the homogenized version of the ISC bulletin respectively. Each seismic cell is characterized through the *Kostrov* [1974] method, and cells with similar deformation regime are gathered together for computing a representative b-value.

In Part 4 a high quality focal mechanisms dataset for Southern California is used to try gathering observations of b-value on focal mechanisms, on depth and on differential stress converging into a unique likelihood model for b-value. This one, despite complexities coming from increase in the number of free parameters, is expected be the "best" model for explaining reality, on the basis of statistical criteria. As a compare, *Scholz* [2015]'s forecast of different gradients of b-value in the crust for different tectonic styles should be considered: lower gradient (11.25 MPa/km) is expected for normal mechanisms, intermediate gradient (22 MPa/km) for strike-slip mechanisms, higher gradient (45 MPa/km) for thrust mechanisms.

6. Datasets

Both global (Global CMT and ISC) and local datasets (Southern California) are used in this thesis. Global datasets are used for the extension of *Schorlemmer et al.* [2005] (see Chapter 2 and 3) while the local dataset for Southern California is used for the implementation of the different *b*-value likelihood models (see Chapter 4).

6.1 Global CMT

The Global Centroid Moment Tensor (acronym GCMT) [*Dziewonski et al.*, 1981; *Ekström et al.*, 2012] is the most authoritative worldwide source for focal mechanisms and it is one of the most used catalog for seismology. The GCMT project involves a systematic determination of moment tensors on global scale with $M_w \gtrsim 5$, also including temporary solutions inside the catalog (so-called "quick solutions"), and continuous development of updated methods for quantifying features of the global seismic sources (Fig. 1.12a).

The Centroid Moment Tensor (CMT) is a method for the computation of the seismic moment tensor developed in the early '80s by the research group of Harvard, now carried on by Columbia University. According to this method, it is possible, under certain conditions, to reconstruct the seismogram recorded by a seismic station, through a relationship that is a linear function of the moment tensor components. The linearity of the relation allows to reverse the calculation to estimate the unknown components of the tensor seismic moment [*Dziewonski et al.*, 1981; *Ekström et al.*, 2012]. Current tensors are calculated according to the CMT method by an inversion process of mantle waves in the 125-350 s band, body waves in the band 40-125 s band and, since 2003, also of surface waves with a period of 50-150 seconds. The usage of long volume waves recorded at teleseismic distances avoids that CMT is generally applicable to moderate earthquakes (smaller than M_w=5), due to the low signal-to-noise ratio [*Pondrelli et al*. 2002].

The catalog ranges from 1976 to present and it is available at http://www.globalcmt.org/CMTfiles.html. The most recent version (September 2016), used for the thesis, contains about 48,000 earthquakes. The moment magnitude M_w reported is computed using the formula of *Kanamori* [1979]

$$M_w = \frac{2}{3}(\log m - 16.1) \tag{1.37}$$

where here the scalar seismic moment m is given in dyne * cm.

Starting from 2004, the usage of intermediate waves resulted in a sudden increase of yearly detected events, because of the ability of analyzing smaller earthquakes (Fig. 1.12b). From 1977 to 2003, a gradual decrease in the median M_w, in part due to improvements in the global network of seismic stations. For the period 2004–2010 the median is approximately 5.2, reflecting the many earthquakes in the range $5.0 \leq M_w \leq 5.5$ that can be analyzed routinely and robustly (Fig. 1.12c). This has, of

course, effects on the catalog completeness. According to *Ekström et al.* [2012], the M_c for the period goes down to 5.0, while older data are more consistent with a value near to 5.3 or 5.4.

Despite for the robustness of CMT M_w, great uncertainties affect the depth information. In fact, according to *Kagan* [1999], there are two reasons because the Global CMT earthquake depths can be biased near the Earth's surface. First, CMT coordinates available in the catalog are for the seismic moment centroid [*Dziewonski et al*., 1998], which should be at least at 15-30 km, especially for great earthquakes, since the largest earthquake fractures involve the entire brittle crust. Second, if the centroid solution does not converge with respect to the depth, the depth is assigned by default, usually at 10 or 33 km, by linking it with external sources (USGS, NEIC, etc).

6.2 ISC Mw

The International Seismological Center (ISC) is an organization involved in collecting, archiving and processing data from more than 130 different data centers, in order to complete the overall picture of global seismicity. The ISC is the catalog at the basis of the Global Earthquake Risk Model (GEM) project, (Http://www.globalquakemodel.org/what/seismic-hazard/instrumental-catalogue) for models of seismic risk [*Storchak et al*, 2013].

The online Bulletin of the ISC (available at http://www.isc.ac.uk/iscbulletin/search/bulletin/ , last accessed February 2016) is the most complete source of earthquake locations and magnitudes at the global scale.

The wide variety of magnitude types coming from different scientific institutions does not still allows to use the entire ISC bulletin to estimate the variations of the *b*-value, since this operation presupposes the availability of a homogeneous magnitude dataset, i.e. calculated according to identical methodologies. For the purposes of this thesis, only part of ISC catalog data was used with homogenous magnitudes re-evaluated according to *Lolli et al.* (2014, 2015). This sub-catalog contains over 400,000 earthquakes with ISC magnitude (originally M_s and m_b), which have been transformed into magnitude M_w through orthogonal regression methods ("Generalized Orthogonal Regression", GOR [*Fuller*, 1987; *Gasperini et al.*, 2013; *Lolli et al.*, 2014]. ISC revised locations are presently available from 1964 to 2013 but for technical reasons only those lying in the time interval from 1990 to 2012 are considered.

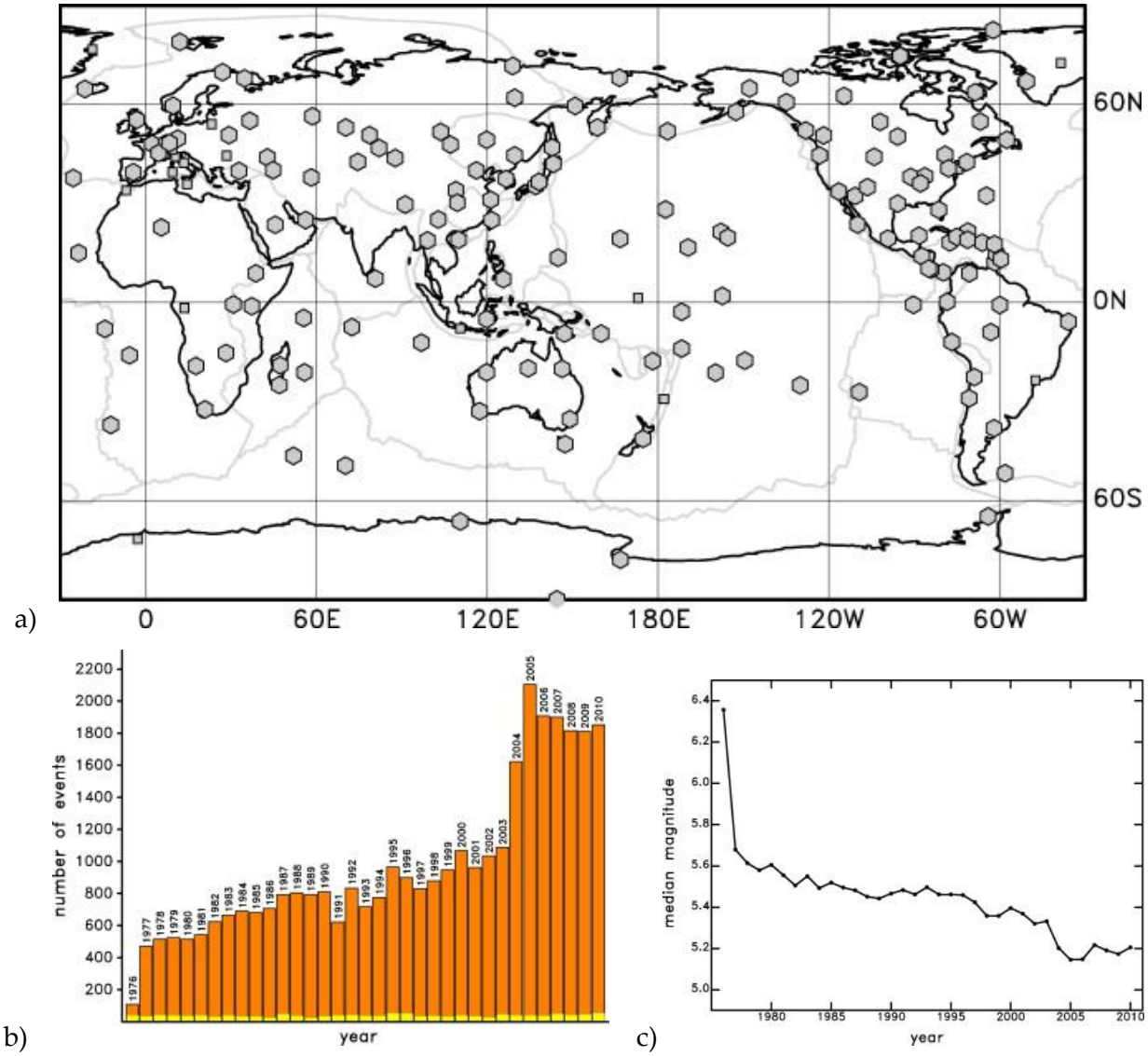

Figure 1.12: Global CMT catalog. a) Locations of the 178 stations of the Global Seismographic Network (GSN) that contributed to GCMT analyses in 2010. **b)** Histogram showing the number of yearly CMT solutions since 1976. The yellow portion of each bar represents the number of earthquakes with $M_W \geq 6.5$. **c) Median** M_W of GCMT earthquakes in each year since 1976. Figures taken from *Ekström et al.* [2012].

6.3 SC catalog

Southern California represents one of the most suitable area for local seismicity analysis, because of the high earthquakes activity and the deep coverage of seismic stations. Recently, the old catalog for focal mechanisms, the Southern California Seismic Network (SCSN), have been updated with a new, more complete version by *Yang et al.* [2012] and *Hauksson et al.* [2012] (http://scedc.caltech.edu/research-tools/alt-2011-yang-hauksson-shearer.html). Using the HASH method developed by *Hardebeck and Shearer* [2002, 2003], focal mechanisms for more than 400000 earthquakes have been determined, ranging a time period from 1981 to 2016 (last update) (Fig. 1.13).

The HASH is a method of determining earthquake focal mechanisms from P-wave first-motion polarities, considering also possible errors in assumed earthquake location and seismic-velocity model. For each event, then, a set of possible focal mechanisms is made up: the average of this set is returned as preferred solution and uncertainty is represented by the distribution of acceptable mechanisms [*Hardebeck and Shearer*, 2002, 2003]. Whenever possible, data have been relocated from the original SCSN catalog by applying waveform cross-correlation techniques.

The result is a refined, high-quality, relocated focal mechanisms catalog for Southern California. A quality flag is assigned to each event (from class A – best – to class – D - worst). Data quality is established according to two parameters: nodal plane uncertainty and azimuthal gap, which both relies on the data coverage on the focal sphere. The mean nodal plane uncertainty (NPU) is the root mean square angular difference of the best nodal planes from the preferred planes on a preliminary catalog [*Hardebeck and Shearer*, 2002]. This parameter results in being inversely related to the number of S/P ratio, i.e. number of polarities. The azimuthal gap (AZG) is the maximum angular difference between two neighboring stations on the focal sphere. Focal mechanisms classes are so indicated: class A (NPU $\leq 25°$, AZG $\leq 90°$), class B (NPU $\leq 25° - 35°$, AZG $\leq 90°$), class C (NPU $\leq 35° - 45°$, AZG $\leq 90°$), class D the others. The dominant pattern of faulting for Southern California is high-angle strike-slip faulting with a small component of normal motion [*Yang et al.*, 2012]. The *b*-value is largest for normal faulting events (about 1.165 ± 0.021) and smallest for reverse faulting events (0.900 ± 0.018) [*Yang et al.*, 2012]. The completeness level is established at 2.5 according to the authors.

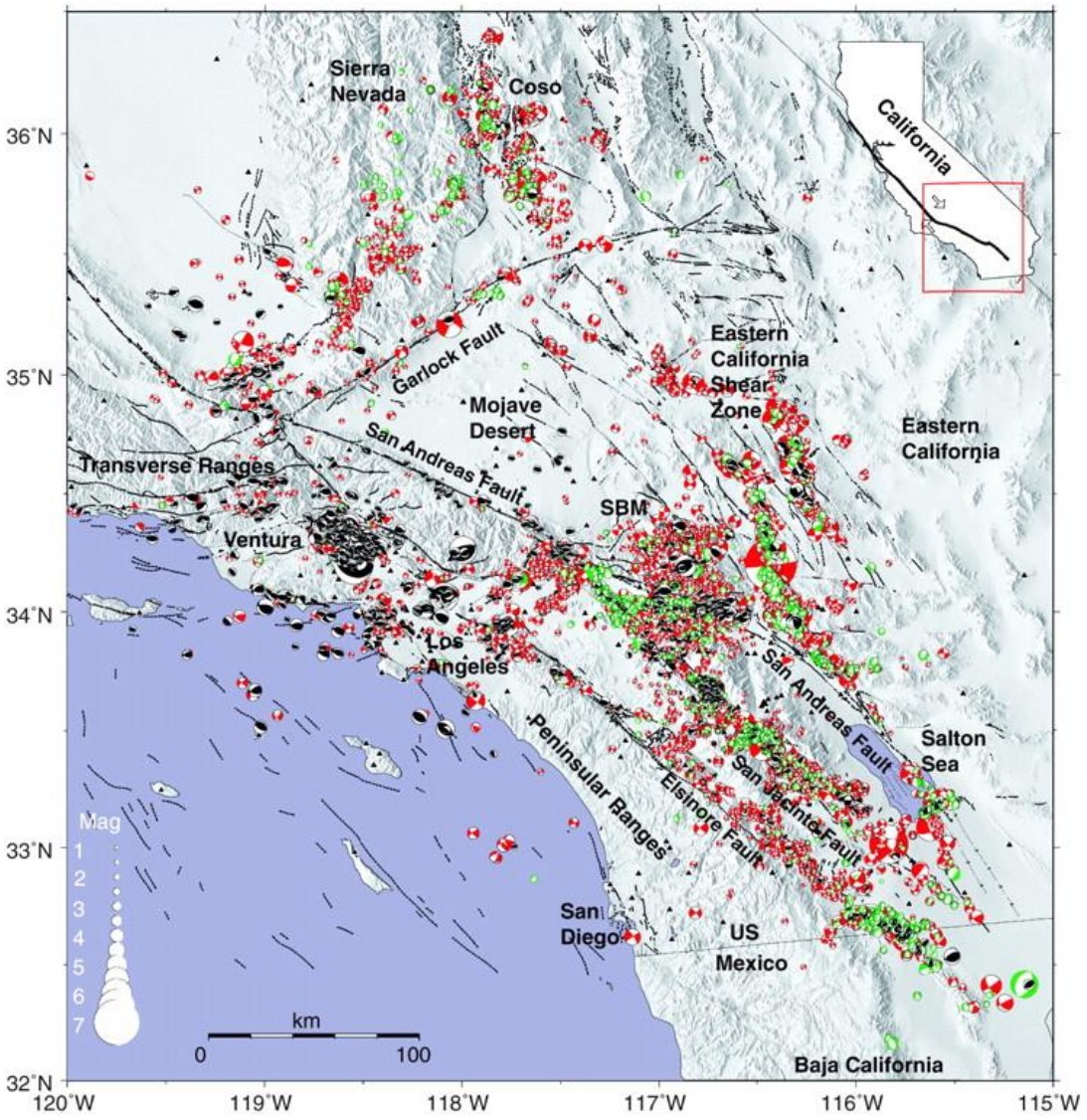

Figure 1.13: Yang et al. [2012] focal mechanisms catalog for Southern California. Original picture from *Yang et al.,* [2012].

Part 2

A UNIFIED THEORY FOR FAULTING STYLE, TECTONIC REGIME AND EARTHQUAKE SIZE-DISTRIBUTION

A. Petruccelli[1]

D. Schorlemmer[2], T. Tormann[3], A. P. Rinaldi[3], S. Wiemer[3], P. Gasperini[1], G. Vannucci[4]

[1] Dipartimento di Fisica e Astronomia, University of Bologna, Italy; [2] Helmholtz Centre Potsdam, GFZ Potsdam, Germany; [3] Swiss Seismological Service, ETH Zurich, Switzerland; [4] Istituto Nazionale di Geofisica e Vulcanologia, Bologna, Italy

Anderson's faulting theory introduced in 1905 describes how fault orientation and differential stress conditions are related. Independently, laboratory measurements on acoustic emissions since the 1960's have established that the differential-stress controls the frequency-size distribution, or b-value, of earthquake populations. In this first part, our global survey of the frequency-size distribution reveals that observed spatial variations are consistent with faulting theory: different tectonic regimes are characterized by distinctly different b-values, generally lower in compressional and higher in extensional regimes, allowing to distinguish 'Chilean type' and 'Mariana type' subduction zones. With a new plunge-based b-value analysis, we additionally resolve a systematic influence of faulting geometry on the frequency size distribution: steep normal faults are found to have highest b-values, while flat thrust faults lowest. Combining such dependencies with a Mohr-Coulomb failure criterion, we present a unified theory linking Anderson faulting and the frequency-size distribution of earthquakes.

1. Introduction

One of the ongoing debates in seismological research concerns the understanding of the frequency-size distribution of earthquakes, its potential variations on different scales, and its significance and interpretation. The empirical behavior in magnitude M of the number of detected earthquakes $N(M)$ is generally well expressed by a negative log-linear trend, commonly known as the Gutenberg-Richter (GR) relation (1.1). In the GR relation, the b-value is the negative slope of the distribution and quantifies the relative proportion of larger to smaller earthquakes: the higher or lower the b-value, the relatively less or more frequent the occurrence of larger magnitude events, respectively.

The large amount of publications on GR b-values reflects the importance of a proper understanding. Firstly, the b-value is a crucial parameter in seismic hazard assessment, used to extrapolate from frequently observed small and moderate seismicity to the rates of rare large and most hazardous events [*Smith*, 1981; *Main*, 1996; *Kagan*, 1999; *Wiemer and Wyss*, 2002 and others]. Secondly, observed spatial and temporal variations in b-values can be interpreted in a seismo-tectonic context and help to unravel a wide range of processes that take place in the Earth's crust, from magma intrusions in volcanic regimes [*Wiemer et al.*, 1998; *Farrell et al., 2009*] to stress redistributions after large earthquakes [*Tormann et al.*, 2015; 2016]. Evidence from natural observations and laboratory measurements suggests for example an inverse relation between b-values and differential stress [*Scholz* 1968; *Amitrano* 2003; *Schorlemmer et al.*, 2005; *Goebel* 2012; 2013; *Tormann et al.*, 2013].

The stress distribution in the crust is a critical parameter for understanding earthquake nucleation, but due to the sparsity of in-situ measurements, stressing condition on faults are probably the key unknown for advancing earthquake forecasting. Differential stress generally increases with increasing depth (see part 1 paragraph 4), a first order gradient in the Earth, and a corresponding decrease of b with depth has been reported in several studies [*Brace and Kohlstedt*, 1980; *Kirby*, 1980]. In particular, it has been shown that b-values increase again when approaching the brittle-ductile transition zone [*Spada et al.*, 2013], consistent with the known strength profile of the Earth crust. High-resolution b-value imaging has been shown to offer important clues on the stressing conditions throughout the seismic cycle [*Cao and Gao,* 2002; *Schorlemmer and Wiemer*, 2005; *Gosh et al*., 2008; *Nanjo et al.*, 2012; *Tormann et al.*, 2012; 2014; 2015; *Schurr et al.*, 2014]. On local to regional scales, lower b-value zones are typical of asperity structures, indicating highly stressed portions of the crust, i.e. potential future rupture patches [*Wiemer and Wyss* 1997, 2002; *Schorlemmer et al.*, 2004; *Schorlemmer and Wiemer*, 2005; *Ghosh et al*., 2008; *Tormann et al.*, 2012, 2014, 2015; *Gulia et al.*, 2016]. On the other hand, higher-b zones match low-stress areas, like volcanic regimes [*Wiemer and Benoit*, 1996; *Wiemer et al.*, 1998; *Wyss* 2001; *Wyss et al.*, 2001; *Schorlemmer et al.*, 2003, *Farrell et al*., 2009; *Tormann et al.*, 2015] and oceanic ridges [*Okal and Romanovics*, 1994; *Kagan*, 1997]. For subduction zones, b-values have been reported to depend on local tectonic properties, such as the age of the subducting plate, the rate of the plate motion and the slab buoyancy [*Molnar and Atwater*, 1978; *Ruff and Kanamori*, 1980, 1983; *Scholz and Campos*, 1995; *Nishikawa and Ide*, 2014].

Anderson's theory defines three possible faulting styles (see Part paragraphs 2.1 and 2.3), according to the orientation of the three principal stresses $\sigma_1, \sigma_2, \sigma_3$. Given a faulting style, the differential stress (i.e. the difference between maximum and minimum principal stresses) required for reactivation is

strictly linked to frictional properties and to the orientation of a fault. Indeed, a systematic dependence of the *b*-value on faulting style for global and regional datasets has been documented [*Schorlemmer et al*., 2005; *Gulia and Wiemer*, 2010; *Yang et al*., 2012]. Especially for large datasets, the *b*-value is often observed to be close to unity and some authors argue about its constancy [*Kagan*, 1999, 2002a, 2002b, 2003, 2010; *Bird and Kagan*, 2004]. *Schorlemmer et al.* [2005] and *Gulia and Wiemer* [2010] showed, on FM datasets from different areas (world-wide, California, Japan and Italy), a systematic dependence of the *b*–value on the rake angle λ of the focal mechanisms, i.e. a dependence on different tectonic regimes: normal faulting events λ = -90° have highest *b*-values (~1.1–1.2), thrust events λ = 90° the lowest (~0.7–0.8), and strike-slip events λ = 0, ±180° intermediate values (~1). Because thrust faults (compressive regime) tend to be under higher stress than normal faults (extensive regime) [*Anderson*, 1905], these observations are consistent with the results of laboratory measurements according to which *b*-values depend inversely on differential stress [*Scholz* 1968; *Amitrano* 2003; *Goebel* 2012, 2013].

Missing until today, however, is a quantitative comparison and theory, which unifies Anderson's faulting theory, differential stress dependency and the size distribution of earthquakes. To develop such a theory, we perform a global survey of the earthquake size distribution and find that spatial patterns of *b* reflect the main global seismotectonic structures, and the generic dependence of *b*-values on rake angles λ of the FM is confirmed in the most recent global data. We test and confirm that the observed spatial variations and the variation with rake angle are consistent with the ones predicted by Andersons faulting theory, if assuming an inverse relationship between *b*-value and differential stress. We then develop a new analysis approach linking *b*-values and faulting geometry, which uses the plunge-based ternary diagram (see part 1 paragraph 2.4). Finally, we combine those ternary analyses of *b* with fault modeling and derive a relation linking *b*-value with differential stress to be applied for dip-slip fault modeling.

2. Global M_c and *b*-value mapping

2.1 Data and methods

Data

We use FM data from the Global CMT catalog [*Dziewonski et al.*, 1981; *Ekstrom et al*., 2012] (see Part 1 paragraph 6.1), starting from January 1980 to the end of September 2016. Following *Schorlemmer et al.* [2005], we limited to earthquakes with hypocentral depth of 0–50 km. Moreover, moment magnitudes M_W binned to $\Delta M = 0.1$ are used. The GCMT catalog provides strike, dip, and rake values for both nodal planes [*Ekström et al.*, 2012]; we refer to the first plane as plane 1 and to the second one as plane 2.

Methods: Mc - *b* mapping

Spatial *b* and M_c distributions are often computed by selecting events within sampling volumes on regular grids [*Wiemer and Wyss*, 2000]. However, considering the non-uniformity of the global earthquake density, we adopt a slightly different approach. We use the epicenters of all earthquakes in the top 50km as nodes (Fig. 2.1). Around each of these nodes, we select all earthquakes within cylinders of different radii (from 200 km to 1400 km, see A, B, C, D points in Fig. 2.1) down to a depth of 50 km. For reliable parameter estimates, we consider only those cylinders containing a minimum number of 200 events for M_c estimations and more than 100 events above the completeness magnitude for the subsequent *b*-value estimation. To reach the best possible spatial resolution, we use the smallest of the above cylinders that surpasses the required event numbers.

We decide to automatically select different classes of cylindrical radii for the selection of GCMT earthquakes into the *b*-M_c maps. The selected radii (Fig 2.1) depend on the local data density, and are the basis for the calculation of the M_c and *b*-values. According to the stability criteria for M_c and *b* described above, the more the area surrounding each center/node is crowded of events the less the radius selected for that node will be lower. For GCMT, the smallest radii are assigned at locations with high density of events (red dots), i.e. subduction zones [*Hayes et al.*, 2012]. For continental and especially ridges areas, higher radii are necessary to sample the minimum number of events due to lower event density.

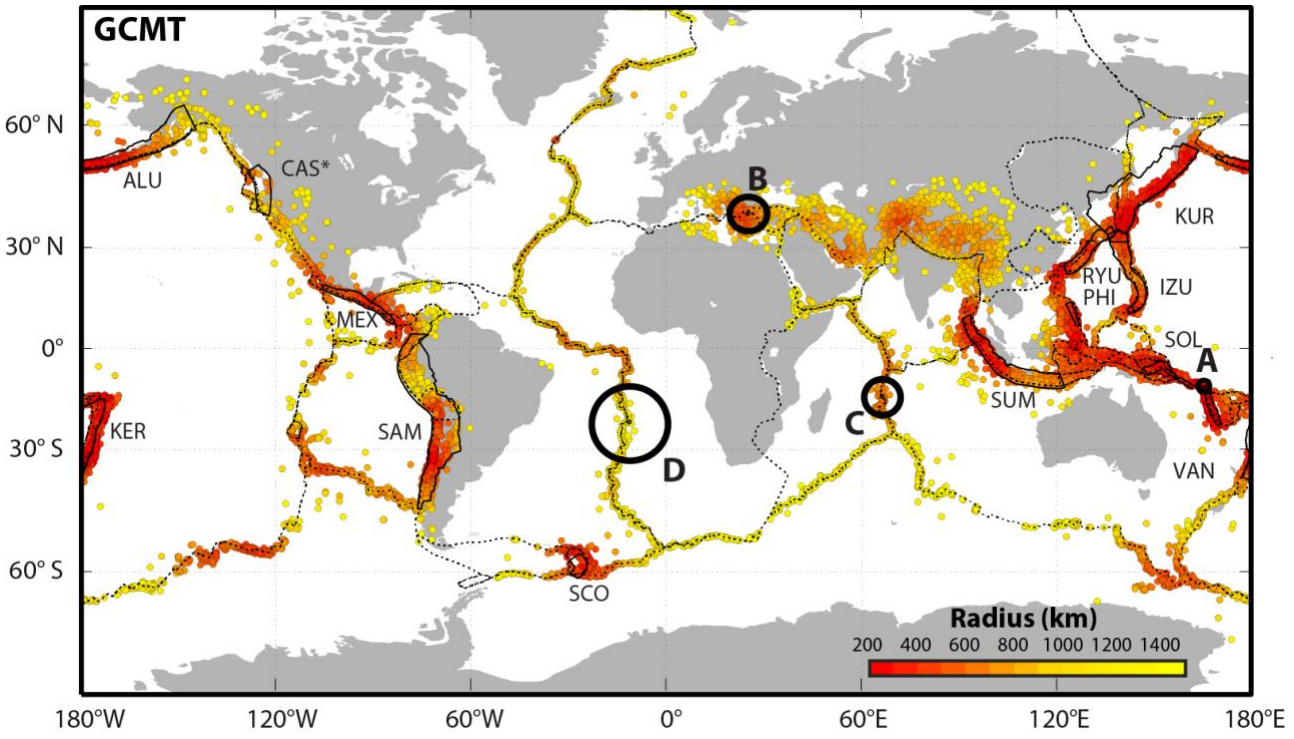

Figure. 2.1. Global map of selection radius *R* for the GCMT catalog (1980–2016, depth = 0–50 km). Dotted black line: global plate-boundary model by *Bird* [2003]. Subduction zones (black solid lines) according to the SLAB 1.0 model [*Hayes et al.*, 2012] (for the zone acronyms see List of symbols and acronyms).

We estimate M_c using the Maximum-Curvature method (adding 0.2 magnitude units to be conservative, see part 1 paragraph 1.2) [*Wiemer and Wyss*, 2002; *Woessner and Wiemer*, 2005] and we compute *b*-values using the standard maximum-likelihood method (equation 1.8 of *Aki*, 1965). For the standard deviation assessments, the computations are bootstrapped [*Efron*, 1987; *Efron and Tibshirani*, 1993] hundred times.

M_c is a critical parameter in *b*-value determination, as an underestimate in M_c leads to a systematic underestimate in *b*-value [*Woessner and Wiemer*, 2005]. Because catalog completeness depends on station distribution, which changes over time, spatial and temporal completeness variations are expected in every catalog. In general, completeness is expected to improve with time as the network density increases. Local assessments of M_c are thus required for different periods separately. Due to the continuous improvement of the global seismographic network, the completeness level of the GCMT catalog has improved from 5.4 – 5.5 for older data down to 5.0 after 2010 [*Ekström et al.*, 2012]. However, the M_c-map (Fig. 2.2) of the GCMT catalog for the full period since 1980 shows that most M_c-values are in the range 5.4–5.5, with only little deviations in some particular zones: along most oceanic ridges and in the Himalayan area the M_c-values are slightly lower with 5.1–5.3.

In order to test the influence of tectonic regimes on the estimated *b*-values, two statistical tests are performed: the *Utsu* [1966] test (see Part 3 paragraph 2.3) and the *Wilcoxon* [1945] ranked sum test. While Utsu's test is done to check whether two estimations of *b*-value are significantly different, the Wilcoxon ranked sum test, instead, is performed to decide if the populations are sampled from continuous distributions with equal medians (5% significance level). Moreover, we also test the gaussianity of those distributions, using a Kolmogorov-Smirnov.

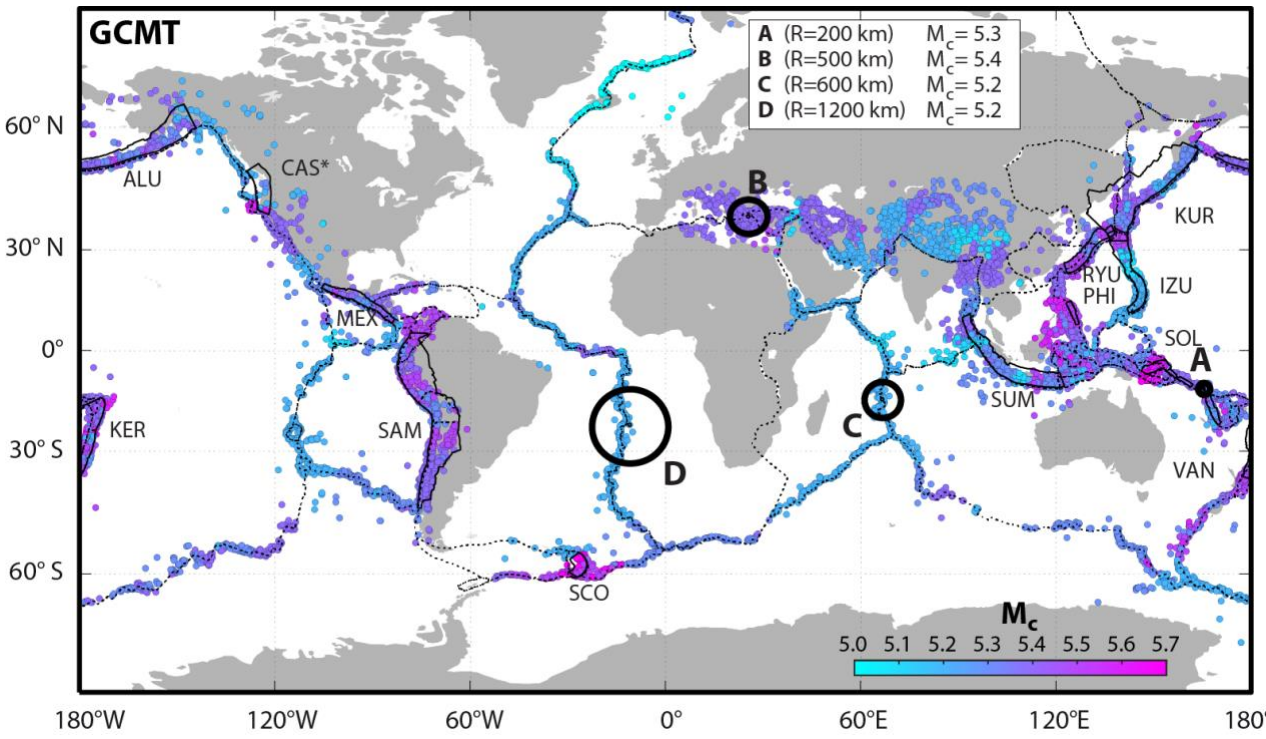

Figure 2.2. Global map of M_c for the GCMT catalog (1980–2016, depth = 0–50 km). Points A, B, C, D, plate boundaries and faults classification are the same of Fig. 2.1.

Methods: *b* – rake angle

The now available longer period is used to reassess the systematic dependency of *b*-values on the earthquake rake angle. The same processing of *Schorlemmer et al.* [2005] is followed with only one modification: instead of using a sampling window of $\gamma = 40°$, the increased number of events (12448 compared to the original 7636) allows us to reduce this value to 20°. For this analysis, the whole catalog is cutted at the overall completeness magnitude of Mw = 5.5. The analysis for plane 1 and the full study period (1980 - 2016) is firstly shown. Then, the more detailed analysis using both nodal planes, different periods, and different γ is provided. For the sake of completeness, we will also compare the residual distributions (summed on all λ_i) of γ=40° data with respect to *Schorlemmer et al.* [2005] and "constant-b" models.

Methods: *b* – plunge angles

In addition to the rake angle, a triplet of plunge angles can also be used to infer the tectonic style of a FM (see part 1 paragraph 2.4). Ranging from 0° to 90°, such angles correspond to the dip (with respect to the horizontal direction) of the P, B, and T axes (corresponding to moment tensor eigenvectors), with sizes (eigenvalues) from lowest to highest respectively. Each earthquake above the completeness level is reported into the diagram, and a corresponding *b*-value is estimated by sampling its 500 nearest neighbor events within the diagram. Because events in a ternary diagram tend to cluster, this procedure is preferred to an equal tessellation, which may result in great differences in number of selected events, in order to preserve the *b*-value pattern continuity.

2.2 Testing the effect of tectonic regime on global *b*-value

1st order tectonic imprint

If differential stress impacts *b*-values, then we must expect systematic variations of *b*-values for different tectonic provinces. To test this hypothesis, we perform the first comprehensive global survey of *b*-values to date, based on the CMT global earthquake catalog since 1980 (Fig. 2.3). To classify the tectonic zones, we use independently defined references [*Bird*, 2003; *Hayes et al*., 2012], while for the spatial mapping we assess local completeness magnitudes (see Fig. 2.2).

We find statistically significant and highly systematic variations that are in agreement with the hypothesis. The *b*-value overall are found to vary spatially (Fig, 2.3 a, b), but with a highly systematic pattern that rather well reflect three main tectonic categories: we resolve high *b*-values along the mid-ocean ridges, low *b*-values in the subduction zones, and intermediate *b*-values in the continental zones, where mixtures of different FMs coexist. However, we noted that in some sparse cases, like for some heterogeneous tectonic areas (e.g. Europe or the Himalaya), our selected volumes contained a mixture of different FM styles, and consequently our *b*-values did not fully resolve the

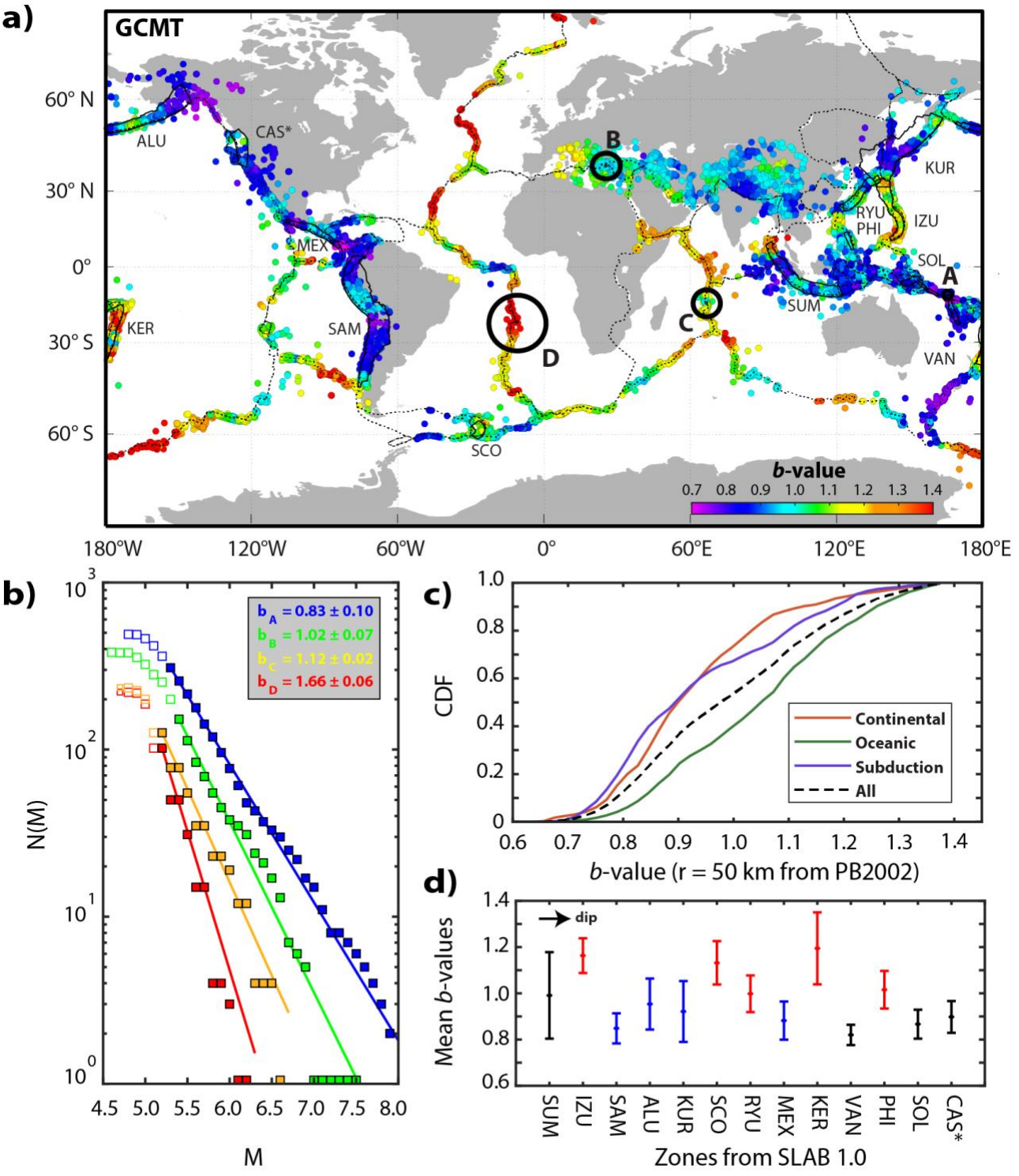

Figure 2.3. *b*-value distributions for the Global CMT catalog: a) Global map of *b*-values for the GCMT catalog. Dotted black line: global plate-boundary model PB2002, solid black line: subduction zones according to the SLAB 1.0 model (for underlying M_c and R maps see Figs 2.1, 2.2). **b) Frequency-magnitude distributions** corresponding to points A (R = 200 km, M_c = 5.3), B (R = 500 km, M_c = 5.4), C (R = 600 km, M_c = 5.2), and D (R = 1200km, M_c = 5.2) of a). **c) Cumulative density functions** of *b*-values of a) sampled within a radius of 50 km from PB2002. **d) Average *b*-values for SLAB 1.0 subduction zones**, error bars: standard deviation, red: Mariana type zones (high *b*), blue: Chilean type zones (low *b*) [*Uyeda and Kanamori*, 1982], black: undefined types. Zones are ordered according to increasing slab dip (for Cascadia CAS, unknown).

mixture of local tectonic regimes (Fig. 2.3, black outlined dots). Then, we apply the moment tensor summation by *Kostrov* (1974) (see paragraph 2.6) to establish a dominant deformation regime for the selected area: we determine the largest double couple by decomposition of the cumulative moment tensor according to the Harvard CMT standard procedure (see for details *Gasperini and Vannucci* [2003]). If the Compensated Linear Vector Dipole (CLVD) component of the cumulative moment tensor is lower than 15% the center-node indicates a prevalent tectonic regime, while a larger CLVD component indicates tectonic heterogeneities of the focal mechanisms population.

However, the *b*-populations are distinctly different at significance levels exceeding 0.01 when using for example *Utsu* [1966]'s test (Table 2.1) on 4 selected locations (Fig. 2.3b). To test if tectonic regime is a statistically significant predictor of *b*-value, we derive first of all the distribution of *b*-values separately for each of the tectonic regimes, following the previous classification schema of *Bird* [2003]. The resulting distributions (Fig. 2.3 c), including the global one, are not normally distributed, which we confirm using a Kolmogorov–Smirnov test (see Table 2.2). We then apply the non-parametric Wilcoxon signed-rank test to decide if the populations are sampled from continuous distributions with equal medians (5% significance level): we find that the subduction distribution is significantly different from the oceanic one, which in turn differs from the continental one (Table 2.2).

N	*b*-value	Points	A	B	C	D
350	0.83 ± 0.10	**A (subduction)**	1	0.186	**0**	**0**
148	1.02 ± 0.07	**B (continent)**	0.186	1	0.446	**0.002**
329	1.12 ± 0.02	**C (ocean)**	**0**	0.446	1	***0.014***
75	1.66 ± 0.06	**D (ocean)**	**0**	**0.002**	***0.014***	1

Table 2.1: Utsu test P_b, where P_b is the probability of the A, B, C, D *b*-values of Fig. 2.3 a, b (second column) of being equal. Bold italic (5% significance) and bold (1% significance) P_b indicate significantly and high significantly different *b*-values. Number of complete events for *b*-value estimation in the first column.

Wilcoxon test				Kolmogorov-Smirnov test
PDF	**Continents**	**Oceanic**	**Subduction**	
Continents	1	**0**	0,06	**0**
Oceanic	**0**	1	**0**	**0**
Subduction	0,06	**0**	1	**0**

Table 2.2: Wilcoxon and Kolmogorov-Smirnov tests (last column) for the PDFs of Fig. 2.3 c (5% significance level). Wilcoxon test computes the probability of being wrong in rejecting the null hypotheses that two distributions come from continuous distributions with same medians, while Kolmogorov-Smirnov assumes as null hypotheses that data are normally distributes.

2nd order differentiation of subduction types

On a global scale, the bulk of total moment release occurs in subduction zones [*Pacheco and Sykes*, 1992], where the worldwide largest observed earthquakes break the contact area between the overriding and under-thrusting plates. These compressive regimes feature the highest, strong magnitudes earthquake activity, and the lowest *b*-values on our map. On the contrary, oceanic spreading ridges feature lower seismicity compared to subduction zones, of lower magnitudes, resulting in high *b*-values. Our global results are fully consistent with local studies that resolve low and very low *b*-values along the thrust interface [*Tormann et al.*, 2015]. Besides the abundant plate-interface thrust seismicity, minor shallow normal-faulting activity occurs off-trench due to bending as the lithosphere begins to descent [*Chen et al.*, 1982; *Fröhlich et al.*, 1982]. While a *b*-value differentiation of these off-trench normal-faulting events from the ones of thrust regime is beyond the resolution capability of this global analysis, *Tormann et al.* [2015] have shown that they scale with higher *b*-values.

In fact, subduction zones show a great degree of variability in structure and characteristics. A first order classification according to *Uyeda* [1982] distinguishes between *Chilean-type* subduction (young, hot, and slow-moving subducting lithosphere at low dipping angle with strong compression along strongly-coupled interfaces) and *Mariana-type* subduction (old, cold, and fast-moving subducting lithosphere at steep dipping angle, accompanied by extensional roll-back mechanisms and back-arc spreading, while lacking great earthquakes due to low coupling). We find that the global *b*-values distinguish these types clearly (Fig. 2.3d): Chilean-type subduction zones (Fig 2.3 d, blue) – are mostly characterized by low *b*-values. The much steeper dipping Mariana-type subduction zones (Fig 2.3 d, right) feature instead higher *b*-values.

We now zoom into more detail in four regions (Figure 2.4).

The Mariana subduction zone (Fig. 2.4 a) is part of convergent oceanic margin of about 2800 km [*Stern*, 2002]. Here, the old seafloor subducts deep in the crust, giving rise to widespread volcanic activity and hydrothermal emissions [*Baker et al.*, 2008], and lack of very deep earthquakes compared to other subduction zones [*Katsumata and Sykes*, 1969]. FM diagram (Fig. 2.4 a) indicates that both compression and extension can coexist in such zones: downdip tension in the lower zone and downdip compression in the upper zones [*Samowitz and Forsyth*, 1981]. This double seismic zone locates at depths where the slab curvature is maximum, and where it straights into a planar configuration [*Stern et al.*, 2003]. Here, both thermal stresses and anelastic unbending of the upper part slab cause low-magnitude shallow seismicity patterns [*Samowitz and Forsyth*, 1981], consistent with general high *b*-values. These results also agree with the suggested dependency of *b*-values on the age and the slab buoyancy of the subducting lithosphere [*Nishikawa and Ide*, 2014], which likely govern the state of stress on the interface between the subducting and the overriding plate. Young and more buoyant slabs (Chilean-type) exhibit high normal and shear stress on the interface (i.e. low *b*-values), while old and heavy ones (Mariana-type) produce lower stresses (higher *b*-values).

The Chilean subduction zone (Fig. 2.4 b), which originates from the subduction of the Nazca Plate beneath the South America Plate, is instead associated with widespread and relatively high magnitude seismicity [*Stern*, 2002], mostly characterized by thrust fault mechanisms, and hence by lower *b*-values. There, the strong coupling between overriding plates determine high applied shear stress. Moving towards the southwest oceanic ridges, where faulting is normal and strike-slip, *b*-values gradually increase.

Seismicity along the spreading rifts and transform faults of mid-oceanic ridges (Figs. 2.4 c) has previously been reported to have higher *b*-values compared to the global average [*Kagan*, 1997]. With their low coupling coefficient, the bulk of deformation along these systems occurs aseismically. While the spreading ridges are characterized by volcanic activity and associated normal-faulting seismicity, the transform faults generate many slow earthquakes and, given their length and linearity, produce rather small strike-slip earthquakes (*Boettcher and Jordan* [2004] and references therein). High pore pressures and the extensional regime suggest low differential stresses in these regions, which is consistently reflected by the measured high *b*-values.

Continental collision zones show typically strong tectonic heterogeneity on spatial scales that are beyond the resolution capability of this global study. Thus, we here cannot distinguish the individual local regimes and their imprints on local *b*-values. Rather, we observe overall intermediate *b*-values for continental collision boundaries, partially with a tendency towards lower *b*-values e.g. in the Himalayan region (e.g., Fig. 2.4 d) but also a tendency towards higher *b*-values in the European area. Continental rift systems, e.g. the East African Rift are characterized by high *b*-values as expected in an extensional regime.

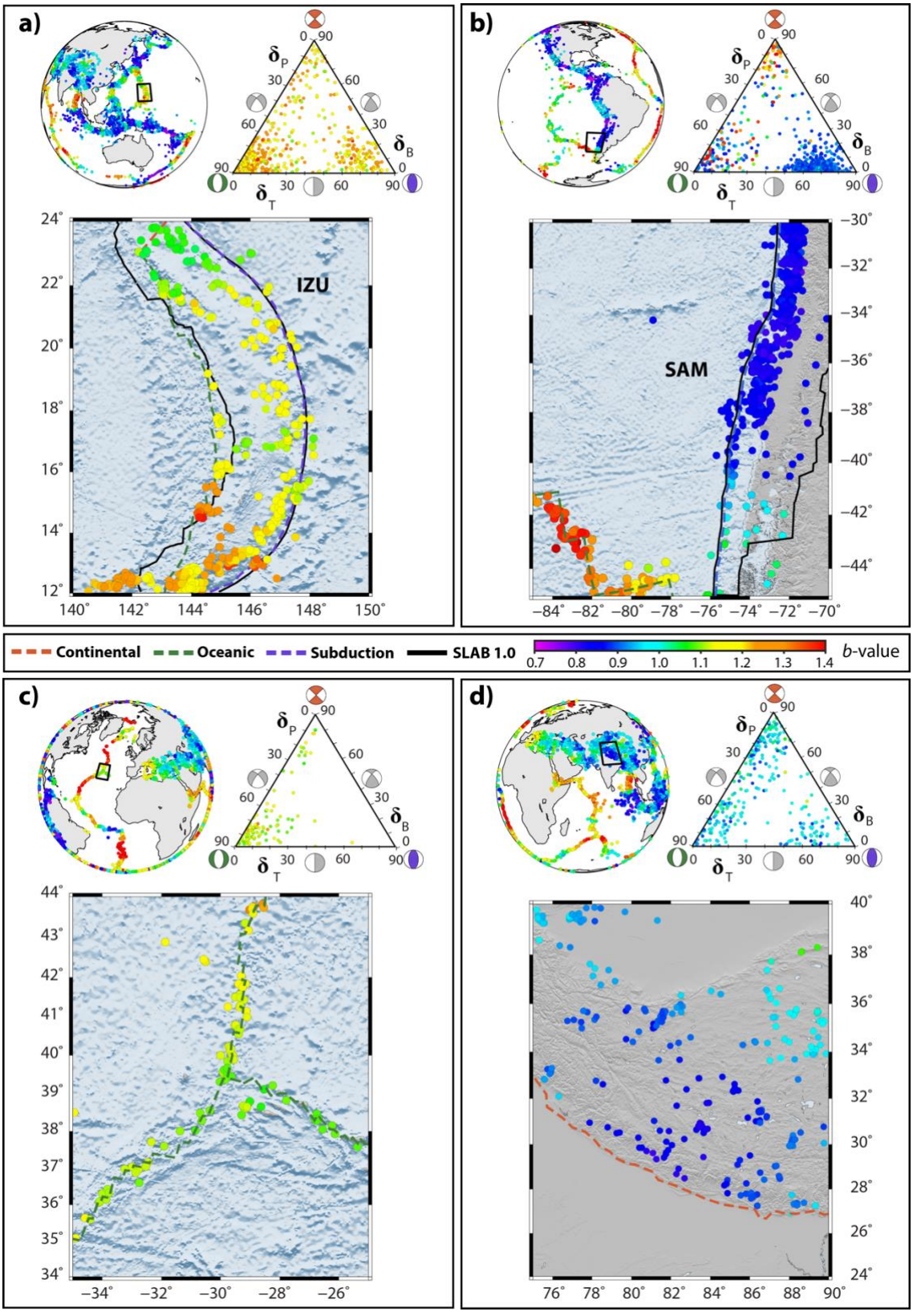

Figure 2.4. Different seismotectonic structures and relative ternary diagrams: a) Mariana type subduction zone: mostly normal and thrust events and only high *b*-values. b) Chilean type subduction zone: majority of thrust events with low *b*-values (high *b*-value strike-slip and normal-faulting events along the oceanic ridge faults in the southwest). c) Oceanic ridge: mostly normal, some strike-slip events with high and very high *b*-values. d) Continental collision zone (NPL): mixture of event types with intermediate *b*-values.

3. Reassessing the effect of rake angle on global *b*-values

A map of the global FMs based on rake angle λ well matches the seismotectonic description so far explained (Fig. 2.5 a). The reassessment of the *b*-value rake angle dependence based on more than 10 years of additional seismicity data fully confirms the results documented by *Schorlemmer et al.* [2005].

With the additional data, we can reduce the selection width γ to 20° (Fig. 2.5 b, right) reaching a higher resolution than that used by *Schorlemmer et al.* [2005] (γ=40° Fig. 2.5 b, left) and being always consistent with it (gray trend on the background). In addition, we find that the maxima in *b* are offset from the pure normal faulting mechanism (λ=-90°) by approximately ±45°. We follow up on this finding in the subsequent section: what we can highlight is that the analysis at $\gamma = 40^{\circ}$ (Fig. 2.5 b, left panel) shows the first order pattern of faulting style vs *b*-value, while the γ=20° (Fig. 2.5 b, right panel) reveals that within a given style there is a dependency on the differential-stress.

We formally test the null hypothesis (no rake dependence of *b*) against the alternative hypothesis given by the *Schorlemmer et al.* [2005] model (1980-2004, z=0 - 50 km, $\gamma = 40°$) using the Wilcoxon test and find that the null hypothesis can be rejected at significance levels < 0.01 (Fig 2.6).

We verify the same *b*-λ dependence for both nodal planes and different periods individually (Fig. 2.7). We keep fixed the depth layer 0-50 km while we vary the time period (1980-2004, 1980-2016, 2005-2016) and the parameter $\gamma = \pm 20°, \pm 30°, \pm 40°$. Bigger panels refer to nodal plane 1 while upper panels insets refer to nodal plane 2, as indicated by the authors of the catalog. The chosen periods refer to the original one of *Schorlemmer et al.* [2005] (1980-2004, where we set $M_c = 5.5$, also indicated with a gray frame), to the updated one (1980-2016, where we set $M_c = 5.5$ again) and the independent a brand new one (2005-2016, where we set a $M_c = 5.2$).

The peculiar trend is always conserved with all the time-γ combinations. The different choices for the γ-parameter enhance different smoothing effects of the b-λ trends: a lower γ allows the detection of the different peaks relatives to vertical thrust and normal mechanisms.

Thus, the spatial mapping and *b*-λ assessment are completely consistent each other.

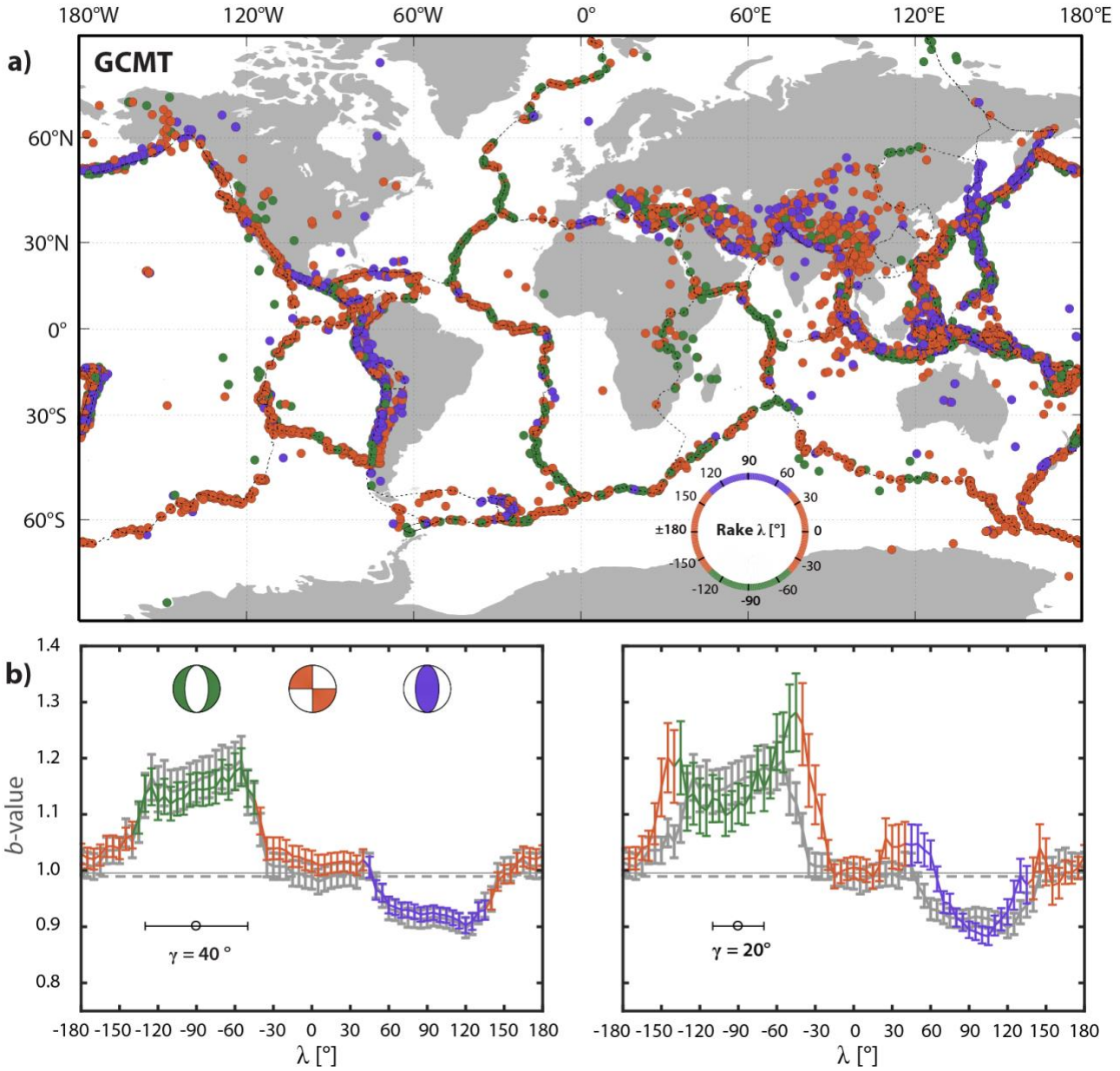

Figure 2.5. GCMT FM analyses based on the rake angle λ of the first nodal plane (1980–2016, z = 0–50 km, M_c = 5.5). a) FM characterization according to λ. Rake angles with $-135° \leq \lambda \leq -45°$ are defined as normal mechanisms (green dots), rake angles with $45° \leq \lambda \leq 135°$ are defined as thrust mechanisms (blue dots), while the others are defined as strike-slip mechanisms (red dots) (see *Schorlemmer et al.*, 2005). **b) Variations of *b*-values on rake angle λ.** The left and right frames compare the *b*-value (colored lines) as a function of λ with range γ of 20° and 40° (indicated with a horizontal black width bar), respectively, with the computations using only a width γ of 40° by *Schorlemmer et al.* [2005] (gray background lines, 1980–2004, z = 0–50 km, M_c = 5.5). Error bars on *b*-values are the uncertainties by *Shi and Bolt* [1982]. Horizontal gray dashed and solid lines are the *b*-value computed with the entire datasets of *Schorlemmer et al.* [2005] and of this work respectively (M_c = 5.5).

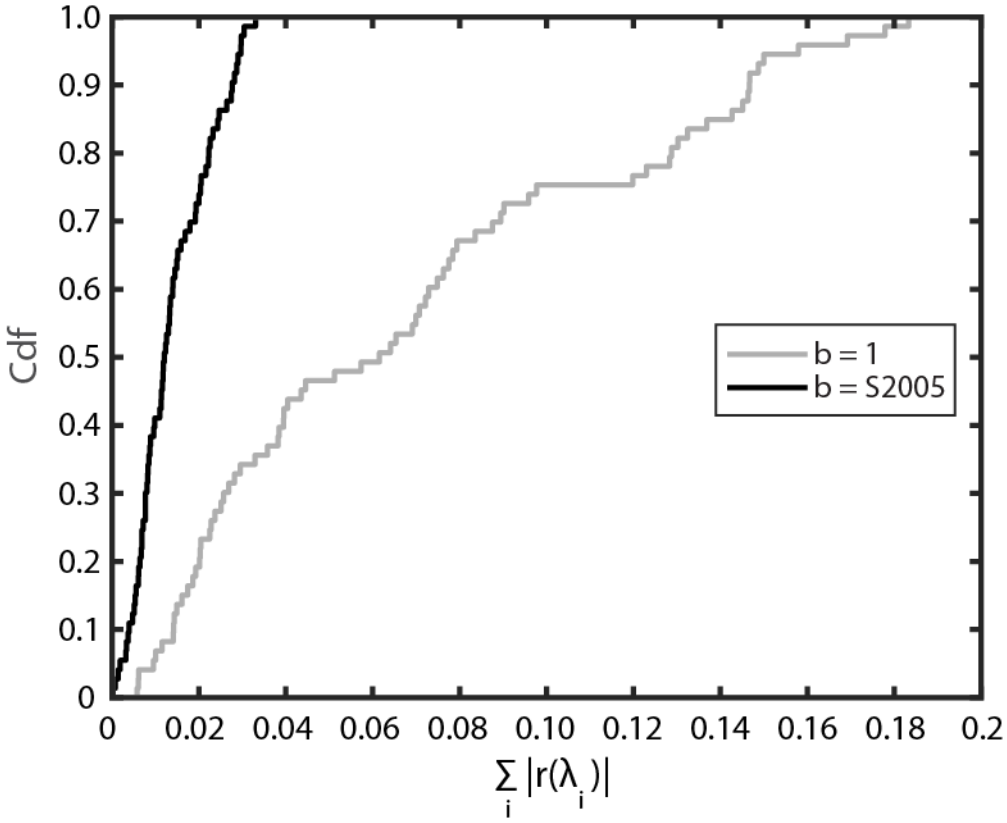

Figure 2.6. Cumulative density functions for the sum residuals (on all λ_i) of the Fig 2.5 b (γ=40°) data with respect to a constant b=1 model (gray) and to S2005 (black) data. The two histograms are significantly different at 0.01.

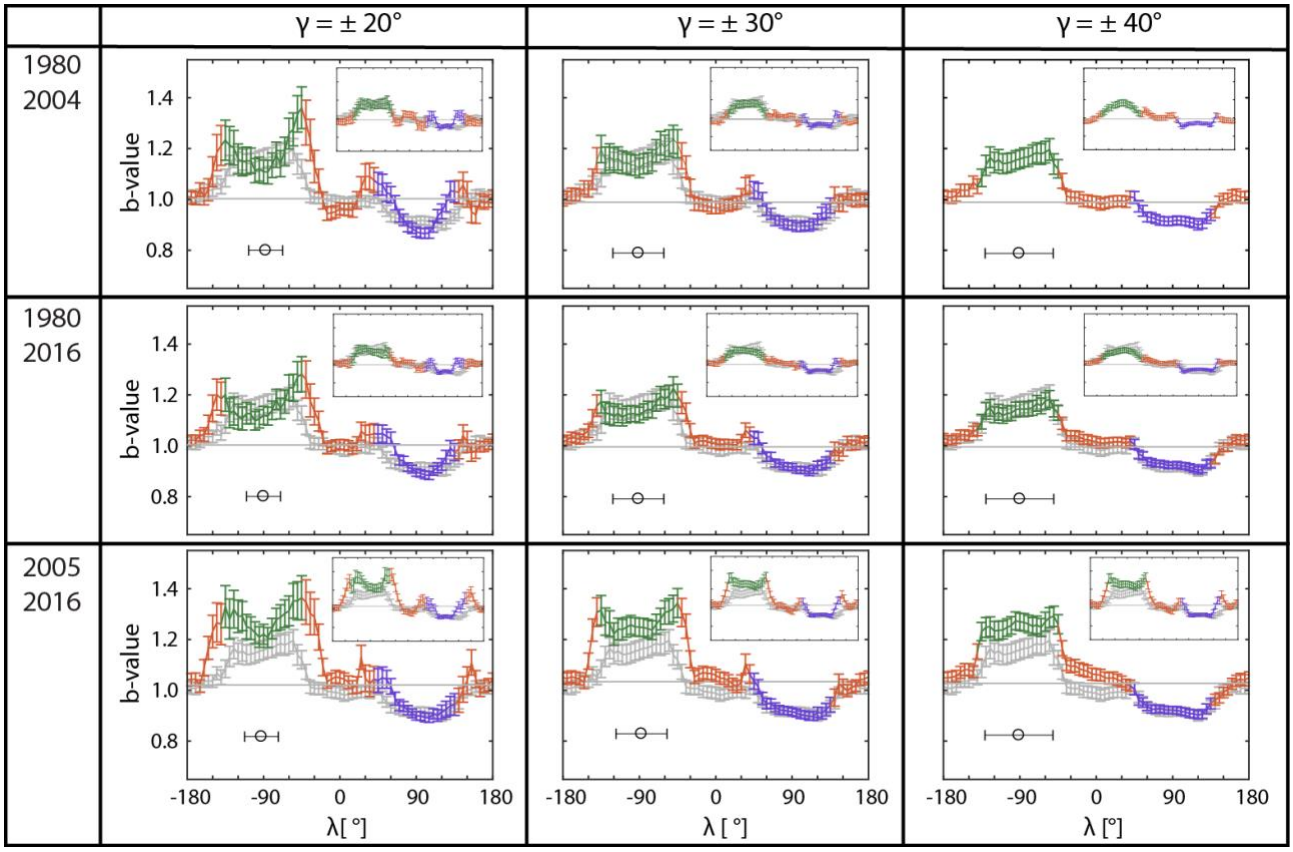

Figure 2.7. *b*-value dependence on rake angle λ for different time-γ selections (1980–2016, depth = 0–50 km). Rows show different time periods while columns refer to different γ value. Horizontal gray line refers to mean b-value for the specific time-γ subset.

4. Novel *b*-FM representation in ternary diagram: evidences of *b* differences for dip-slip faulting regimes

In order to investigate further parameters that might systematically imprint on the *b*-value, we extend the established analysis of the *b*-value dependence on faulting style by introducing a new analysis approach by using the ternary diagram of *Fröhlich* [1992, 2001]. Assigning *b*-values to each earthquake in the ternary diagram confirms at first order the typical pattern (Fig. 2.8 a): higher, intermediate, and low *b*-values for normal (left corner), strike-slip (top corner), and thrust (right corner) events, respectively. More importantly, this representation newly reveals further *b*-value variations within the mechanism types: along the bottom edge of the diagram, the populations of normal and thrust earthquakes (dip-slip faults) *b*-values suffer significant variations, starting from the pure mechanism vertexes (for normal $\delta_T = 0°$ and thrust $\delta_T = 90°$) towards vertical/horizontal orientations ($\delta_T \sim 45°$). To our knowledge, it is the first time that this effect is resolved in *b*-value data within thrust-normal faulting regimes: we observe lowest *b*-values towards vertical/horizontal orientations from the thrust corner of the triangle ($50° \lesssim \delta_T \lesssim 60°$) and highest *b*-values towards vertical/horizontal orientations from the normal corner ($30° \lesssim \delta_T \lesssim 40°$).

Figures 2.8 b and 2.8 d show how the new plunge-based (Fig 2.8 a) and the previously introduced rake-based (Figs. 2.8b and 2.5b right) representations of FM are related: the sampled rake windows of the FMs roughly span triangular δ selections inside the ternary diagram, thus equally reflecting the differences in *b*-values for normal and thrust families (Fig. 2.8c). We note that "pure" dip-slip faults ($\lambda = \pm 90°$) lie on the bottom of the triangle, while the "pure" strike-slips ($\lambda = 0, \pm 180°$) align along the vertical axis of the diagram.

5. Dip-slip faulting re-activation process

It is known from faulting theory of *Anderson* [1905] for dip-slip faults that differences in faults orientations cause differences in stress conditions: thrust faults dip less with respect to normal faults, with an angle β (fault dip) which depends on the frictional properties of the rock. Furthermore, an increase in friction enhances the difference in required shear stress for faulting.

Using the Mohr-Coulomb criterion, the differential stress $\Delta\sigma = \sigma_1 - \sigma_3$ required for reactivating a dip-slip fault, given a friction coefficient μ, on the bottom edge of the ternary diagram as a function of δ_T (see Appendix B for analytical details) is

$$\Delta\sigma(\delta_T|\mu) = \frac{C + 2\mu(\rho g z - p)}{\pm \sin 2\beta(\delta_T) - \mu[1 - \cos 2\beta(\delta_T)]} \qquad (2.1)$$

Equation (2.1) well show that thrust faulting regime (positive stresses) is under higher stress conditions with respect to normal faulting regime (negative stresses). Moreover, it can be applied to four different cases: high dip (gray curves in Figs. 2.9 a with $\beta > 45°$) and low dip (black curves in Figs. 2.9 a with $\beta < 45°$) planes for the two tectonic styles (normal, with $\delta_T < 45°$ and thrust, with $\delta_T > 45°$).

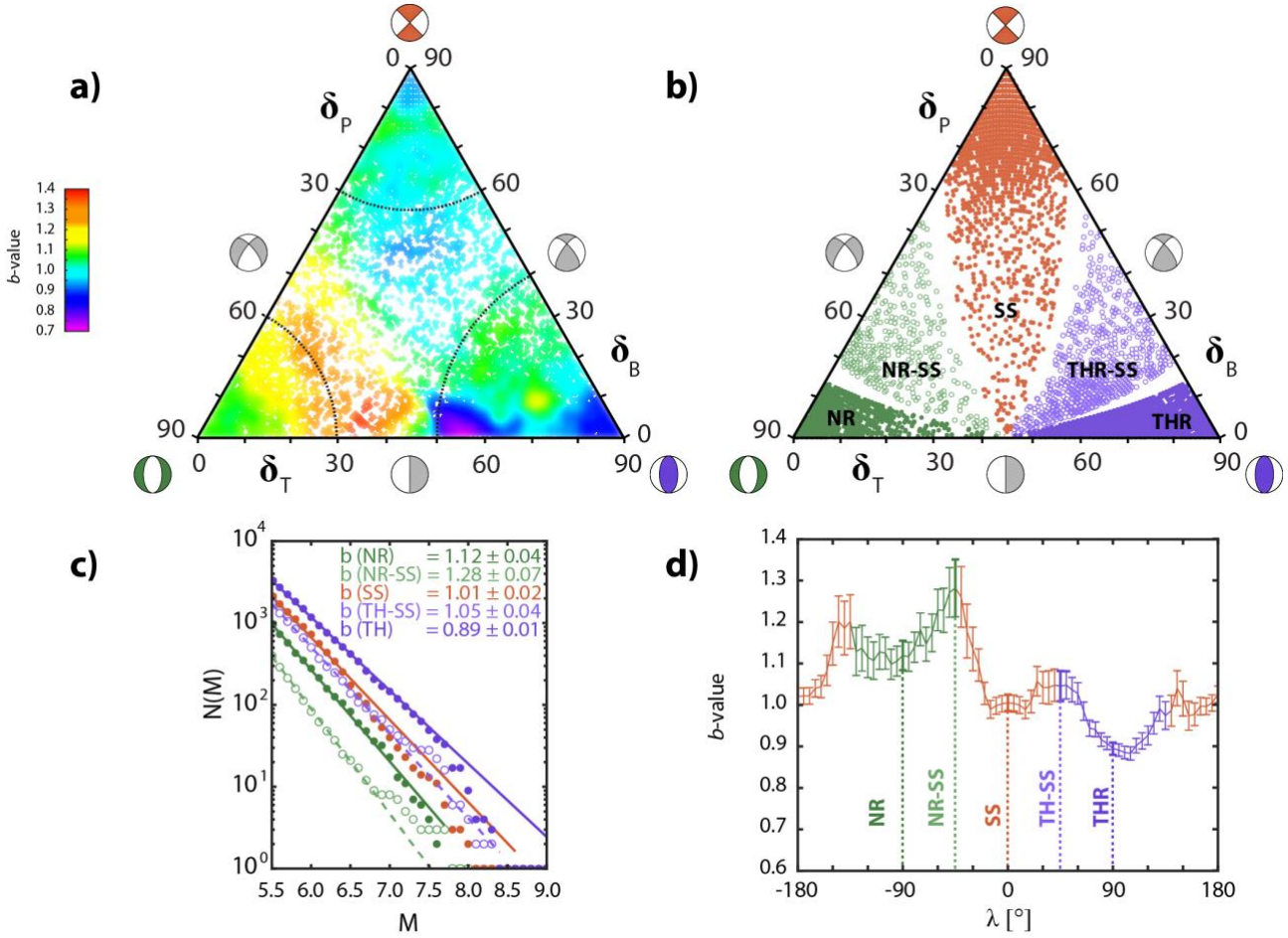

Figure 2.8. Ternary FM and b-value analyses. a) b-value mapping inside the FM triangle using nearest (500) neighbors approach: black dotted lines delineate areas of the almost "pure" NR, SS, and TH styles**. b) + d) Association between rake sampling width γ = 20° (same of Fig. 2.5b) and representation in the ternary plot for selected rake bins. c) FMDs for subsets of b):** a-value for TH-SS is doubled for plotting purposes.

Relations of dip angles $\beta_{1,2}$ as function of δ_T angle for the four cases are derived in the Appendix B and showed in Fig. 2.9 b: optimal planes (normal and thrust corners) would dip at β=45° while, as going towards the center of the diagram, one orientation (assume β_2) rotates toward the vertical (β=90°) and the other one (β_1) toward the horizontal (β=0°). In Fig. 2.8 b, a good comparison of the analytical solutions (2.1) with observed dip-slip ternary data ($\delta_B \leq 5°$ data of Fig. 2.8 a, displayed in the upper left corner) can be achieved with a double normalized plot of b' (ranging from 0 to 1) and differential stress $\Delta\sigma'$ (ranging from -1 for normal mechanisms to 1 for thrust mechanisms) with δ_T or $\beta_{1,2}$.

The inverse linearity between the (normalized) dip-slip *b*-values and the differential stress is expressed through

$$b'(\delta_T|\mu) = \frac{1}{2}[1 - \Delta\sigma'(\delta_T|\mu)] \quad (2.2)$$

The higher μ, the higher required stress (in absolute value) for fracturing: since thrust faulting differential stress ($\sigma_1 > \sigma_3$) is higher than the normal one ($\sigma_3 > \sigma_1$) fracturing, the curves would tend to slip up and down respectively. In other terms, if the friction coefficient μ is fixed, the more vertical a thrust fault, the more energy required for fracturing, and vice versa for normal faults. These differences are well described through μ-level curves of equations 2.1 and 2.2 in which most of the *b*-values fit (Fig. 2.8 c). Normal mechanisms ($\delta_T < 40°$) fit with high dip curves (gray curves on the left side), and thrust mechanisms ($\delta_T > 55°$) fit with low dip curves (black curves on the right side), as expected by theory of faulting. Data from $\delta_T = 40°$ to $\delta_T = 55°$ (gray circles) are removed since they come from smoothing effect due to the adopted technique for mapping.

Starting from the center ($\delta_T \sim 40°$ for NR and $\delta_T \sim 55°$ for TH) and following the arrows, the four curves also describe the activation cycle of dip-slip faults with the dip angles $\beta_{1,2}$ (Fig. 2.9 d).

For NR (Fig. 2.9c, curves on the left, and Fig. 2.9d, left faulting schemes), the dip angle increases along the black line (low-dip β_1) towards low δ_T where both β tend to 45°. This is associated with a progressive decrease (in absolute value) in differential stress starting from the maximum physical value (depending on the tensile strength, see caption). The trend then continues along the grey line (high-dip β_2), where the differential stress reaches its minimum (absolute) at around 60° dipping, and it keeps increasing for steeper faults (grey scheme, Fig. 2.9 d). Since there are no data to fit on, the shallowly-dipping NR solution is unlikely to happen.

For TH faulting (Fig. 2.9 c, curves on the right, and Fig. 2.9 d, right faulting schemes) the path is similar: from the center following the low-dip β_1 curve towards high δ_T (where again both β tend to 45°) with decreasing differential stress (Fig. 2.9 d, blue curves), and then from high δ_T to the center on the grey line (high-dip β_2) with higher differential-stress. In this case, the steeply dipping TH solution is improbable for mechanical reasons.

However, the *b*-values of the "pure" corners could potentially deviate from the analytical solutions, containing some events that are not TH or NR with β=45°. Purely horizontal/vertical motion cases (central vertical line, δ_T =45°, i.e. β_1=0°, β_2=90°) represent a singularity of the problem (see Appendix B), since here the differential stresses required for fracture would provide some unphysical solutions (Fig 2.10). In fact, for normal faulting the $\Delta\sigma$ cannot be larger (in absolute value) than the lithostatic stress (Fig. 2.9 a, left side), otherwise a tensile fracture would take place. On the other side, for thrust faulting regime Δσ is limited to an upper boundary (i.e. 400 MPa, Fig. 2.9a, right side).

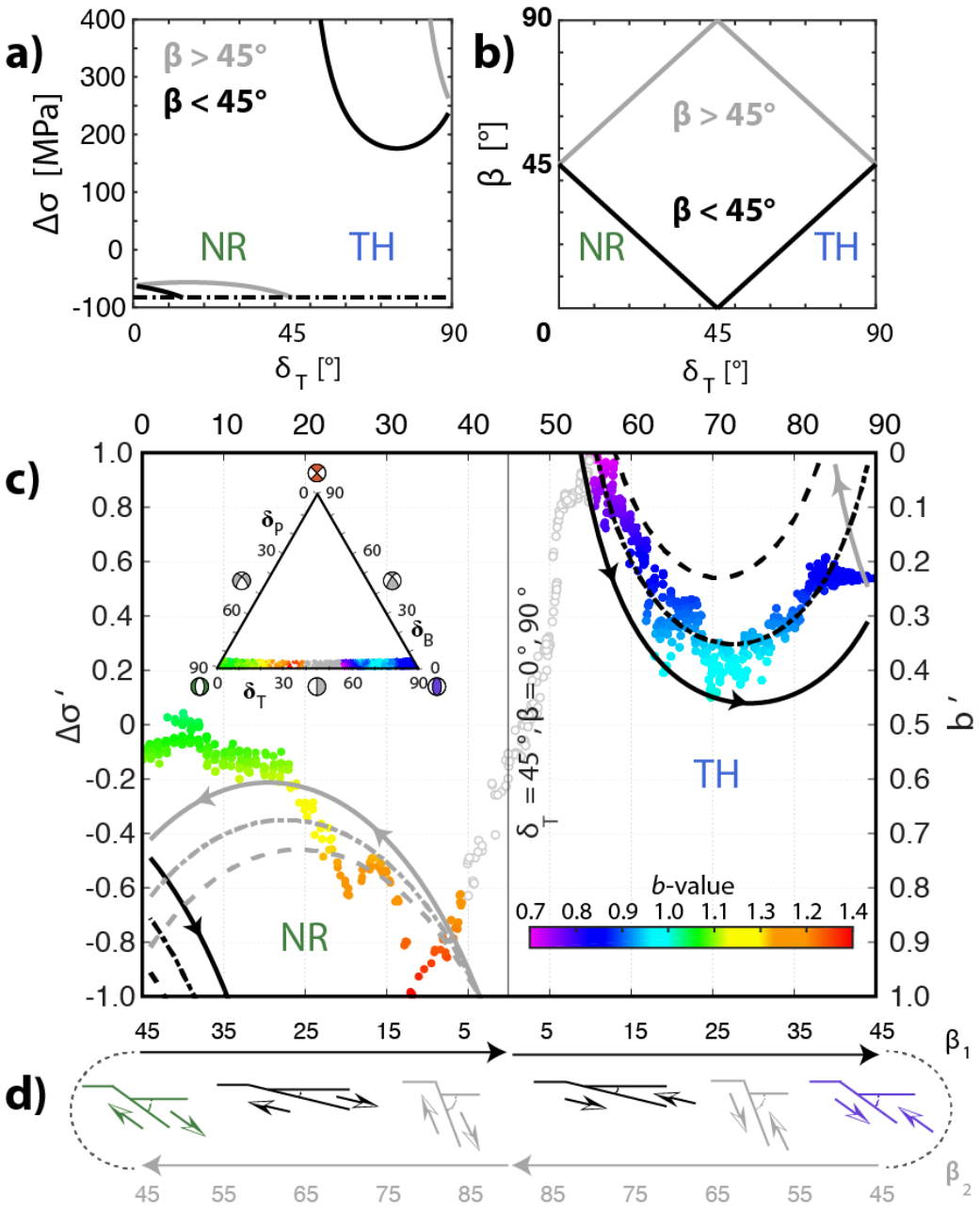

Figure 2.9. GCMT dip-slip (λ=±90°) b-values combined with faulting theory and Mohr-Coulomb criterion. a) Dip-slip differential-stress curves (1): cohesion C=0 MPa, friction μ=0.6, maximum compressive stress Δσ = 400 MPa. Horizontal dash-dotted line indicates a lithostatic stress of 83 MPa (ϱ=2700 kg/m3, z=5000 m)**. b) β(δT) relations:** optimal planes (NR and TH corners) are expected to dip at β=45° while, as going towards the center of the diagram, one orientation rotates toward the vertical (β=90°) and the other one toward the horizontal (β=0°) (see Appendix B)**. c) Normalized GCMT dip-slip b-values b' and differential stress Δσ' of (2) with different μ on plunge angles δT (top) or dip angles β1,2 (bottom, see d)).** *b′* are normalized with respect to minimum/maximum *b*-values while *Δσ′* with respect to minimum (negative) / maximum (positive) stresses (see Appendix B). Parameters for equation (2): C = 10 MPa, friction values μ = 0.6 (solid), 0.7 (dash-dot), 0.8 (dashed), maximum compressive stress Δσ = 400 MPa. In the upper left corner dip-slip data from Fig. 2.8 a ($\delta_B \leq 5°$). **d) Dip-slip faulting schemes for NR and TH regimes:** arrows describe re-activation processes of dip-slip faults with dip β (see text): β_1 refers to low dip plane while β_2 to high dip plane.

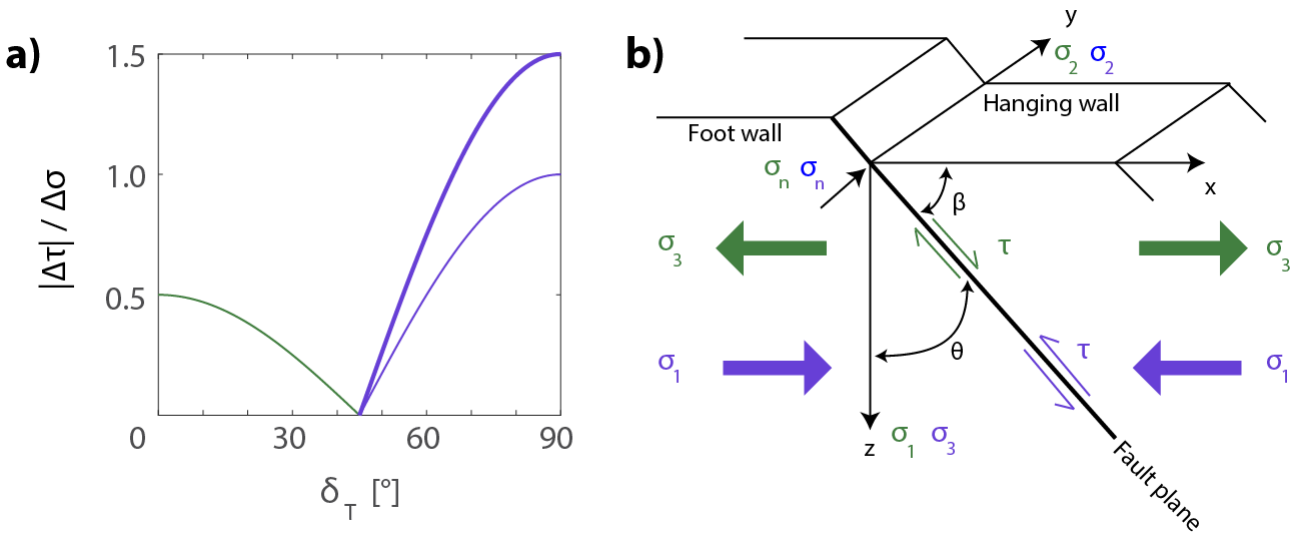

Figure 2.10. Anderson's dip-slip mechanisms. a) Shear stress τ – differential stress Δσ ratio as a function of δ_T for NR (green curve) and TH (blue curves. Thick and thin blue lines indicate that differential stress acting on a TH is three and two times the one acting on a NR respectively. **b) Dip-slip faulting schemes and principal axes orientations.** If one principal stress is always assumed to be along the vertical *z* and the intermediate one σ_2 lies on one horizontal directions *y*, the dip-slip faulting mechanisms are easily inferred and the tectonic stress $\Delta\sigma_{HV}$ acting on the fault is the differential stress $\Delta\sigma = \sigma_1 - \sigma_3$.

6. Conclusions for part 1

In this first part, a unified theory that links Anderson's faulting theory and differential-stress is exposed in a quantitative way with the relative earthquake size distribution, or *b*-value.

The analytical solutions (2.1, 2.2) are in good agreement with the global observations of *b*-values. In fact, they perfectly explain the first order observations: lowest *b*-values are observed for subduction zones and TH, highest *b* for extensional regimes and NR, and SS regimes are in between. In this way, the global *b*-value imaging draws a precise picture of the tectonic regime on the globe. It robustly differentiates extensive (high *b*) and compressive (low *b*) regimes from major continental transform faults and tectonically heterogeneous collision zones (intermediate *b*).

However, the analytical solutions also well explain second order variation that this analysis has revealed: theory predicts that the lowest *b*-value should not, as previously speculated by *Schorlemmer et al.* [2005], be observed for "pure" TH at 45° dip. Instead, they should occur at very shallowly dipping TH such as Chilean-style subduction zones. Likewise, as confirmed by observations, it is expected that the highest *b*-values should occur for NR to SS regimes, not for pure NR, thus at rake angles of 45° rather than 90°, as previously assumed.

Overall, it is highly remarkable how systematic the *b*-values vary with faulting style and how well this fits with simple geo-mechanical formulation based solely on Anderson's faulting theory introduced in 1905 and Mohr-Coulomb failure, dating back to 1776. It is especially remarkable given the known uncertainties in location, FM, and magnitudes, and given that faulting styles and tectonic regimes are known to be highly heterogeneous in many places.

The generic nature of the previously reported [*Schorlemmer et al*., 2005] dependence of *b*-values on rake angle has been proved to be time-independent, and confirmed with different choices of the γ-parameter. The ternary diagram analysis, constitutes a powerful new way to study *b*-values and their relationship to faulting. With *b*-value estimation within the plunge-based ternary representation of FMs [*Fröhlich*, 1992], we introduce a new tool to verify the *b*-value variation between different deformation regimes. Furthermore, this technique resolves, for the first time, *b*-value differences for different fault orientations within thrust and normal faulting regimes (visible but unexplainable through rake angle representation), as would be expected from Andersons' theory of faulting. The analytical model (2.2) that links *b*-values and stress can and should now be tested using independent data. This could be regional, high quality earthquake catalogs as well as lab based studies which link stress and faulting styles of acoustic emissions. Finally, by providing a theory linking differential-stress, faulting and *b*-values, a new and more quantitative avenue for seismic hazard analysis is provided.

To conclude, these findings provide a first strong supplementary set of clear evidences for the *b*-value dependence on differential stress combining faulting model and new data analysis techniques. The remarkable consistency between the systematic *b*-value patterns and the well-known global tectonic features reflects theoretically expected stress differences in all considered details. This part thus greatly improves the credibility that well-assessed *b*-value variations are meaningful for physical interpretation and consequently can provide valuable information for seismic hazard

assessment. The probabilistic hazard analyses in the future should consider the highly systematic variations as an important input and constrain when building seismogenic source models or earthquake simulators.

Part 3

HARMONIC FLUCTUATIONS OF *B*-VALUE AS A FUNCTION OF THE ANGLE OF RAKE

A. Petruccelli[1]

G. Vannucci[2], B. Lolli[2], P. Gasperini[1]

[1] Dipartimento di Fisica e Astronomia, University of Bologna, Italy; [2] Istituto Nazionale di Geofisica e Vulcanologia, Bologna, Italy

The slope (b-value) of the FMD of earthquakes might significantly vary as a function of the style of faulting. This behavior can be justified in terms of variations of the level of differential stress in different tectonic situations. In this part, we resume such hypothesis in the light of new data and of different procedures of analysis, also fitting a simple harmonic functional form for the dependence of b-value as a function of the rake angle λ. The fitted harmonic function is found to have a zero phase and a unit frequency thus indicating that b-value modulation is about proportional to −sinλ: b-value modulation appears to be about proportional to the work done by the gravity force during the earthquake slip. Finally, we also confirm the oscillating using a Tapered GR model on seismic moment, showing that the effect of high magnitude events is negligible for MLE approach.

1. Introduction

The frequency-magnitude distribution of earthquakes exhibits scale invariance and power law behavior that are well described by the GR law (1.1). This defines the empirical occurrence of the number N of earthquakes with magnitude M, in a given area and over a given time interval.

The general validity of the GR law has been tested by a number of studies concerning different distance scales and different tectonic situations, as explained in the introductory part and showed in the previous part. In paragraph 3 of part 2, we have updated global FM dataset and repeated the same algorithms of *Schorlemmer et al.* [2005], showing that the b-value continues to vary as a function of the style of faulting (e.g. rake angle λ), in particular that thrust-fault ($\lambda \sim$ -90°) events are associated with lower b-values (0.8-0.9) when compared with normal-fault events ($\lambda \sim 90°$ with $b \sim$ 1.1 - 1.2), while strike-slip faults ($\lambda \sim 0°, \pm 180°$) stay about in the middle between them with "constant" b ~ 1.

An important step forward of our analysis, with respect to 2004, is that, thanks to the increasing data availability for GCMT [*Ekström*, 2012], we reduce the γ-parameter (± 20°) for reliable estimations of b: apart from differences within normal and thrust faulting regimes, which can be explained by ternary FM analysis (see Part 2 paragraphs 4 and 5), the oscillating trend of b with λ is conserved. What can be done further is to provide a functional form of $b(\lambda)$, possibly with a physical origin, that fits the data. To get this, we need to disjoint each λ-subsets, to obtain b estimations coming from independent populations of FMs, and prove that estimations relative to different tectonic styles are statistically different each other.

We have also extended the analysis of *Schorlemmer et al.* [2005], by allowing for spatial variations of b-value (part 2 paragraph 2.2): we have detected high b-values along the oceanic ridges (where mechanisms are extensive and partially strike-slip), low b-values for subduction zones (where mechanisms are mostly compressive) and intermediate b-value for continental parts. However, we have noticed a degree of variability for subduction zones [*Uyeda*, 1982], linked to the age and the buoyancy of the subducted lithosphere [*Nishikawa and Ide*, 2014]. Therefore, we also want to test the existence of a spatial link between variations of the style of faulting and of the b-value by determining the rake and the b-value separately from the GCMT catalog and from a homogenized version of the Bulletin of the ISC (see part 1 paragraph 6.2) respectively, based on a spatial tessellation of the Earth's surface.

Several other studies report variations of the b-value. However, *Kagan* [1999, 2002a, 2003, 2005, 2010] and *Bird and Kagan* [2004] argued that they are statistically insignificant or due to technical artifacts (see part 1 paragraph 3.1), claiming on universal constancy of the b-value. Then, variability in the measured b (or b^*) can be explained through inappropriate usage of magnitude [*Kagan*, 1999; 2003], considering usage of corner moment magnitude m_C - which can vary for different tectonic styles (higher for thrust regimes and lower for normal regimes) - and of tapered GR model (1.25) [*Kagan*, 1991a, 2002a; *Bird and Kagan*, 2004]. We also allow for the usage of this model in our computations, proving that the effect of m_C on b is instead negligible.

2. Data and methods

2.1 Datasets

We use the same (1980-2016, z=0-50 km M_c=5.5) GCMT catalog of part 2 and a revised version of the ISC catalog (see part 1 paragraph 6.3), from 1990 to 2012. We convert M_s and m_b to M_w using the empirical relations derived by *Lolli et al.* [2014, 2015] and use such proxies if M_w not available from moment tensor (MT) catalogs for the given earthquakes. We again restrict the analysis to shallow earthquakes (depth 0-50 km) occurred after 1990, when the completeness of the ISC Bulletin improved significantly with respect to previous times. Consistently with *Schorlemmer et al.* [2005], we binned all magnitudes in both catalogues to ΔM=0.1.

2.2 Harmonic model derivation

In general, the proportion of large earthquakes seems to increase (low *b*-value) in high-stress environments (compressional, deep brittle crust, young subducted lithosphere) and to decrease (high *b*-value) in low-stress environments (extensional, shallow crust, old subducted lithosphere). Actually *Scholz* [1968] and *Amitrano* [2003] demonstrated the dependence of the *b*-value on the state of stress for rock microfractures in laboratory experiments and *Scholz* [2015] derived a negative dependence on differential stress $\sigma_1 - \sigma_3$ of *b*-values measured as a function of depth and in different tectonic environments as (1.28). Equation (1.28) gives the typically observed average value of ~ 1, by assuming a differential stress $\Delta\sigma = 200$ MPa. A decrease and an increase in stress conditions determine higher and lower *b*-value respectively.

The oscillating behavior of *b*-value with rake angle, as shown by *Schorlemmer et al.* [2005] and confirmed in previous part, suggests the existence of a functional relationship between the *b*-value and the rake. This can be deduced from the hypothesis that, as proposed by *Anderson* [1905] and by *Turcotte and Shubert* [2002], gravity favors the slip on normal faults and opposes the slip on reverse faults. That means that the differential stress required to slip a normal fault should be lower than that required for a reverse fault while for a strike-slip fault it should stay about in the middle between the other two fault types.

We could hypothesize the differential stress be a linear function of the along-dip component of the slip vector $\hat{d}$ that is a linear function of the sine of the rake λ (see Fig. 3.1)

$$\Delta\sigma = \sigma_1 - \sigma_3 \cong \sigma_a + \Delta(\sigma_1 - \sigma_3)\sin\lambda \tag{3.1}$$

where σ_a is the average differential stress and $\Delta(\sigma_1 - \sigma_3)$ is the (positive) amplitude of differential stress perturbation. Combining (1.28) and (3.1)

$$b(\lambda) = b_r - k[\sigma_a + \Delta(\sigma_1 - \sigma_3)\sin\lambda] = b_0 - \alpha\sin\lambda \tag{3.2}$$

where

$$b_0 = b_r - k\sigma_a \tag{3.3}$$

is the offset of the sinusoidal model (related to the average differential stress) while

$$\alpha = k\Delta(\sigma_1 - \sigma_3) \tag{3.4}$$

represents the amplitude of the oscillations, that are more pronounced if higher differential stresses are allowed.

In order to make the testing of such functional form more stringent, one can allow even the frequency ω and the phase φ of the sinusoidal function to vary freely. In this case the function (3.2) to actually fit on data becomes

$$b(\lambda) = b_0 - \alpha \sin(\omega\lambda + \varphi) \tag{3.5}$$

where ω and φ are dimensionless frequency and an angle of phase respectively.

Variation of b with rake angle λ would correspond to the scalar product between the unit versors of the gravity force component along the fault plane g and of the co-seismic displacement d (see Fig. 3.1)

$$-\sin\lambda = \cos\left(\lambda + \frac{\pi}{2}\right) = \cos\left(\lambda - \left(-\frac{\pi}{2}\right)\right) = \hat{g} \cdot \hat{d} \approx \Delta b \tag{3.6}$$

This means that the deviations from the average b-value (~ 1) is about proportional to the amount of mechanical work done by the gravitational force during the earthquake. This inference might represent anyhow a valuable clue to understand the physical mechanism producing such b-value variations.

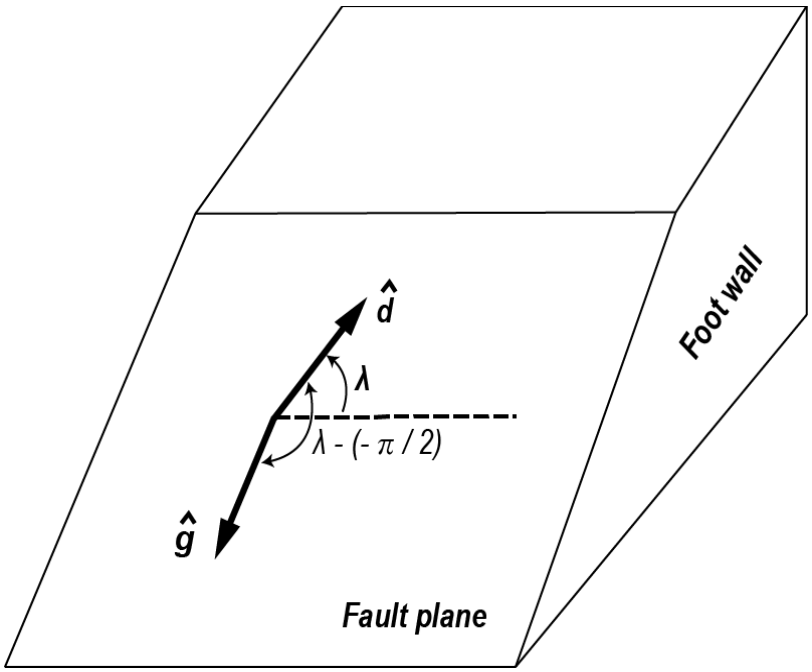

Figure 3.1. Unit versors of the co-seismic displacement (slip) $\hat{d}$ and of the component of the gravity force along the fault plane.

2.3 Mechanisms selection and inequality tests

The rake λ is the parameter that represents the deformation style of an earthquake (see Figs. 1.3, 3.1): λ=-90° indicates a pure normal (NR) extensional fault, λ=90° a pure reverse thrust (TH) fault and λ=0° and λ=±180° pure strike-slip (SS) faults, left-lateral and right-lateral respectively. Other values indicate mixed mechanisms: trans-tensive or trans-pressive, depending on the sign of λ (negative or positive respectively). *Schorlemmer et al.* [2005] analyzed various focal mechanisms datasets by selecting, for each of the two focal planes, sub-catalogs of earthquakes with λ within moving windows (by moving with a step rake of 5° from -180° to 180°) with width γ (ranging from 60° to 120°), depending on the used datasets (see Fig. 1.9). Then, they estimated the *b*-value of each subcatalog using the maximum likelihood estimation approach [*Aki*, 1965] (eq. 1.8) and plotted it versus the central value of rake λ_c of each moving window.

Differently from *Schorlemmer et al.* [2005] and from what we have done in the previous part, we now use disjointed datasets of similar rake. Since we want to fit a curve to independent *b* estimations, we need to set the step rake to be equal to γ, using a value of 30° (so λ_c ± 15°), obtaining 12 disjointed datasets (from -180° to 150° with a step of 30) of common rake events.

As the rake windows are all disjointed, we can statistically test for the inequality of their *b*-values. We use both the non-parametric tests based on the *Akaike* (1974) criteria, specifically developed by *Utsu* (1966, 1999) for comparing *b*-values, and the t-student test for the equality of two estimates given their errors, which assumes instead a normal distribution. For the first criterion, we compute probability P_b that the two *b*-values are not different

$$P_b = \exp\left\{-\frac{1}{2}\left[-2(N_1+N_2)\ln N + 2N_1 \ln\left(N_1 + N_2\frac{b_1}{b_2}\right) + 2N_2 \ln\left(N_2 + N_1\frac{b_2}{b_1}\right)\right]\right\} \tag{3.7}$$

where N_1, b_1 and b_2, N_2 are the number of events and the estimated *b* for two selected groups (1 and 2). For the second one we estimate the significance level (SL) of the equality hypothesis, i. e. the probability P_b of being wrong in rejecting a true H_0 hypothesis of equality,

$$P_b = 2\int_t^\infty \frac{\Gamma\left(\frac{\nu+1}{2}\right)}{\Gamma\left(\frac{\nu}{2}\right)} \frac{1}{\sqrt{\nu\pi}} \frac{1}{\left(1+\frac{x^2}{\nu}\right)^{\frac{\nu+1}{2}}}\, dx \tag{3.8}$$

if the *t*-value is

$$t = \frac{|b_1 - b_2|}{\sqrt{\frac{(N_1-1)\sigma_{b_1}^2 + (N_2-1)\sigma_{b_2}^2}{N_1+N_2-2}}} \tag{3.9}$$

where ν are the degrees of freedom, Γ is the Gamma-function and $\sigma_{b_{1,2}}$ are the standard deviations of the two *b*-values. For the t-test, according to the statistical practice, the equality hypothesis can be rejected (and then the inequality accepted) with confidence for SL < 0.05 and with high confidence for SL < 0.01.

2.4 Choice of the nodal planes: gaussianity tests on *b*-value distributions

Computations can be performed for both focal planes (see Fig. 2.7): smoothed oscillating behaviors are expected with maximum at or close to λ=-90° and minimum at or close to λ=90°. However, sometimes, the plots for the two nodal planes might appear slightly different one to the other (see Fig. 1.9). Note that the ordering of the two planes provided by MT catalogs is not related to any physical arguments but rather to the computational practice as the real fault plane cannot be distinguished from the auxiliary one based on seismological arguments only. Consequently, the distribution of fault parameters within the two planes might be not the same because computational algorithms might select them based on predefined criteria. To overcome such inconveniences, it is possible to randomize the choice of the planes (i.e., randomly distinguish the real plane from the auxiliary one), or to stack them (and obtain only one b(λ) trend). The stack of the nodal planes (which consist in selecting all the possible solutions for both planes in a unique, comprehensive rake selection) is the technique we adopt for the data trend to which perform the sinusoidal regressions (3.2) (3.5).

When two different estimations of *b*-value are obtained from two groups of earthquakes and we have to decide whether their difference is significant, we refer to the Utsu test (3.7) in order to compute to probability of being wrong in rejecting the null hypothesis that the two groups of earthquakes have the same *b*-value. Similarly, for the t-student test (3.8, 3.9), we compute the probability in being wrong in rejecting the hypothesis of different *b*-values: but, in this case, each of the two populations should follow a normal distribution, which is not automatically guaranteed for *b*-values. In fact, as reported by *Utsu* [1966], the MLE *b*-values would not follow a symmetric probability distribution. However, in the above work, b was considered constant in time, while variations of *b*-value with time are widely reported in literature.

Aki [1965] showed that, for large samples, the GR PDF tend to a normal distribution with zero mean and variance $\sigma_b^2 = \frac{N}{b^2}$. On the other side, by the theorem of the central limit, for large N, the distribution function of magnitudes M approaches to a normal distribution, if the M_i are independent, evenly distributed, with finite mean and variance σ_M^2. In fact, according to *Shi and Bolt* [1982], the PDF of the MLE *b*-value can be considered normal, for large number of events assuming slow temporal b variations: the standard error associated to b is $\sigma_B = 2.30\ b^2\ \sigma_M$ (see eq. 1.6).

We therefore test the gaussianity of our distributions in two steps:

1) we randomize 1000 times the choices of the nodal planes;
2) we perform 1000 repetitions of the stacked dataset by bootstrap sampling [*Efron*, 1987; *Efron and Tibshirani*, 1993] (the bootstrapped dataset contains the same number of events of the original one but with possible replies).

For each iteration, we compute *b*-values with the standard procedure, and we finally obtain three different distributions of *b*-values with rake angle λ (randomized plane 1, 2 and bootstrapped stacked dataset). In order to test the data to be normal distributed, we perform a *Lilliefors* [1967; 1969] test: it returns a test decision for the null hypothesis that the data come from a normal distribution

(at the 5% significance level). The *p*-value is the probability in being wrong by rejecting the null hypothesis: hence, small values of *p* carries doubts on the validity of the gaussianity.

2.5 GCMT-ISC spatial analysis

In GCMT b(λ) analysis, earthquakes are assigned to different rake windows independently on their spatial location then the results shown do not indicate if there is a spatial coherence between styles of faulting and *b*-values. In the following, we adopt a different strategy that takes into account the spatial locations of earthquakes by determining the rakes and the *b*-values separately from different datasets and associating them to each other based on spatial criteria.

We determine the rakes from the GCMT catalog and the *b*-values from the hypocentral catalog of earthquakes provided by the Bulletin ISC with M_s and m_b magnitudes converted to M_w according to relations determined at the global scale by *Lolli et al.* [2014, 2015]. To combine the two datasets, we subdivide the mechanisms and the hypocentral data by a tessellation of the Earth surface in cells of 5°×5° in latitude and in longitude. For each cell, we compute a cumulate MT by summing all the individual MTs from the GCMT catalog belonging to the cell [*Kostrov*, 1974] (see part 1 paragraph 2.6). Then we determine the largest double couple by the decomposition of the cumulate MT according to the Harvard CMT standard procedure (see for details *Gasperini and Vannucci*, 2003). We only consider cells in which the size of the Compensated Linear Vector Dipole (CLVD) component of the cumulate MT is lower than 15% (as done in part 1), because a larger CLVD size might indicate tectonic heterogeneity of the cell (note that using the Harvard CMT decomposition method the maximum possible CLVD size is 25%).

2.6 Tapered GR model

Finally, as suggested by *Kagan* [1999, 2002a, 2003, 2005, 2010], we consider moving from the "pure" GR model to the tapered GR model (1.25), to see if effectively variations of *b*-values are related to the absence of a corner magnitude. Hence, we follow the MLE procedure in *Bird and Kagan* [2004] by numerically maximizing the Loglikelihood function (see Appendix A)

$$L = \sum_i \ln\left[\frac{b^*}{m_i} + \frac{1}{m_c}\right] + N b^* \ln m_T - b^* \sum_i m_i + \frac{1}{m_c}\{N m_T - \sum_i m_i\} \tag{3.10}$$

and we simultaneously estimate the asymptotic *b*-value, b^* which is related to the "classic" GR *b*

$$b^* = \frac{2}{3}\, b \tag{3.11}$$

in addition to the corner moment magnitude m_c. However, the loglikelihood function (3.10) presents some convergences problems (as we tested), since some bias in MLE estimations can be reported [*Kagan*, 2002a]. In particular, the successfully of the optimization algorithm strongly depends on the choice of the starting point (see *Bird and Kagan* [2004]).

In implementing the MLE method, we assume as initial estimates a "universal" b-value b^* of $\frac{2}{3}$ ($b = 1$) and a corner moment of

$$m_{c_0} = \frac{\frac{\sum_{i=1}^{N} m_i^2}{N} - m_t^2}{2\left[m_t b^* + (1-b^*)\sum_{i=1}^{N} m_i\right]} \tag{3.12}$$

according to *Kagan and Schoenberg* [2001]. All the magnitude M_w are converted to seismic moment m according to *Kanamori* [1979]'s formula (1.37). We set the moment threshold to $\sim 1.99\ 10^{17}$ N m (corresponding to $M_w = 5.5$).

3. Results

3.1 GCMT: harmonic fluctuations of b-value with rake λ

In paragraph 2.3 we state that it is impossible to distinguish between the two available focal plane solutions the real one from the auxiliary one, and that such inner ambiguity can affect the events distribution of the tectonic styles. In Fig. 3.2 (top panels) we can see how the frequencies of rakes for the GCMT catalog are rather different for the two original focal planes. In particular, mechanisms close to a pure strike-slip (λ=0° and λ=±180°) are definitely more frequent in plane 1 (red histogram on the left) than in plane 2 (dashed blue histogram on the right). As well mechanisms close to a pure thrust (λ=90°) are more frequent in plane 2 than in plane 1. In Fig. 3.2 (middle panels) we show that the distributions of rakes in the two sets become rather similar to each other when the mechanisms are selected randomly from one of the two planes. The distribution of both randomly selected sets is also very similar to that can be obtained by staking the frequencies of the rakes of the two original planes in a single histogram (Fig 3.2 bottom).

The asymmetry of the distributions of rakes between the two planes provided by the GCMT catalog has also some consequences on the estimated b-values within different, disjointed rake windows. In Fig. 3.3 (top left panel) we show the behavior of b-value as a function of the central rake of disjointed windows with width γ = 30° (±15°) for the two planes as provided by the GCMT catalog. We can note how in some windows (e.g. λ = −150°, −30°, 120°) the differences between the b-values computed by the two planes are definitely larger than their respective uncertainties computed according *Shi and Bolt* [1982]. Again, the maximum values are not found in correspondence of the pure-normals (λ = 90°) for both planes, as showed in part 1 (see paragraph 5).

Using instead the two randomly selected sets (Fig. 3.3 top right panels) the differences of b-value decrease significantly and, in most cases, stay well within the uncertainties. On the other hand, the b-values computed from subsets obtained by stacking the earthquakes selected by both planes (Fig. 3.3 bottom panel) stay about in the middle between the two randomly extracted planes.

In Table 3.1 and 3.2 we report Pb for the Utsu test (3.7) and SL for the t-test (3.8) respectively for all pairs of rake windows computed from the GCMT dataset by stacking the two planes (Fig. 3.3, bottom). Also note in Table 3.1 that the numbers N of data used to compute b-values for are of the order of several hundreds or of a few thousands for all rake windows. The pairs for which the

inequality is significant are evidenced in light gray and those for which it is highly significant in dark gray. For all comparisons between "pure" fault styles (cells bordered with rectangles) both tests indicate that the inequality of *b*-values is highly significant. The inequality is also significant or highly significant over wide ranges of rakes for the comparisons between mechanisms around NR and around TH. Also note that, consistently with the hypotheses made, the inequality is not significant between pure right lateral ($\lambda = \pm 180°$) and left lateral ($\lambda = 0°$) SS mechanisms.

As the rake windows are all disjointed, the corresponding earthquake datasets are independent and then we can use the *b*-values computed within the various windows to fit the harmonic model described in 2.2. We perform an unconstrained weighted least-square regressions of eq. 3.2 (red dotted line in Fig. 3.3) and of eq. 3.5 (black dashed line in Fig. 3.3) on the *b*-values computed in different windows as a function of the central rake λ. The covariance matrix is computed as the inverse of the finite difference Hessian of the minimized sum of squares and the standard errors of the best-fit parameters are computed as the square roots of the corresponding diagonal elements.

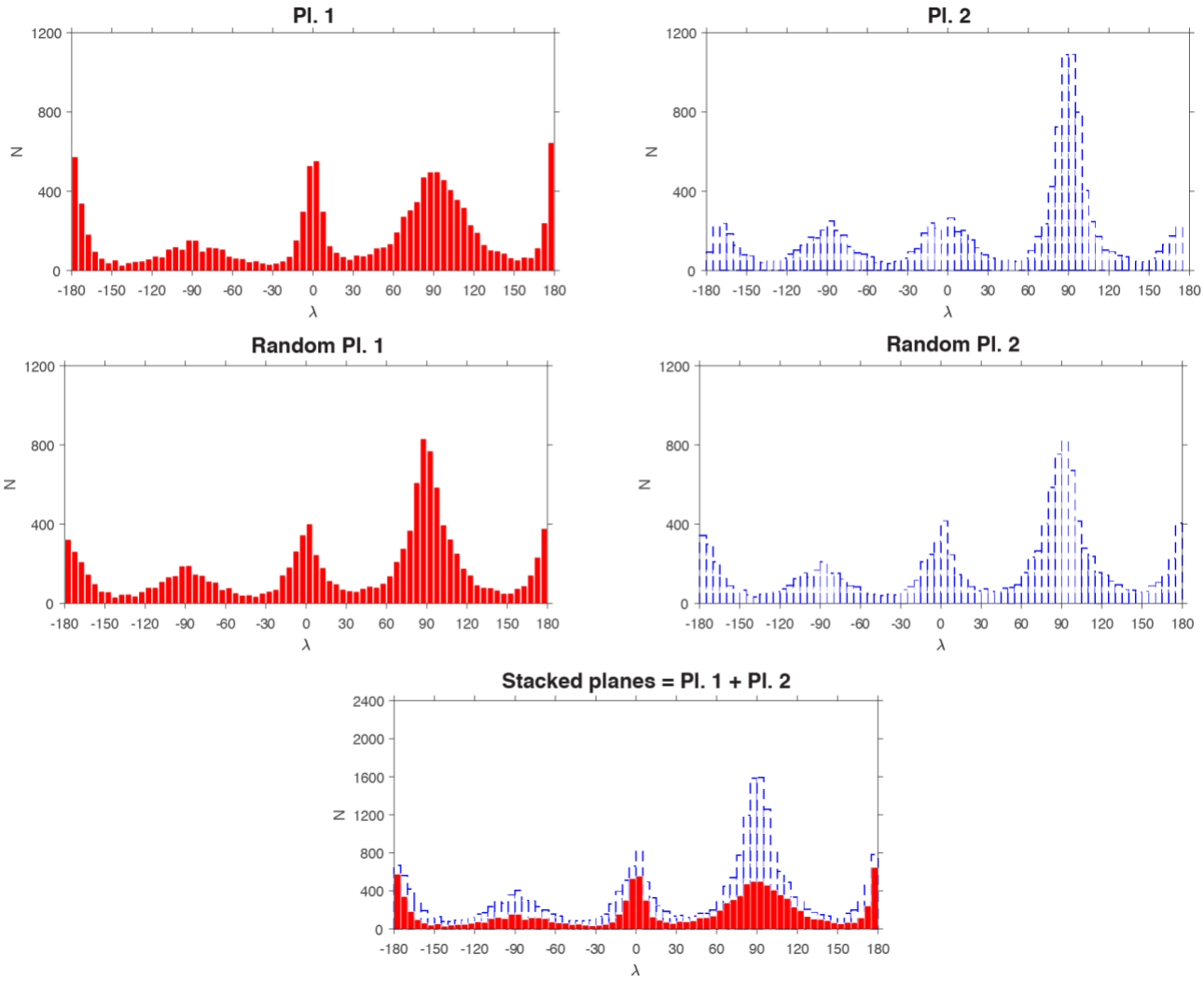

Figure 3.2. Histograms of the number of events as a function of rake angle λ for the two nodal planes provided by the GCMT catalog (top), for two sets selected randomly from the two planes (middle) and for the stacking of the two planes (bottom).

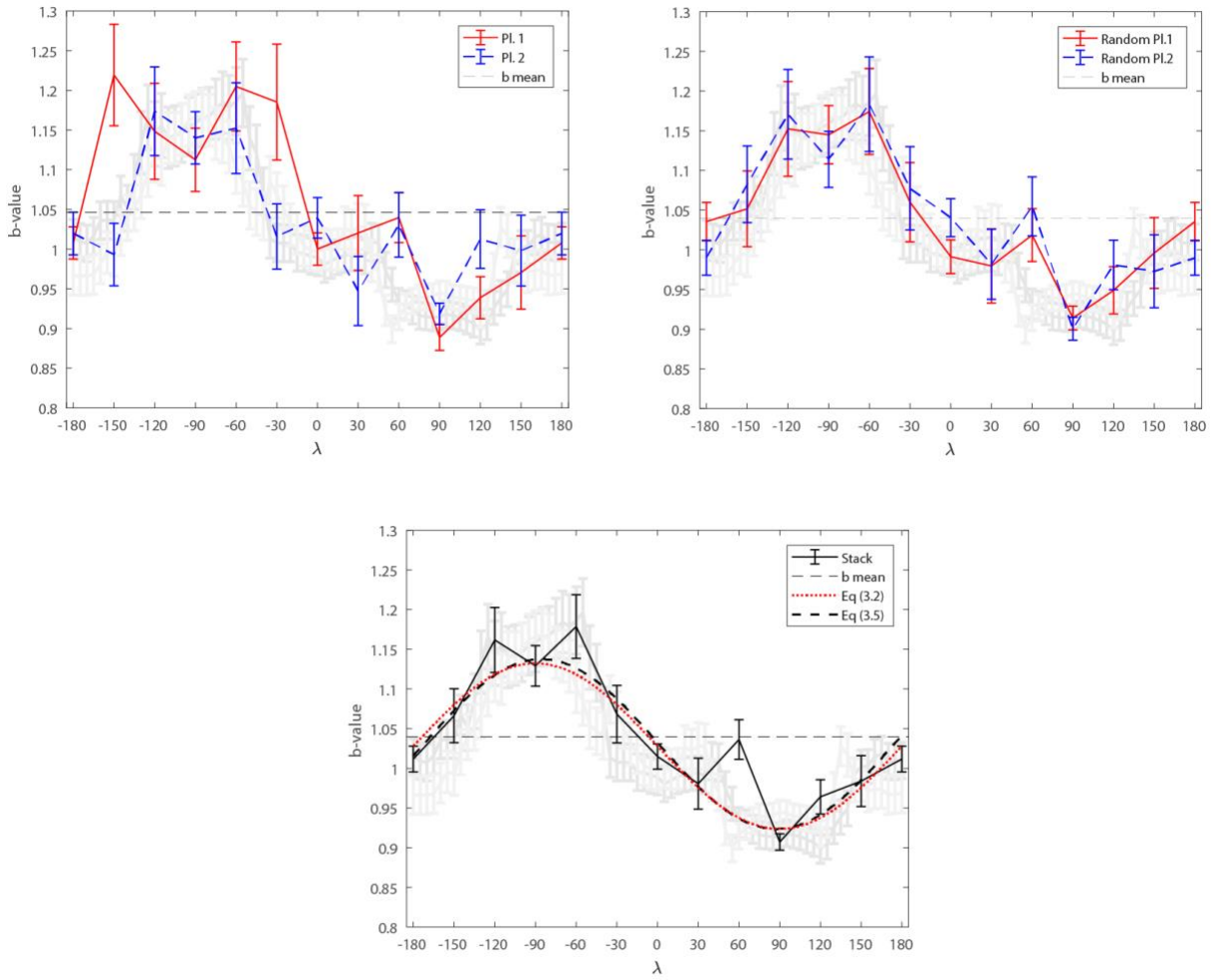

Figure 3.3: *b*-value as a function of the central rake λ_c of windows with width of γ=30° (GCMT), for original nodal planes provided by the catalog (top left), for two sets selected randomly from the two original planes (top right) and for the stacking of the two planes (bottom). In light gray the results obtained by *Schorlemmer et al.* (2005) and reproduced in part 1. In bottom panel, the dotted and thick dashed lines indicate the fitted sinusoidal curves according to eq. (3.2) and (3.5) respectively.

			SS		NR			SS			TH			
			±180	**-150**	**-120**	**-90**	**-60**	**-30**	**0**	**30**	**60**	**90**	**120**	**150**
λ_c	**N**	**b**	1,01	1,07	1,16	1,13	1,18	1,07	1,02	0,98	1,04	0,91	0,96	0,98
±180	3191	1,01	1	0.39	0	0	0	0.39	0.99	0.70	0.72	0	0.23	0.77
-150	876	1,07	0.39	1	0.20	0.37	0.11	1	0.44	0.20	0.79	0	0.05	0.24
-120	877	1,16	0	0.20	1	0.78	0.95	0.23	0	0	0.02	0	0	0
-90	1919	1,13	0	0.37	0.78	1	0.57	0.42	0	0	0.03	0	0	0
-60	914	1,18	0	0.11	0.95	0.57	1	0.13	0	0	0.01	0	0	0
-30	814	1,07	0.39	1	0.23	0.42	0.13	1	0.43	0.20	0.77	0	0.05	0.24
0	3212	1,02	0.99	0.44	0	0	0	0.43	1	0.64	0.78	0	0.19	0.72
30	965	0,98	0.70	0.20	0	0	0	0.20	0.64	1	0.38	0.08	0.91	1
60	1811	1,04	0.72	0.79	0.02	0.03	0.01	0.77	0.78	0.38	1	0	0.08	0.45
90	7223	0,91	0	0	0	0	0	0	0	0.08	0	1	0.05	0.08
120	2101	0,96	0.23	0.05	0	0	0	0.05	0.19	0.91	0.08	0.05	1	0.88
150	871	0,98	1	0.39	0	0	0	0.39	0.99	0.70	0.72	0	0.23	0.77

Table 3.1: For the GCMT stacked dataset, Utsu-test probabilities (P_b) for *b*-values of various rake windows not being different to each other. Cells in light and dark gray evidence, according to *Schorlemmer et al.* (2005), significant (≤ 5%) and highly significant (≤ 1%) differences. *N* is the number of earthquakes in each rake window. Cells bordered by rectangles correspond to comparisons between pure mechanisms (SS: λ = 0°, ± 180°; NR: λ = -90°; TH: λ = 90°).

			SS		NR			SS			TH			
			±180	**-150**	**-120**	**-90**	**-60**	**-30**	**0**	**30**	**60**	**90**	**120**	**150**
λ_c	**N**	**b**	1,01	1,07	1,16	1,13	1,18	1,07	1,02	0,98	1,04	0,91	0,96	0,9
±180	3191	1.01 ± 0.02	1	0,01	0	0	0	0,01	0,85	0,14	0,21	0	0,01	0,18
-150	876	1.07 ± 0.03	0,01	1	0,01	0,03	0	0,95	0,02	0,01	0,29	0	0	0,01
-120	877	1.16 ± 0.04	0	0,01	1	0,29	0,68	0,02	0	0	0	0	0	0
-90	1919	1.13 ± 0.03	0	0,03	0,29	1	0,11	0,04	0	0	0	0	0	0
-60	914	1.18 ± 0.04	0	0	0,68	0,11	1	0	0	0	0	0	0	0
-30	814	1.07 ± 0.04	0,01	0,95	0,02	0,04	0	1	0,01	0,01	0,27	0	0	0,01
0	3212	1.02 ± 0.02	0,85	0,02	0	0	0	0,01	1	0,1	0,28	0	0,01	0,13
30	965	0.98 ± 0.03	0,14	0,01	0	0	0	0,01	0,1	1	0,04	0	0,51	0,92
60	1811	1.04 ± 0.03	0,21	0,29	0	0	0	0,27	0,28	0,04	1	0	0	0,06
90	7223	0.91 ±0.01	0	0	0	0	0	0	0	0	0	1	0	0
120	2101	0.96 ± 0.02	0,01	0	0	0	0	0	0,01	0,51	0	0	1	0,43
150	871	0.98 ± 0.03	0,18	0,01	0	0	0	0,01	0,13	0,92	0,06	0	0,43	1

Table 3.2: For the GCMT stacked dataset, significance levels (SL) for the T-student test of equality between *b*-values computed for different rake windows. For cells evidenced in light and dark gray, the equality hypothesis can be rejected with confidence (SL < 0.05) and high confidence with (SL < 0.01) respectively. "0" indicates SL <0.005 and "1" SL > 0.995. Bordered cells correspond to comparisons between pure mechanisms (SS: $\lambda = 0°, \pm 180°$; NR: $\lambda = -90°$; TH: $\lambda = 90°$).

Dataset	Model	b_0	α	ω	SL (ω=1)	φ	SL (ω=0)
GCMT	Eq. (3.5)	1.031±0.013	0.107±0.017	1.039±0.086	0.66	-1.0°±9.6°	0.92
GCMT	Eq. (3.2)	1.028±0.011	0.104±0.015	-		-	
ISC	Eq. (3.5)	1.178±0.027	0.196±0.035	1.054±0.084	0.53	6.8°±9.9°	0.51
ISC	Eq. (3.2)	1.178±0.025	0.187±0.032	-		-	
GCMT (Tapered GR)	Eq. (3.5)	1.025±0.014	0.106±0.017	1.019±0.099	0.85	-3.1°±10.9°	0.78
GCMT (Tapered GR)	Eq. (3.2)	1.024±0.011	0.099±0.015	-		-	

Table 3.3: Parameters of fitted harmonic functions of *b*-values as a function of rake for different datasets and equations. SL(H_0: $\omega = 1$) and SL (H_0: $\varphi = 0$) indicate the t-test probabilities to be wrong in rejecting the H_0 hypotheses that $\omega = 1$ and $\varphi = 0$ respectively, if they are actually true.

In Fig. 3.3 (bottom) and Table 3.3 we report respectively the plot and the coefficients of the harmonic function fitted on the stacked dataset. The t-test indicates that the dimensionless frequency $\omega = (1.039 \pm 0.086)$ is not significantly different from 1 and that the angle of phase $\varphi = (-1.0° \pm 9.6°)$ is not significantly different from 0°. This means that the *b*-value behavior is actually well described even by eq. (3.2). The other fitted coefficients are also reported in Table 3.3.

From the fitted value (using eq. 3.2) of the average *b*-value $b_0 = (1.031 \pm 0.013)$, we can estimate the average differential stress as

$$\sigma_a = \frac{1}{k}(b_r - b_0) \cong (166 \pm 44) \text{ MPa} \quad (3.13)$$

that would correspond to the differential stress required to slip a pure SS fault. From the fitted value of the amplitude of *b*-value variations $\alpha = (0.107 \pm 0.017)$, we can estimate the amplitude of differential stress variations as

$$\Delta(\sigma_1 - \sigma_3) = \frac{\alpha}{0.0012} \cong (89 \pm 36) \text{ MPa} \quad (3.14)$$

Hence, the average differential stress for slipping a pure normal fault would be

$$\Delta\sigma_{NR} = 166 + 89\sin(-90°) \cong (77 \pm 80) \text{ MPa} \quad (3.15)$$

and the average differential stress for slipping a pure reverse fault would be

$$\Delta\sigma_{TH} = 166 + 89\sin(90°) \cong (255 \pm 80) \text{ MPa} \quad (3.16)$$

Such values are rather consistent with those expected based on the modeling of friction on dip-slip faults (*Turcotte and Schubert*, 2002): thrust faulting requests an amount of stress which is about three times the one requested for normal faulting (see also Appendix B).

3.2 ISC: spatial coherence of the b(λ) trend

In Fig. 3.4 we repeat the same analysis of the GCMT for the ISC catalog (top panels). We also report the geographical distribution of considered cells (5° x 5°) with different colors indicating the 12 rake windows to which they belong (bottom panels).

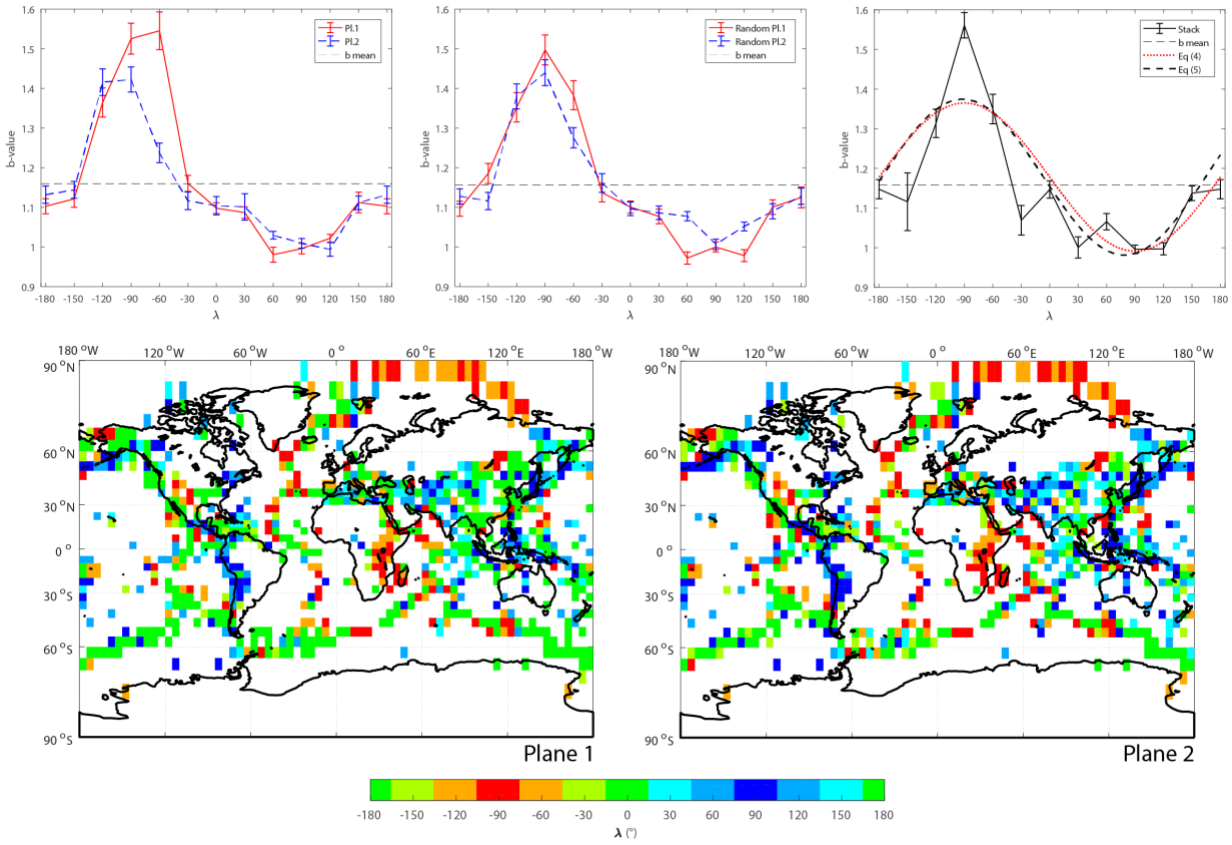

Figure 3.4: ISC dataset *b*-value analysis (1990-2012, z=0-50 km). In top panels, same as GCMT catalog (on the left the original solutions, in the middle one possible randomization, on the right the stacked solution with the regression curves). In lower panels, geographical cells used in computations (with CLVD component of the cumulate moment tensor lower than 15%). Colors indicate the rake windows to which they belong according to plane 1 (left) and plane 2 (right) (see text).

We can note a fair coherence between the two planes and, as expected, the abundance of cells with TH mechanisms (blue) along trenches and with NR mechanisms (red) along ridges. If we compare the global seismotectonic characterization of Fig. 3.4 with the GCMT *b*-value map (Fig. 2.3) it is interesting to note the correspondences between high *b*-values (yellow to red dots in Fig. 2.3, oceanic ridges, continental rifts and old subduction zones) and zones with MT sum solutions of rake ~ -90° and between low *b*-values (cyan to purple dots in Fig. 2.3, young subduction zones) and zones with MT sum solutions of rake ~ 90°. Cells with SS mechanisms (green) along ridges can be explained by

the presence of transform faults and intermediate *b*-values (Fig. 2.3). The consistency of b(λ) trend and spatial distribution of *b*-values has already been evidenced in part 2 paragraph 3 while, here, we strengthen this link through the application of *Kostrov* [1974] summation method.

Then, we compute the *b*-value from sub-sets of the ISC hypocentral catalog obtained by merging earthquakes belonging to all cells for which the rake λ of the largest double couple lies within disjointed windows with width γ=30°. As the completeness of the ISC catalog might vary in different tectonic zones, we separately compute the completeness magnitude M_c for each sub-set using the MBS method by *Cao and Gao* [2002] (as implemented by *Woessner and Wiemer*, 2005, see part 1 paragraph 1.2), which evaluate the stability of the *b*-value as a function of the cut-off magnitude.

In Fig. 3.4 top left panel we show the behavior of *b*-value as a function of the central rake for the two nodal planes as computed by our codes. Even in this case we can note how in some windows (e.g. $\lambda_C = -90°, -60°$) the differences between the *b*-values computed by the two planes are definitely larger than the respective uncertainties while for the two randomly selected sets (Fig. 3.4 top middle) the differences of *b*-value generally decrease. The behavior of *b*-value computed from a set composed by stacking the two planes (Fig. 3.4 top right) is somehow different from *b*-values of the two randomly selected sets (Fig. 3.4 top middle), probably owing to the variable completeness approach we adopted in this case, but the amplitude of *b*-value variations is substantially consistent.

We can see in Fig. 3.5 (top panels) that even in ISC cases the rakes (computed this time by our own codes, see Methods) are unevenly distributed between the two focal planes with a larger number of cells with mechanism close to a pure SS in plane 1 (Fig. 3.5 top left) than in plane 2 (Fig. 3.5 top right). Analogously to the previous case, Fig. 3.5 middle panels show that the distributions of rakes become rather similar for two sets randomly selected from the two original planes and that distribution of both random sets is quite similar to that can be obtained by staking in a single histogram the frequencies of cells with rakes from both original planes (Fig. 3.5 bottom).

In Table 3.4 and 3.5 we report the values of Pb for the Utsu test (3.7) and of SL for the t-test (3.8) respectively for all pairs of *b*-values computed from the ISC dataset. The inequality of *b*-values is highly significant for both tests in all combinations between "pure" fault styles (bordered cells) and is also significant or highly significant over wide ranges of rakes for comparisons between mechanisms around NR and around TH.

Even for this dataset we fitted the harmonic functions of eq. (3.2) and (3.5) on *b*-values of the stacked set. As in case of GCMT dataset, the T-student test indicates that the dimensionless frequency $\omega = (1.054 \pm 0.084)$ is not significantly different from 1 and that the phase $\varphi = (6.8 \pm 9.9°)$ is not significantly different from 0 and then eq. (3.2) well describes the behavior of *b*-values (see Table 3.3).

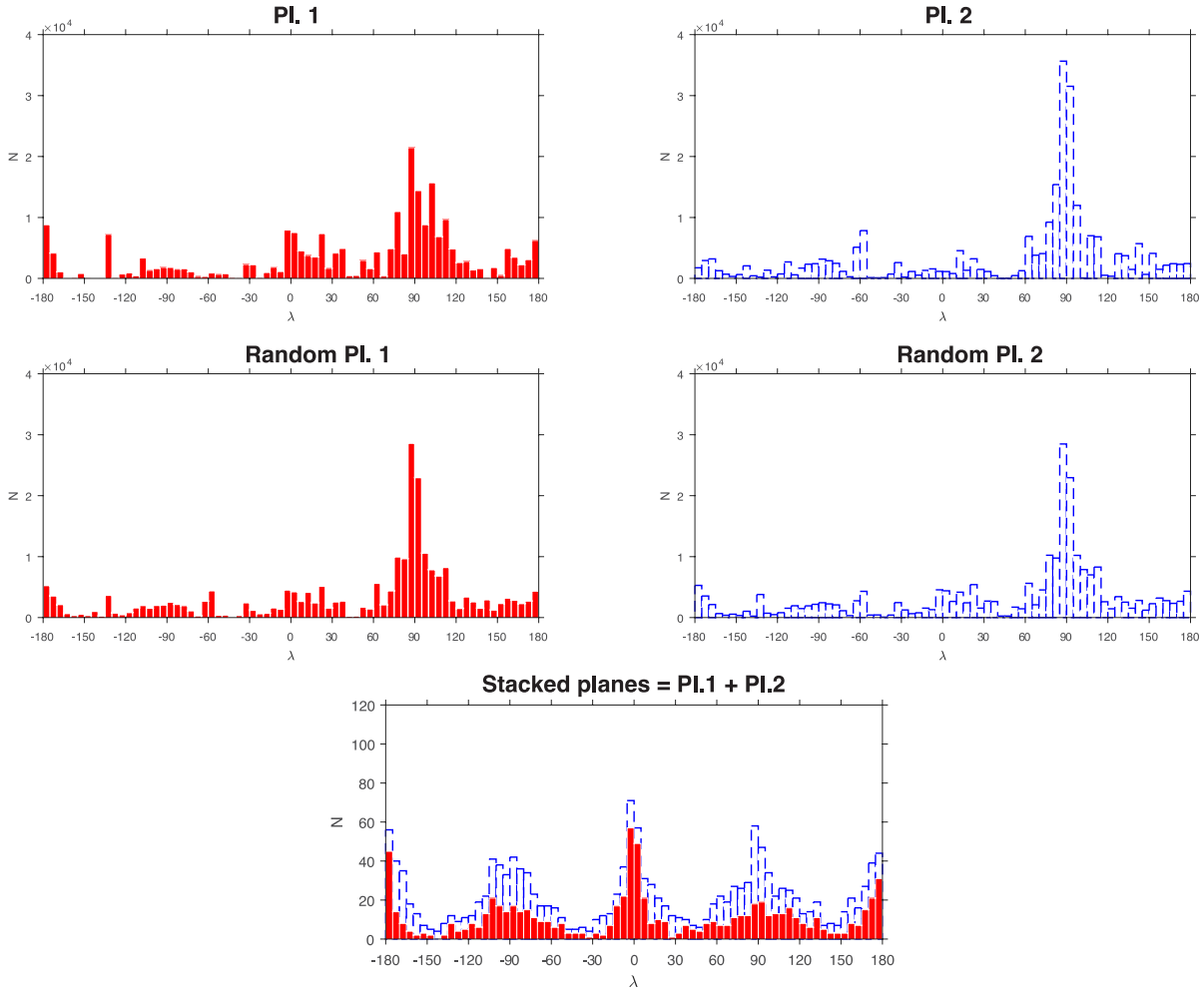

Figure 3.5: Histograms of the number of 5°x5° spatial cells as a function of the rake λ computed from cumulate mechanisms (see text) for the two nodal planes as computed by our codes (top), for two sets randomly selected from the two planes (middle) and for the stacking of the two planes (bottom).

				SS		NR			SS			TH			
				±180	**-150**	**-120**	**-90**	**-60**	**-30**	**0**	**30**	**60**	**90**	**120**	**150**
λ_c	**M_c**	**N**	**b**	1,15	1,12	1,31	1,56	1,35	1,07	1,15	1,00	1,07	1,00	1,00	1,14
±180	5,5	2063	1,15	1	0,91	0	0	0	0,23	1	0	0,04	0	0	0,95
-150	5,4	260	1,12	0,91	1	0,05	0	0,02	0,84	0,91	0,28	0,78	0,21	0,22	0,96
-120	5,2	1353	1,31	0	0,05	1	0	0,79	0	0	0	0	0	0	0
-90	5,1	2355	1,56	0	0	0	1	0	0	0	0	0	0	0	0
-60	5,2	1231	1,35	0	0,02	0,79	0	1	0	0	0	0	0	0	0
-30	5,2	822	1,07	0,23	0,84	0	0	0	1	0,21	0,33	1	0,16	0,19	0,27
0	5,3	2562	1,15	1	0,91	0	0	0	0,21	1	0	0,03	0	0	0,95
30	5,3	1342	1,00	0	0,28	0	0	0	0,33	0	1	0,17	0,99	0,99	0
60	5,2	2703	1,07	0,04	0,78	0	0	0	1	0,03	0,17	1	0,01	0,03	0,04
90	5,4	8853	1,00	0	0,21	0	0	0	0,16	0	0,99	0,01	1	1	0
120	5,2	4291	1,00	0	0,22	0	0	0	0,19	0	0,99	0,03	1	1	0
150	5	3684	1,14	0,95	0,96	0	0	0	0,27	0,95	0	0,04	0	0	1

Table 3.4: Same as Table 3.1, but for the ISC stacked dataset. M_c is the magnitude of completeness computed for each rake-subset.

				SS		NR			SS			TH			
				±180	**-150**	**-120**	**-90**	**-60**	**-30**	**0**	**30**	**60**	**90**	**120**	**150**
λ_c	**M_c**	**N**	**b**	1,15	1,12	1,31	1,56	1,35	1,07	1,15	1,00	1,07	1,00	1,00	1,14
±180	5,5	2063	1.15 ± 0.02	1	0,34	0	0	0	0,01	0,97	0	0	0	0	0,62
-150	5,4	260	1.12 ± 0.07	0,34	1	0	0	0	0,33	0,31	0	0,09	0	0	0,4
-120	5,2	1353	1.31 ± 0.04	0	0	1	0	0,32	0	0	0	0	0	0	0
-90	5,1	2355	1.56 ± 0.03	0	0	0	1	0	0	0	0	0	0	0	0
-60	5,2	1231	1.35 ± 0.04	0	0	0,32	0	1	0	0	0	0	0	0	0
-30	5,2	822	1.07 ± 0.04	0,01	0,33	0	0	0	1	0	0,03	0,89	0	0	0
0	5,3	2562	1.15 ± 0.02	0,97	0,31	0	0	0	0	1	0	0	0	0	0,63
30	5,3	1342	1.00 ± 0.03	0	0	0	0	0	0,03	0	1	0	0,73	0,85	0
60	5,2	2703	1.07 ± 0.02	0	0,09	0	0	0	0,89	0	0	1	0	0	0
90	5,4	8853	1.00 ± 0.01	0	0	0	0	0	0	0	0,73	0	1	0,92	0
120	5,2	4291	1.00 ± 0.02	0	0	0	0	0	0	0	0,85	0	0,92	1	0
150	5.0	3684	1.14 ± 0.02	0,62	0,4	0	0	0	0	0,63	0	0	0	0	1

Table 3.5: Same as Table 3.2, but for the ISC stacked dataset. M_c is the magnitude of completeness computed for each rake-subset.

3.3 Gaussianity of GCMT *b*-values

The randomized-planes histograms of *b*-values are shown in Fig. 3.6. Apart for some "odd"-mechanisms family (λ = ±30°, -60° plane 2, λ= 120° plane 1), for which the normality of the distribution is not guaranteed by the Lilliefors test (*p*-value < 0.05), for all the other distributions the gaussianity hypothesis is confirmed. Higher variances are observed for odd-regimes (especially around normal regimes) and lower for "pure"-regimes. Moreover, the means of the randomized distributions $\bar{b}$ are extremely closer to the estimations of the stacked datasets (Tables 3.1 and 3.2) and the standard errors are surprisingly closer to the one provided by eq. (1.6) (see Table 3.6). The only differences between the estimated errors are found for the "pure" dip-slip faults: normal (λ = -90°) and thrust (λ = 90°) faulting regimes (evidenced with light gray background in Table 3.6). Here, in fact, the standard deviations for the randomized distributions are about halved with respect to the *Shi and Bolt* [1982] estimations for the stacked dataset. This happens because, during the randomization, while for strike-slip mechanisms the two plane solutions fall into separate window-selections (for example the complementary solution of a left fault is a right fault and vice versa), this does not happen for thrust and normal faulting regimes, for which two solutions fall in the same selection, lowering the distribution variances. To clarify, in Table 3.6, moreover, it is also reported the number of repetitions (events counted twice) for the stacking procedure: the only families with values different from zero are λ=±90°. For the stacked bootstrap procedure, the gaussianity tests are passed in all cases (Fig. 3.7) and the results are extremely coherent with the "original" stack analysis.

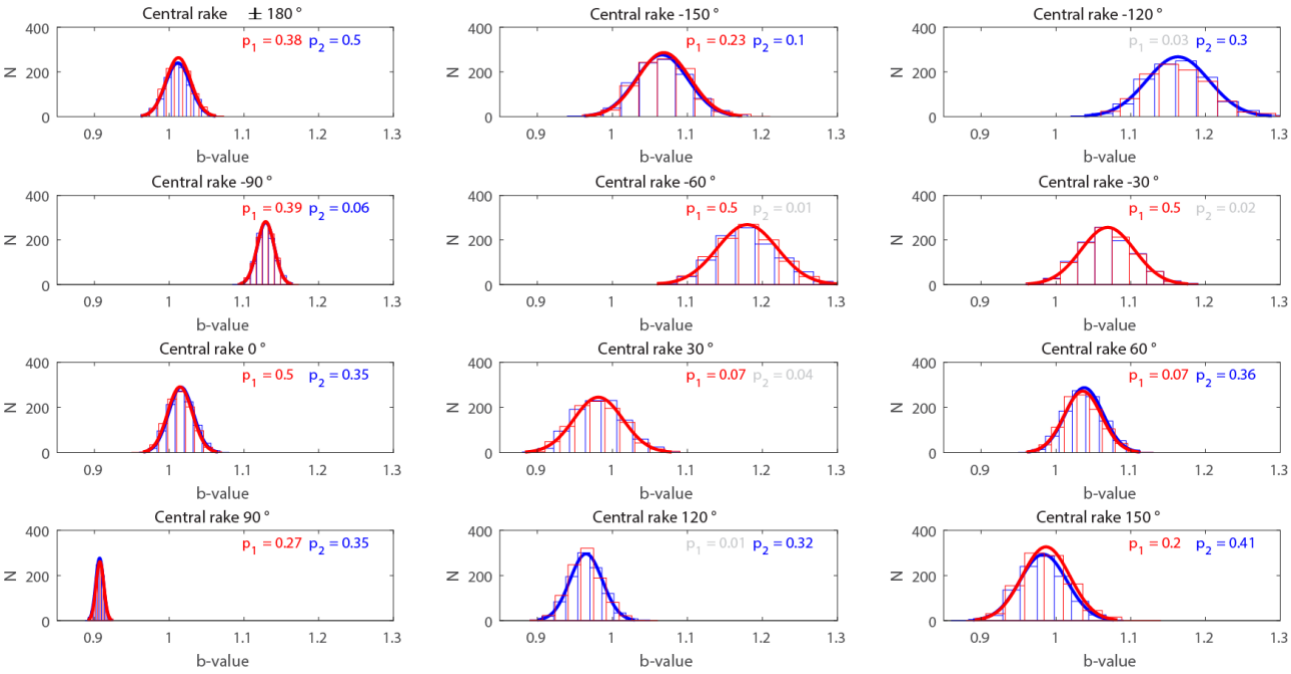

Figure 3.6: Randomized-planes *b*-values distributions relative to different tectonic regimes for the first (red) and second (blue) nodal planes (N=1000 repetitions). For each distribution, a Lilliefors (1967, 1969) gaussian test is performed: if passed, the relative normal curve is overlapped to data and the *p*-value (≤ 5%) is reported with the relative color. If not passed, there is no curve and the *p*-value (> 5%) is displayed in gray.

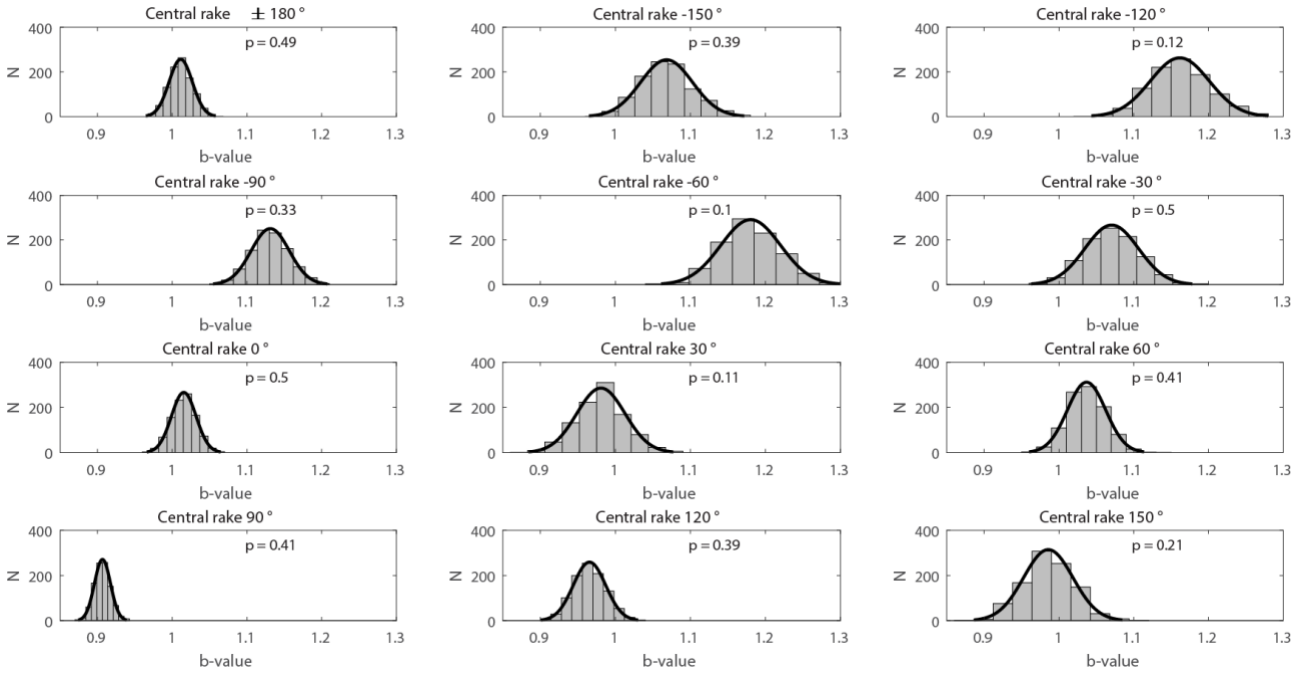

Figure 3.7: Bootstrapped *b*-values histograms relative to different tectonic regimes for the stacked datasets. For each distribution, a Lilliefors (1967, 1969) gaussian test is performed: the relative normal curve is overlapped to data and the *p*-value (≤ 5%) is reported.

λ_c	b_{STACK}	$\sigma_{b_{STACK}}$	N rep	$\bar{b}$ (Pl 1)	$\sigma_{\bar{b}}$ (Pl 1)	$\bar{b}$ (Pl 2)	$\sigma_{\bar{b}}$ (Pl 2)	b_{BOOT}	$\sigma_{b_{BOOT}}$
± 180°	1,012	0,016	0	1,012	0,017	1,012	0,017	1,012	0,016
-150°	1,066	0,034	0	1,069	0,035	1,066	0,035	1,068	0,033
-120°	1,162	0,041	0	1,163	0,042	1,163	0,042	1,163	0,039
-90°	1,129	0,025	755	1,129	0,011	1,129	0,011	1,13	0,026
-60°	1,179	0,04	0	1,18	0,04	1,18	0,04	1,179	0,04
-30°	1,068	0,036	0	1,069	0,036	1,07	0,036	1,07	0,035
0°	1,015	0,016	0	1,014	0,016	1,016	0,017	1,015	0,016
30°	0,981	0,032	0	0,981	0,033	0,982	0,033	0,982	0,033
60°	1,036	0,025	0	1,036	0,025	1,038	0,025	1,037	0,025
90°	0,907	0,01	2690	0,907	0,005	0,907	0,005	0,907	0,01
120°	0,964	0,022	0	0,964	0,022	0,965	0,022	0,964	0,021
150°	0,984	0,032	0	0,987	0,032	0,983	0,031	0,985	0,032

Table 3.6: Randomized and bootstrapped *b*-values with uncertainties compared to stacked *b*-values. Column fields: *b*-value and uncertainties of Table 1, number of repetitions (events counted twice) for the stack, means and standard deviations for the distributions of Fig. 3.6, means and standard deviations for the distribution of Fig. 3.7

3.4 Tapered GR sinusoidal b(λ)

For the sake of completeness, we repeat the analysis by using a different form of GR law, the tapered GR (eq. 1.25) claimed by *Kagan* [1999, 2002a, 2005, 2010], who hardly argued about variations of *b*-values. Final estimates of $b = \frac{3}{2}b^*$ together with "classical" b of Aki equation (1.8) for the stacked datasets are reported in Table. 3.8: they look are quite identical.

We detect, as expected (see *Kagan* [2002a]), different corner magnitudes for different tectonic styles, higher for thrust mechanisms (λ = 90°, 120°) lower for normal mechanisms (λ= -90°, -150°) and intermediate for strike-slip mechanisms. On the contrary, our corner magnitudes significantly differ from the ones of *Kagan* [2002a] (for THR ~ 8.0, for NR ~ 5.8, for SS ~ 6.5-7.2): we are much closer to the maximum magnitudes (see FMD plots of Fig. 3.8), in correspondence of which the loglikelihood for a Pareto-type distribution is maximum [*Pisarenko*, 1991; *Kijiki and Graham*, 1998].

Both GR *b* and tapered GR *b** vary on rake angle λ, with higher values for normal mechanisms and with lower values for thrust mechanisms. Both models perfectly match on a wide range of magnitudes after departing in correspondence of the higher magnitudes: slopes are very similar and the effect of corner magnitude, and consequently of higher magnitudes, on *b*-value is practically negligible. Results of the sinusoidal regression are reported in Table 3.3.

	GCMT					ISC				
λ_c	b^*	σ_{b^*}	b	σ_b	M_{corn}	b^*	σ_{b^*}	b	σ_b	M_{corn}
± 180	1,035	0,019	1,012	0,016	8,4	1,140	0,027	1,148	0,024	8,1
-150	1,073	0,039	1,066	0,034	7,7	1,098	0,074	1,116	0,073	7,3
-120	1,142	0,042	1,162	0,041	8	1,354	0,039	1,314	0,036	7,6
-90	1,103	0,028	1,129	0,025	7,4	1,538	0,035	1,561	0,032	6,9
-60	1,175	0,042	1,179	0,04	8	1,404	0,043	1,35	0,037	7,6
-30	1,058	0,040	1,068	0,036	7,7	1,049	0,04	1,069	0,037	7,2
0	1,039	0,019	1,015	0,016	8,4	1,162	0,021	1,147	0,022	8,1
30	0,969	0,034	0,981	0,032	8,2	1,037	0,026	1,001	0,027	7,8
60	1,043	0,026	1,036	0,025	8,2	1,088	0,022	1,066	0,021	7,9
90	0,921	0,011	0,907	0,01	9	1,011	0,011	0,996	0,011	8,6
120	0,969	0,022	0,964	0,022	8,9	1,012	0,016	0,997	0,015	8,5
150	0,976	0,036	0,984	0,013	7,8	1,117	0,02	1,137	0,018	7,5

Table 3.7: Stacked *b-values for GCMT and ISC datasets using Tapered GR model.** *b*-values of *Aki* [1965] and the estimated corner magnitudes are also reported.

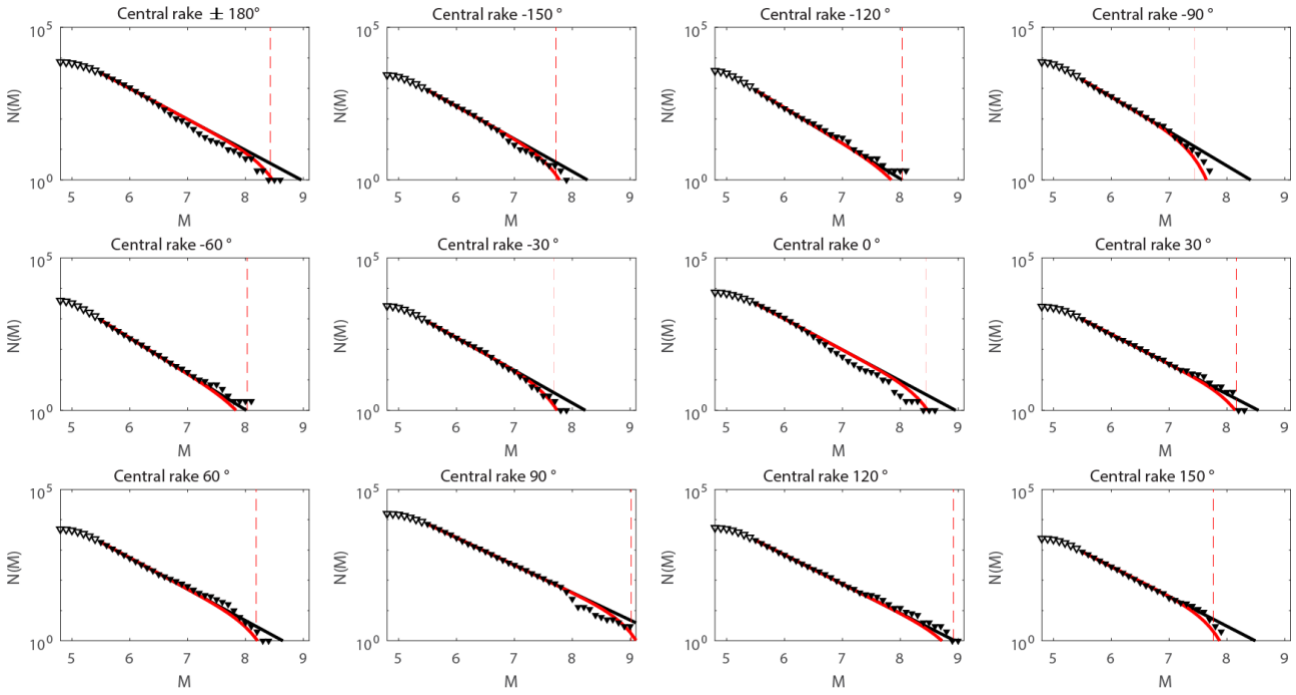

Figure 3.8: GCMT FMD for the stacked datasets. Data below completeness (5.5) are displayed with empty markers, complete data with filled markers. Black line indicates GR law while the red one indicates the tapered GR. Corner magnitudes are indicated with a vertical red dashed line.

4. Conclusions for part 2

We tested, in alternative ways, the hypotheses that the proportion of large earthquakes (low *b*-value) with respect to smaller ones (high *b*-value), depends on the style of faulting through the rake angle λ: for all the considered cases, normal mechanisms ($\lambda \sim -90°$) exhibit higher *b*-values compared to the thrust ones ($\lambda \sim 90°$), while intermediate *b*-values are obtained for strike-slip mechanisms ($\lambda \sim 0°, \pm 180°$).

Computations are performed for 12 independent, rake-disjointed ($\gamma=\pm15°$) subsets of the GCMT catalog, so that a regression law of *b*-value on rake angle λ can be fitted: the fitted harmonic function was found to have a zero phase and a unit frequency thus indicating that *b*-value modulation is about proportional to -sin λ. As the -sin λ corresponds to the scalar product of the slip and gravity versors along the fault plane, *b*-value modulation appears to be proportional to the work done by the gravity force during the earthquake slip.

We obtain consistent results by determining the rake and the *b*-values separately from the GCMT catalog and ISC respectively, using a spatial tessellation of the Earth's surface, applying the moment tensors summation for the global seismotectonic zonation and allowing for a space-dependent magnitude of completeness. Then, the dependence of the *b*-value on tectonic styles would also hold on a spatial scale, since extensive regimes (rake of sum solution $\sim -90°$) match high *b*-value zones while compressive regimes (rake of sum solution $\sim 90°$) match low *b*-value zones, as already shown through the spatial *b*-mapping of part 2.

However, we noted that for both approaches the earthquakes included in different rake windows are unevenly distributed between the two planes and this has consequences on estimated *b*-values. As well, for several windows, the computed *b*-values are significantly different using the two planes. We settled this ambiguity by two methods: the random selection of earthquakes from the two planes and the stacking of the selections from the two original planes, obtaining in all cases similar frequencies and similar oscillating behaviors of *b*-value as a function of rake with maximum at or close to $\lambda \sim -90°$ (normal fault) and minimum at or close to $\lambda \sim 90°$ (reverse fault). Moreover, by randomizing the nodal planes selection or by bootstrapping the stack, we obtain gaussian distributions of the *b*-values, as a proof of the validity of these approaches.

We verified statistical inequalities between all the possible couples of *b*-values relative to different tectonic regimes by using *Utsu* [1966, 1999] and Student tests. The inequality of the *b*-values between all windows centered on different rakes is tested using pure mechanisms "combinations" as well as between several other windows with rakes close to normal and reverse mechanisms.

Definitely, the coherence of such results using different approaches and statistical techniques strongly support the argument that the variability of *b*-value is due to physical reasons and not to technical artifacts as suggested by others.

Part 4

SIMULTANEOUS DEPENDENCE OF GR *B*-VALUE ON TECTONIC STYLES AND DEPTH

A. Petruccelli[1]

P. Gasperini[1], S. Wiemer[2], T. Tormann[2], D. Schorlemmer[3], G. Vannucci[4], A. P. Rinaldi[3]

[1] Dipartimento di Fisica e Astronomia, University of Bologna, Italy; [2] Swiss Seismological Service, ETH Zurich, Switzerland; [3] Helmholtz Centre Potsdam, GFZ Potsdam, Germany; [4] Istituto Nazionale di Geofisica e Vulcanologia, Bologna, Italy

In this last part, we analyze a local high-quality FM dataset of Southern California to statistically model different dependences of b-values (tectonic styles and depth) and then gather them in multivariable dependence models. Differences in earthquakes b are physically related to different states of stress in the crust in a negative linear way. The stress increase with depth linearly in the brittle upper crust: b decreases monotonically with depth until the brittle-ductile transition surface. On the other side, theory of faulting implies that different stress levels accompany different tectonic regimes around the source volume, higher stress for compressive environments and lower stress extensional environments. We therefore develop a brand new, numerical MLE approach for the estimation of b-value which consists in choosing the optimal parameters that maximize the loglikelihood function: the model that best explain the physical reality is the right compromise between the contemporary dependence of b on tectonic styles and depth and a proper complexity level.

1. Introduction

The frequency-magnitude distribution (FMD) of earthquakes obeys to a negative exponential model with increasing magnitude m, the GR law (1.1), with the slope b of such decay (b-value) usually near to the unity. Variations in such slopes determine variations in the proportion of strong/small events within the dataset: if b exceeds 1 the size distributions favor lower magnitude events, while for b lower than 1 result in an increase of higher magnitudes events.

As shown so far, differences in earthquakes b are physically related to different states of stress σ in the crust in a negative way $\Delta b \propto -\sigma$. The assumption of classical *Anderson* [1905] theory of faulting (see part 1 paragraph 2) implies that different stress levels accompany different tectonic regimes around the source volume, higher stress for compressive environments and lower for extensional environments. *Schorlemmer et al.* [2005] firstly evidenced differences in b for different tectonic regimes on rake angle λ of the FMs. We have confirmed and statistically extended its work in parts 2 and 3, also describing this behavior by a harmonic trend $\Delta b \sim -\sin\lambda$: b is minimum for thrust faulting regimes ($b \approx 90°$), b is maximum for normal faulting regimes ($\lambda \approx -90°$), and it is intermediate for strike-slip faults.

On the other side, if the rheological behavior of the brittle crust can be modeled through Coulomb friction and hydrostatic pore pressure [*Byerlee*, 1978], the stress increases with depth linearly in the brittle upper crust [*Brace and Kohlstedt*, 1980; *Kirby*, 1980] (see part 1 paragraph 4). There, in fact, b decreases monotonically with depth until the brittle-ductile transition surface, from which the b starts to increase [*Spada et al*., 2013].

In this final part of the thesis, we want to convert these two separate dependences of b-value (b vs tectonic style, b vs depth) into unique ones b vs tectonic style-depth. We define and analyze several models of different b-value variability (with different degrees of complexity, i.e. number of free parameters n for each model) with a Maximum Likelihood Estimation (MLE) approach, in order to detect the best ones for the description of physical reality: progressive increases in the model complexities (from a constancy of b-value to multiple simultaneous dependence) might ensure a better goodness between observed data and predicted model, although an increase in the number of free parameters could penalize the chosen model with respect to the simpler ones.

2. Data and methods

2.1 Dataset

We use high quality FM from Southern California (SC) dataset [*Yang et al. 2010*; *Hauksson et al., 2012*] from 1981 to end of September 2016 (http://scedc.caltech.edu/research-tools/alt-2011-yang-hauksson-shearer.html, see part 1 paragraph 6.3), displayed in Fig. 4.1.

According to the authors (see Table 4.1), we consider normal mechanisms (NR) the ones with rake angle $-135° \leq \lambda \leq -45°$ (green beach-balls in Fig. 4.1), thrust mechanisms (TH) the ones with rake angle $45° \leq \lambda \leq 135°$ (blue beach-balls), while classifying all the other as strike-slip (SS, red beachballs). The authors provide only the preferred solution (principal plane) for each event: hence, since for strike-slip of SC most of the FM are right-lateral, we compute the alternative plane for each earthquake, and then we perform the stack procedure of the entire dataset in order to have the complete set of possible rakes λ (see part 2 paragraph 4).

Shallower hypocentral depths are a critical information in an earthquake dataset: we decide to discard the shallower earthquakes ($z < 5$ km) and deeper ($z > 15$ km) from our analysis. In fact, as argued by *Spada et al.* [2013], for *b*-depth analysis shallow earthquakes must be treat carefully because such events, especially for SC, can be influenced by geothermal activity (see Fig. 1.11a). The *b*-values of earthquakes induced by high-pressure injections in geothermal reservoirs have been documented to be higher compared to regional levels [*Bachmann et al.*, 2012].

The entire dataset is complete for M above 2.5, according to the authors. Since we need to split our original dataset according to tectonic styles, we use a higher completeness threshold, considering each style-dataset complete over M = 3 (see FMD in Fig. 4.2).

The mechanisms of the catalog can be classified based on their quality. According to *Yang et al.* [2012], the SC FM quality is classified in 4 classes, from A (best) to D (worst), according to the nodal plane uncertainty (in °) and the azimuthal gap (in °) of the preferred solution. We prefer to keep for our analysis the first two classes, A and B, which results in much more reliable information.

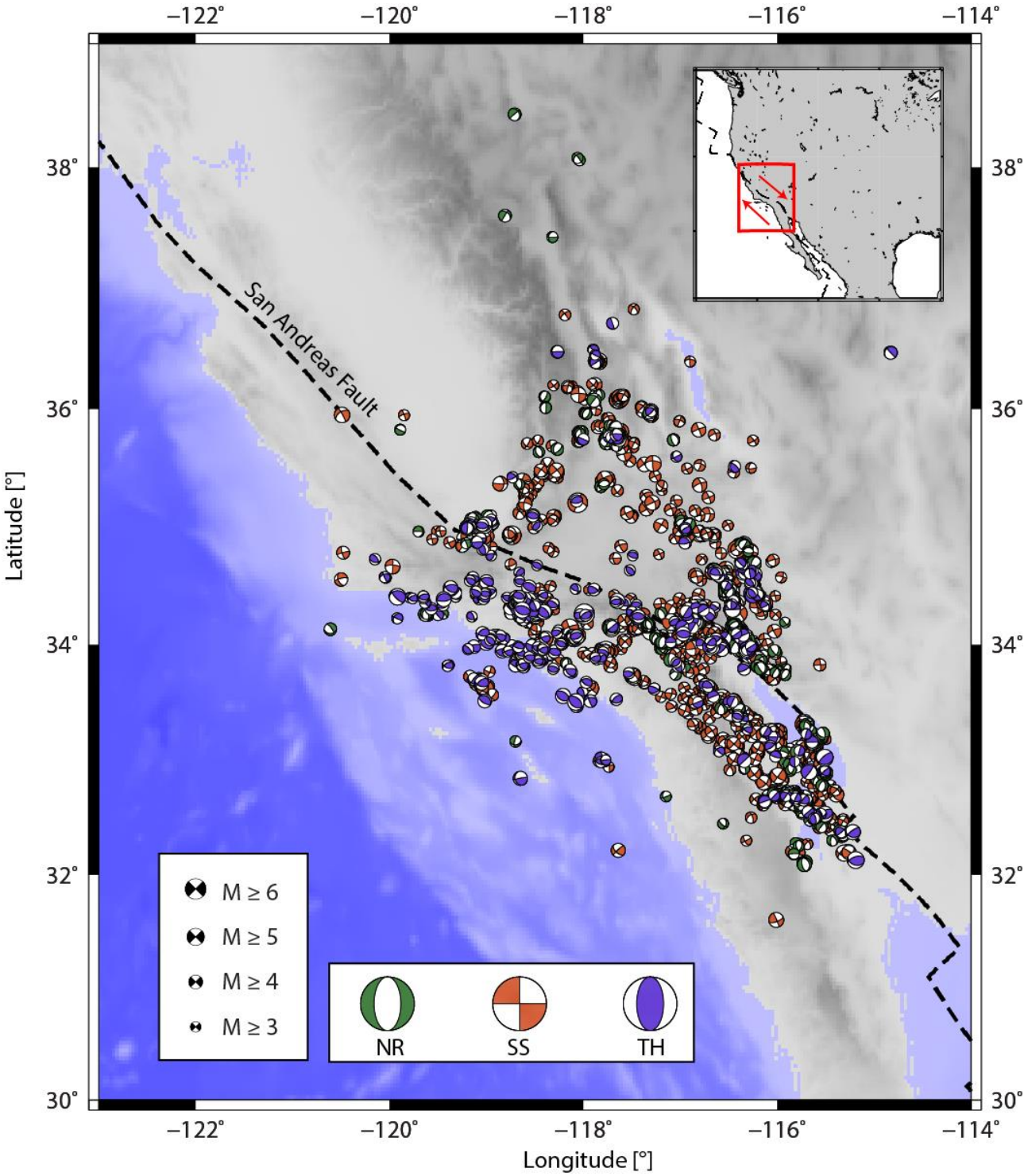

Figure 4.1: SC FM map (1980-2016, 5-15 km, quality AB mechanisms).

	Rake λ	Input	Mc ≥ 3	Final (%)
ALL	$-180° \leq \lambda \leq 180°$	68072	5956	100
NR	$-135° \leq \lambda \leq -45°$	10810	595	9.99
SS	$-180° \leq \lambda < -145°$ $-45° < \lambda < 45°$ $145° < \lambda \leq 180°$	49381	4547	76.34
TH	$45° \leq \lambda \leq 135°$	7881	814	13.67

Table 4.1: SC FM dataset (1980-2016, 5-15 km, quality AB, stack of the nodal planes). First column: rake classification. Second column: total number of input data. Third column: completeness cut. Fourth column: % events considered over the total (second column).

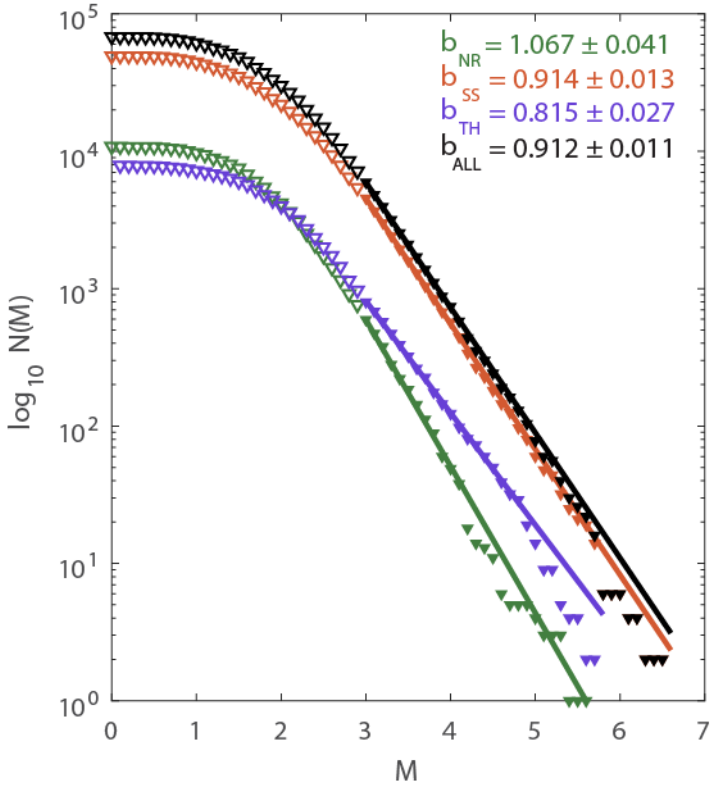

Figure 4.2: FMD for data in Fig. 4.1. The *b*-values are computed with *Aki* [1965] formula (1.8) and the associated errors with *Shi and Bolt* [1982] formula (1.6)**.** Data are complete over M3 (filled markers).

2.2 Methods: different models accompanying b-value variability

In statistical seismology, the MLE method is the standard one for the computation of the GR b. The probability density function (PDF) $f(M)$ for the GR model (1.1) is equation (1.3) for complete datasets. In this part, we have developed a MLE application to numerically estimate b-value, as explained in part 1 paragraph 1.1: the final estimation consists in choosing the optimal b which maximizes the logarithm of the likelihood function $\prod_{i=1}^{N} f(M_i)$, that is the loglikelihood function for the GR model

$$L = \prod_{i=1}^{N} f(M_i) = \sum_{i=1}^{N} \ln\left\{b \ln 10 \ 10^{-b\left[M-\left(M_c-\frac{\Delta M}{2}\right)\right]}\right\} \quad (4.1)$$

The maximization of such function can be performed both analytically (as done so far, see Appendix A) both numerically (as done here).

The numerical maximization (1.7) hence represents a valuable alternative way for the estimation of the MLE b. Equation (4.1) is a general formula with only b as free parameter. An increase in the number of free parameters n results in an increase in the complexity of the model $b(n_1, n_2, \ldots)$used for the explanation of the physical reality. This would mean that in equation (4.1) we can explicit through equations the different dependences of b-value (on depth and tectonic styles separately or simultaneously) and, then, we can maximize the loglikelihood for such models.

Then, we can evaluate the goodness of each model and ranking them according to some statistical criteria. The variance-covariance matrix is computed as $1/H_{ij}$, where H_{ij} is the finite difference Hessian matrix of the minimized sum of squares. The standard errors on the optimal parameters of each model are computed as the square roots of the diagonal elements in the variance-covariance matrix.

2.3 b-value models

It is obvious that in general the larger the number of model parameters the larger the likelihood and the better the fit of the model with data. However, if we are interested in selecting the best from a set of available possible models, we have to account for the number of free parameters for each model by considering an appropriate penalty term to apply to more complex ones with respect to simpler ones. This can be done by the Akaike Information Criterion [AIC, *Akaike*, 1974; *Burnham and Anderson*, 2002] defined as

$$AIC = -2 \log L + 2n \quad (4.2)$$

where n is the number of free parameters in the model and L is the Loglikelihood of each model. According to *Akaike* (1974), the preferred model is the one that minimizes the Kullback - Leibler distance between the model and the data: KL is defined as the amount of information lost when a certain model is used to explain reality. We adopt the second order information criterion of *Akaike* [1974], often called "corrected" *AIC* [*Cavanaugh*, 1997; *Burnham and Anderson*, 2002]

$$AIC_c = AIC + \frac{2n(n+1)}{N-n-1} \tag{4.3}$$

which also takes into account sample size N by increasing a relative penalty term for complex models (high n) with small data sets (low n). *AICc* scores are better shown as

$$\Delta AIC_{c\,i} = AICc_i - \min\{AICc\} \tag{4.4}$$

scores, or difference between each i-th model and the best model (which has the minimum AIC_c, so that the $\Delta AICc_{best} = 0$), for a direct ranking of models.

Another criterion we use to evaluate the goodness of models is the Bayesian Information Criteria (BIC, *Ernst et al.*, 2012), defined as

$$BIC = -2\log L + n\log\left(\frac{N}{\pi}\right) \tag{4.5}$$

Model 0: constant b

The model 0 is the simplest one for eq. (4.1) since it assumes the constancy of b-value of the entire dataset (see previous section) b_{ALL}

$$b_0 = b_{ALL} \tag{4.6}$$

The PDF of this model is simply

$$f_0(b_0|M, M_c, \Delta M) = b_0 \ln 10 \; 10^{-b_0\left[M-\left(M_C-\frac{\Delta M}{2}\right)\right]} \tag{4.7}$$

This model has only one free parameter, b_0.

Model 1: linear relation of b-value on depth/differential stress

In these analyses, we assume the validity of the *Scholz* [2002, 2015] stress state model for the crust: assuming that stress state is governed by frictional strength on preexisting faults ($\mu = 0.75$) and that vertical stress is given by the lithostatic gradient minus the hydrostatic component $(\rho - \rho_W)g$, *Scholz* [2015] calibrated the linear relation of decreasing b with differential stress $\sigma_1 - \sigma_3$ (1.28).

We linearly relate stress state σ (that we approximate with $\sigma_1 - \sigma_3$) with depth, according to *Scholz* [2015] model

$$\sigma \sim \sigma_1 - \sigma_3 = (\rho - \rho_W)gz = \Delta\rho g z \tag{4.8}$$

Earthquakes depth is expressed in km, $g \sim 10^{-2}\frac{km}{s^2}$ and $\Delta\rho = 1.5\;10^{12}\frac{kg}{km^3}$. Then, the proportionality constant between depth and stress is

$$\frac{\sigma}{z} = \Delta\rho g = 15\frac{MPa}{km} \tag{4.9}$$

Equation (4.9) quantify an "average" stress gradient for the upper crust. The model 1 assumes that the b-value depends only on depth z (or on differential stress σ) in a linear way:

$$b(z) = b_0 - \frac{db}{dz}z \tag{4.10}$$

This model has two free parameters, the intercept b_0 and the slope $-\frac{db}{dz}$. The possible switch from depth to differential stress is guaranteed by the supposed linearity between them. Then, the PDF for this model is

$$f_1\left(b_0, \frac{db}{dz} \mid M, z, M_c, \Delta M\right) = \left[b_0 - \frac{db}{dz}z\right] \ln 10 \; 10^{-\left[b_0 - \frac{db}{dz}z\right]\left[M - \left(M_C - \frac{\Delta M}{2}\right)\right]} \tag{4.11}$$

Models 2: b-value dependence on tectonic styles

Model 2.0: constant b-value for different tectonic styles

The model 2.0 assumes the b-value depends only on FMs in a constant way. In this case, we consider separately the three FM families (see Data), normal (NR), strike-slip (SS) and thrust (TH), and we numerically estimate 3 overall b-values:

$$b_{0,STYLE} = \begin{cases} b_{0,NR} \\ b_{0,SS} \\ b_{0,TH} \end{cases} \tag{4.12}$$

Here, the degrees of freedom are three, i.e. the three different intercepts. The 3 PDFs are

$$f_{2.0}(b_{0\,STYLE} \mid M, z, M_c, \Delta M) = \begin{cases} b_{0,NR} \ln 10 \; 10^{-b_{0,NR}\left[M - \left(M_C - \frac{\Delta M}{2}\right)\right]} \\ b_{0,SS} \ln 10 \; 10^{-b_{0,SS}\left[M - \left(M_C - \frac{\Delta M}{2}\right)\right]} \\ b_{0,TH} \ln 10 \; 10^{-b_{0,TH}\left[M - \left(M_C - \frac{\Delta M}{2}\right)\right]} \end{cases} \tag{4.13}$$

The final loglikelihood score for this model will be the sum on the three different FM families ($L_{2.0} = L_{NORM} + L_{SS} + L_{THR}$ with number of events $N = N_{NORM} + N_{SS} + N_{THR}$).

Models 2.1 and 2.2: sinusoidal b-value on rake angle

Rake angle λ is a useful parameter for the determination of the tectonic style of an earthquake on the basis of FM: NR faults have λ close to -90° (extensional environments), TH faults have λ close to 90° (compressive environments) and SS faults λ close to 0, ±180° (transcurrent environments). As we have widely showed, variations Δb on such angle are significant: NR faults exhibit positive variations of b-value (maximum at about $\lambda \sim$ -90°), TH faults exhibit negative variations of b-value (minimum at about $\lambda \sim$ 90°), SS faults instead do not suffer variations, lying on the overall b-value (mostly 1). In previous part, we have proposed a harmonic functional form of this behavior described by (3.2) in its simplest form (unit frequency and null phase, i.e. only two free parameters

to estimate that are the offset b_0 and the amplitude of variations α). Further, it can be generalized (3.5), by accounting for frequencies ω different from the unity and for possible phase terms φ, resulting in two more free parameters. The resulting PDFs for such models are

$$f_{2.1}(b_0, \alpha | M, \lambda, M_c, \Delta M,) = [b_0 - \alpha \sin(\lambda)] \ln 10 \ \ 10^{-[b_0 - \alpha \sin(\lambda)]\left[M - \left(M_C - \frac{\Delta M}{2}\right)\right]} \tag{4.14}$$

$$f_{2.2}(b_0, \alpha, \omega, \varphi | M, \lambda, M_c, \Delta M) = [b_0 - \alpha \sin(\omega\lambda + \varphi)] \ln 10 \ \ 10^{-[b_0 - \alpha \sin(\omega\lambda + \varphi)]\left[M - \left(M_C - \frac{\Delta M}{2}\right)\right]} \tag{4.15}$$

Models 3: simultaneous dependence of b-value on tectonic styles and depth (stress)

Model 3.0: different gradients of depth for different families of tectonic style

The model 3.0, which has the maximum degree of complexity, assumes the contemporary dependence of b-value on FM, and depth (differential stress) in a different way: we get three different linear relations of decreasing b with depth for the three different tectonic regimes.

$$b(z) = \begin{cases} b(z)_{NR} = b_{0,NR} - \left(\frac{db}{dz}\right)_{NR} z \\ b(z)_{SS} = b_{0,SS} - \left(\frac{db}{dz}\right)_{SS} z \\ b(z)_{TH} = b_{0,TH} - \left(\frac{db}{dz}\right)_{TH} z \end{cases} \tag{4.16}$$

For each style-model, we have two free parameters, the intercept $b_{0,STYLE}$ and the slope $\left(\frac{db}{dz}\right)_{STYLE}$, for a total of 6 free parameters.

The 3 PDFs are

$$f_{3.0}\left(b_{0\,STYLE}, \frac{db}{dz}_{STYLE} \,\middle|\, M, z, M_c, \Delta M\right) = \begin{cases} \left[b_{0,NR} - \left(\frac{db}{dz}\right)_{NR} z\right] \ln 10 \ \ 10^{-\left[b_{0,NR} - \left(\frac{db}{dz}\right)_{NR} z\right]\left[M - \left(M_C - \frac{\Delta M}{2}\right)\right]} \\ \left[b_{0,SS} - \left(\frac{db}{dz}\right)_{SS} z\right] \ln 10 \ \ 10^{-\left[b_{0,SS} - \left(\frac{db}{dz}\right)_{SS} z\right]\left[M - \left(M_C - \frac{\Delta M}{2}\right)\right]} \\ \left[b_{0,TH} - \left(\frac{db}{dz}\right)_{TH} z\right] \ln 10 \ \ 10^{-\left[b_{0,TH} - \left(\frac{db}{dz}\right)_{TH} z\right]\left[M - \left(M_C - \frac{\Delta M}{2}\right)\right]} \end{cases} \tag{4.17}$$

As done for model 2.0, the Loglikelihood score are finally summed.

Model 3.1: simultaneous fluctuation on λ and linear decay on depth of b-value

The dependence of b-value on tectonic styles expressed with the sinusoid of rake angle (3.2) can be combined with a linear decay on hypocentral depth (4.6)

$$b(\lambda, z) = b_0 - \left(\frac{db}{dz}\right) z - \alpha \sin \lambda \tag{4.18}$$

This model has 3 free parameters: a common offset b_0 for both dependence, an overall depth gradient of b-value and the amplitude variation α. It is easy to note that, in absence of depth dependence ($z = 0$), eq. (4.18) reduces to eq. (3.2) and, in absence of rake dependence ($\alpha = 0$), it turns into eq. (4.10).

The PDF is

$$f_{3.1}\left(b_0, \frac{db}{dz}, \alpha, \omega, \varphi \middle| M, \lambda, z, M_c, \Delta M\right) = \left[b_0 - \left(\frac{db}{dz}\right) z - \alpha \sin\lambda\right] \ln 10 \; 10^{-\left[b_0 - \left(\frac{db}{dz}\right) z - \alpha \sin\lambda\right]\left[M - \left(M_C - \frac{\Delta M}{2}\right)\right]} \tag{4.19}$$

Model 3.2: b-value on depth with gradient modulated by sin λ

The last model we propose is a reformulation and simplification of models 3.0 and 3.1. The three depth-gradients of 4.16 can be expressed as a function of friction μ (see Appendix C for analytical details), by inserting the expressions for the differential stresses for the three styles in (1.28)

$$\begin{cases} \frac{db}{dz}_{NR} = -k \frac{2\mu\rho g}{\sqrt{\mu^2+1}+\mu} \\ \frac{db}{dz}_{TH} = -k \frac{2\mu\rho g}{\sqrt{\mu^2+1}-\mu} \\ \frac{db}{dz}_{SS} = -k \frac{2\mu\rho g}{\sqrt{\mu^2+1}} \end{cases} \tag{4.20}$$

where k comes from equation (1.25). It is easy to see from (4.20) that the depth gradient is much more pronounced for TH with respect to NR, and SS between them (see part 1 paragraph 2.1). As stated in the previous part, the harmonic fluctuation $-\sin\lambda$ of b-values has a physical origin: as proposed by *Anderson* (1905) and *Turcotte and Schubert* (2002), gravity favors slip on normal faults with respect to thrust faults. Then, the differential stress required to activate a normal fault ($\sin\lambda < 0$) should be lower than the one required for a thrust fault ($\sin\lambda > 0$), with a strike-slip fault ($\sin\lambda \cong 0$) lying in the middle. If the differential stress is modeled as (3.1), the $-\sin\lambda$ term would correspond to the scalar product between the along-dip component of slip vector ($\sim \sin\lambda$) and the gravity force (unit vector), which is minimum for normal faults (extensions easy to activate) and maximum for thrust faults (compressions hard to activate), and nihil for strike-slip (for which $\sin\lambda \sim 0$). Then, possible effects of differential stress on strike-slip faults should be negligible, and consequently on b-values modeling (see further in the text).

We then propose an "heuristic" formula of depth-dependent b with depth-gradients modulated by the sin λ

$$b(\lambda, z) = b_0 - \kappa \frac{2\mu\rho g}{\sqrt{\mu^2+1}-\mu\sin\lambda} z \tag{4.21}$$

This time the gradient κ has dimensions of MPa^{-1}. The model has only 3 free parameters: it accounts for possible different friction μ and "overall" gradient κ values (apart from the offset b_0). For simplicity, we assume a "pure" sinusoid ($\omega = 1$ and $\varphi = 0$) at the denominator of (4.21). The PDF is

$$f_{3.3}(b_0, \kappa, \mu | M, \lambda, z, M_c, \Delta M) = \left[b_0 - \kappa \frac{2\mu\rho g}{\sqrt{\mu^2+1}-\mu\sin\lambda} z\right] \ln 10 \; 10^{-\left[b_0 - \kappa \frac{2\mu\rho g}{\sqrt{\mu^2+1}-\mu\sin\lambda} z\right]\left[M - \left(M_C - \frac{\Delta M}{2}\right)\right]} \tag{4.22}$$

3. Results

3.1 Spatial, frequency-magnitude and depth distributions of FMs in Southern California

The tectonics of SC is dominated (76%) by SS mechanisms (red mechanisms, Fig. 4.1), although also portions of NR (14%, green mechanisms in Fig. 4.1) and TH mechanisms (10%, blue mechanisms in Fig. 4.1) are present and allow for statistical analyses (Table 4.1). NR mechanisms share almost the same zones of the SS ones, while the TH mechanisms mostly fill the western areas of SC. In fact, as reported by *Hauksson* [1990, 2011], the western part of SC (eastern bay of Los Angeles) behaves differently with respect to the rest of the area: there is a transition zone from right-lateral SS to oblique TH, as going towards north-west. In this zone, relative strong earthquakes occurred in the past (as the 1 October 1987 Whittier Narrows ML 5.9 or the 29 July 2008 Chino Hills Mw 5.4 earthquakes), showing reverse fault mechanisms.

Each of style-datasets concur for a different FMD (Fig. 4.2). The *b*-value is around 0.9 for all tectonic styles (ALL, black markers) while, as expected, NR FMD (red markers) has a higher *b*-value (about 1.1) and the TH (blue markers) FMD a lower one (around 0.8) while, strike-slip FMD, almost match the overall FMD. These values are fairly consistent with the estimations provided by the authors (2012 update, with all quality FMs in): 0.994 ± 0.007 for ALL, 0.983 ± 0.008 for SS faulting, 0.900 ± 0.018 for TH faulting, and 1.165 ± 0:021 for NR faulting. The linearity of GR law is then guaranteed for all styles on a wide range of magnitudes: it reaches ~ M6 for SS, ~ M5 for TH and ~ M4 for NR mechanisms.

In order to evaluate the behavior of earthquakes occurrences with depth, the probability density functions (PDFs) are reported (Fig. 4.3). Generally speaking, all the style-trends exhibit an increase and then a decrease, meaning that earthquake occurrence tends to vanish going deep in the crust. For SC, the so-called seismogenic layer (or nucleation zone) is about 15 km, although regional variations from 5 to 25 km are reported [*Nazareth and Haukkson*, 2004]. Underneath it, only a small percentage of crustal earthquakes occur, probably because of the brittle-ductile transition in the crust.

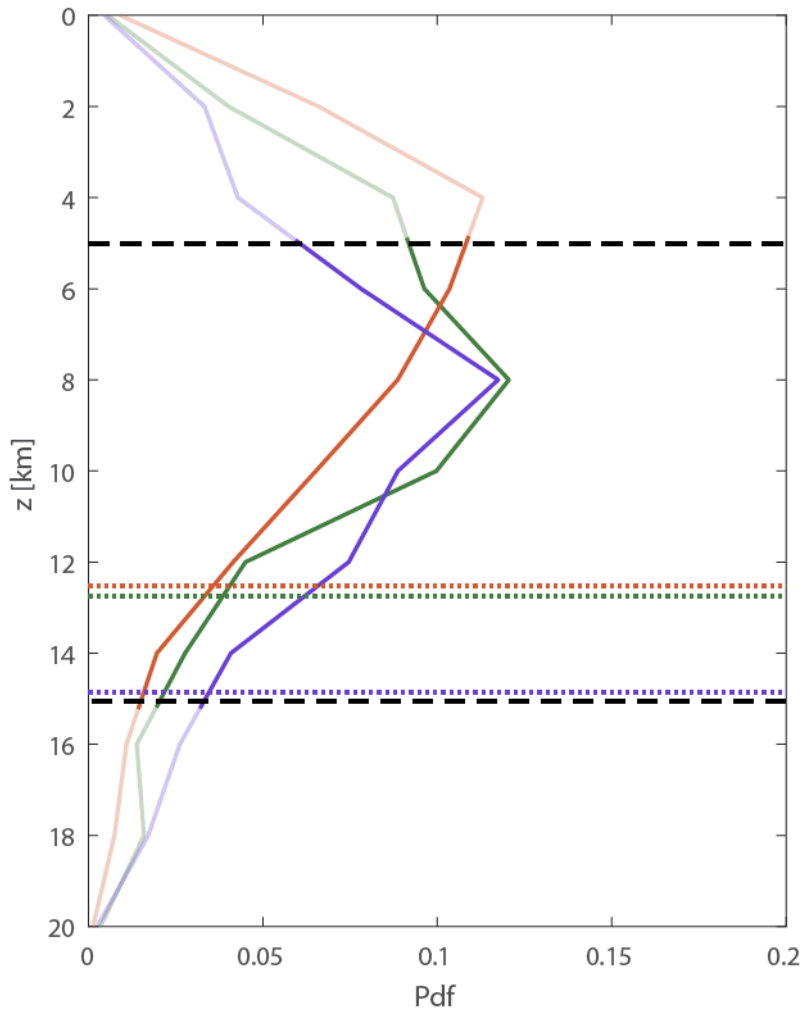

Fig. 4.3: NR (green), SS (red) and TH (blue) PDFs as a function of hypocentral depth z (mechanisms A, B). The depth-PDF estimates are computed with the normalization $z_i' = \frac{z_i}{N\,dz}$, where z_i is depth bin value, N is the dataset size and dz the width of the bin (1 km). Dotted horizontal lines denote the seismogenic depths for each style, i.e. 90% of the data. Black dashed horizontal lines denote the chosen depth limits.

There, as evidenced by many authors, the stress-strain relationship is no more linear (as assumed for the shallow crust) but non-linear, of the type of equation (1.27), describing a plastic flow. Though the seismogenic depth thickness could depend on other physical properties (lithology, stress, strain, material, etc), temperature T is an important factor controlling the maximum depth of seismicity [*Brace and Byerlee*, 1966]. An increase in T (deep crust) increase non-linearity while a decrease in T ensure linearity of the strain-stress relation. *Bonner et al.* (2003) evidenced that, for California, seismogenic depth thickness is inversely correlated with the heat flow: deeper earthquakes occur when heat flow is lower while shallower earthquakes are favored by higher flows. In Fig. 4.3 SS and NR exhibit a sudden increase in the first 4 km layer. This is possibly due to intense geothermal activities, located in the very shallow crust. While SS PDFs start decreasing after 4 km, TH and NR mechanisms, the last of which are unlikely to be found in the shallow crust, progressively increase reaching the maximum frequency at 8 km. From there, the decrease starts with higher NR frequencies with respect to TH. Around 11 km there is an inversion of the TH-NR depth-trends, with higher TH frequencies with respect to NR. This could mean that stress conditions in the deeper crust favor compressions. Moreover, thrust regions in Fig. 4.3 are mostly associated with low heat flow, as reported by *Haukssson* [2011]. The PDF trends are

consistent with what already observed for tectonic style-PDFs with depth for SC by *Yang and Hauksson* [2011] and by *Yang et al.* [2012]. Seismogenic depth might be quantified with the maximum depth containing a certain percentage of seismicity: we choose a 90% level, as done by *Hauksson* [2011], in delimiting the seismogenic depth layer. Consequently, SS and NR mechanisms would have lower seismogenic depth layer (12-13 km) in respect to TH mechanisms (15 km).

3.2 Models analysis

The statistical analyses for all the models are summarized in Table 2 and the plots of the respective equations are displayed in Figs. 4.4 and 4.5.

Single variable models

Model 0 estimates only one parameter, through numerical maximization of the Log-Likelihood function (4.1). As expected, the numerically estimated value coincides with the analytical one obtained by Aki's formula (1.5) of Fig. 4.2, with similar errors, proving that the two approaches are interchangeable one to the others. This model has obviously the lowest Loglikelihood but even the highest AIC_c and *BIC* (Table 4.2), so it is the worst among the others.

Model 1 (*b*-value decreasing with depth, same dependence for all styles, black line in Fig. 4.4) has two free parameters to estimate, the intercept and the slope with respect to depth (eq. 4.10). Compared to model 0, the Loglikelihood increases and AIC_c and *BIC* decrease, so Model 1 improves the description of nature. The obtain depth-slope is similar to the one provided by (1.28), which is $\frac{db}{dz}_{SCHOLZ} = 0.018 \pm 0.004$ (if eq. 4.9 is assumed).

Models 2 assume that *b*-value depends on faulting styles but not on depth. According to model 2.0, *b*-value depends only on tectonic styles in a constant way: it has three free parameters to estimate, the *b*-values for the three styles. The AIC_c and *BIC* are lower than both Models 0 and 1 indicating that the separation on different tectonic styles has a higher impact on the accuracy of the fit with respect to depth dependence. Models 2.1 and 2.2 (black and grey harmonic curves in Fig. 4.5), instead, describe *b*-value variations on tectonic styles by taking advantage of the rake angle λ classification: model 2.1 (eq. 3.2) estimates only two parameters (off-set and amplitude of the variation) while model 2.2 (eq. 3.5) increases the complexity by assuming also the existence of a "frequency" ω of the sinusoid different from 1 and of a phase factor φ (for a total of 4 parameters). However, in this case, the results cannot do better than model 2.0, since AIC_c and *BIC* for models 2.1 and 2.2 are higher than the ones of 2.0 and *L* scores are lower.

b	Model equation		Estimated parameters	$L(\hat{b})$	AIC_c	BIC
Const.	0	$b = b_0$	$b_0 = 0.912 \pm 0.012$	-1539.7	3081.4	3086.3
Depth	1	$b(z) = b_0 - \frac{db}{dz} z$	$b_0 = 1.067 \pm 0.012$; $\frac{db}{dz} = 0.017 \pm 0.001$ km^{-1}	-1532.9	3069.8	3079.5
Fault. style	2.0	$b_{STYLE} = b_{0,STYLE}$	$b_{NR} = 1.067 \pm 0.043$; $b_{SS} = 0.914 \pm 0.013$; $b_{TH} = 0.815 \pm 0.028$	-1527.4	3060.7	3075.3
	2.1	$b(\lambda) = b_0 - \alpha \sin\lambda$	$b_0 = 0.914 \pm 0.012$; $\omega = 0.091 \pm 0.022$	-1531.4	3066.9	3076.6
	2.2	$b(\lambda) = b_0 - \alpha \sin(\omega\lambda + \varphi)$	$b_0 = 0.915 \pm 0.012$; $\Delta b = 0.094 \pm 0.022$; $\omega = 1.038 \pm 0.070$; $\varphi = 0 \pm 8.53$	-1531.3	3070.6	3090.1
Fault. style and depth	3.0	$b_{STYLE}(z) = b_{0,STYLE} - \left(\frac{db}{dz}\right)_{STYLE} z$	$b_{0,NR} = 1.101 \pm 0.043$ $\frac{db}{dz}_{0,NR} = 0.004 \pm 0.005$ km^{-1} $b_{SS} = 1.046 \pm 0.013$ $\frac{db}{dz}_{0,SS} = 0.015 \pm 0.001$ km^{-1} $b_{0,TH} = 1.023 \pm 0.028$ $\frac{db}{dz}_{0,TH} = 0.021 \pm 0.003$ km^{-1}	-1521.8	3055.6	3084.7
	3.1	$b(\lambda, z) = b_0 - \left(\frac{db}{dz}\right) z - \alpha \sin\lambda$	$b_0 = 1.046 \pm 0.012$; $\frac{db}{dz} = 0.014 \pm 0.001$ km^{-1} ; $\alpha = 0.080 \pm 0.022$	-1526.6	3059.2	3073.8
	3.2	$b(\lambda, z) = b_0 - \kappa \frac{2\mu\rho g}{\sqrt{\mu^2 + 1} - \mu \sin\lambda} z$	$b_0 = 1.046 \pm 0.012$ $\kappa = (85.8 \pm 6.3)10^{-5}$ MPa^{-1} $\mu = 0.524 \pm 0.036$	-1525.4	3056.9	3071.4

Table 4.2: Summary of statistical analyses on the *b*-value models. Gold, silver and bronze background evidence models ranking (1st ,2nd, 3rd).

Multi-variable models

Models 3 accounts for the simultaneous dependences of *b*-value with depth and tectonic styles with the best fits: Loglikelihood functions have the highest scores and the relative AIC_c and *BIC* the lowest, among the possible models (Table 4.2).

For model 3.0, each tectonic style can be described through a different equation of decreasing *b* as a function of depth (differential stress), for a total of six free parameters (eq. 4.16, Fig. 4.4). This model results in the highest *L*-value and the lower (and hence best) *AICc*. Steeper depth gradient is found for TH, intermediate depth gradient for SS and lower depth gradient for NR. According to our equations, *b*-value should suffer a decrease of about 0.04 unit every 10 km for NR, of about 0.15 unit every 10 km for SS, of about 0.2 unit every 10 km for TH. These statements agree with what expected: if linearity between stress and depth is assumed [*Bylerlee*, 1966; *Brace and Kohlstedt*, 1980; *Kirby*, 1980] in the brittle shallower crust, differences in tectonic styles accompany differences in stress levels around the source

volume [*Anderson*, 1905], and consequently in *b*-values. *b*-values are expected to be lower for thrust because under compression conditions higher differential stress is requested for rock fracturing [*Amitrano*, 2003]. Higher stressed portions of the crust locate in the deep crust, where TH-PDFs have higher values (Fig. 4.3, blue line) and where *b*-values are expected to be lower (Fig. 4.4). Vice versa, lower stressed portions of the crust locate in the upper crust, where thrust-PDFs are low (Fig. 4.3), SS and NR mechanisms have higher occurrences and *b*-values are expected to be higher (Fig. 4.4).

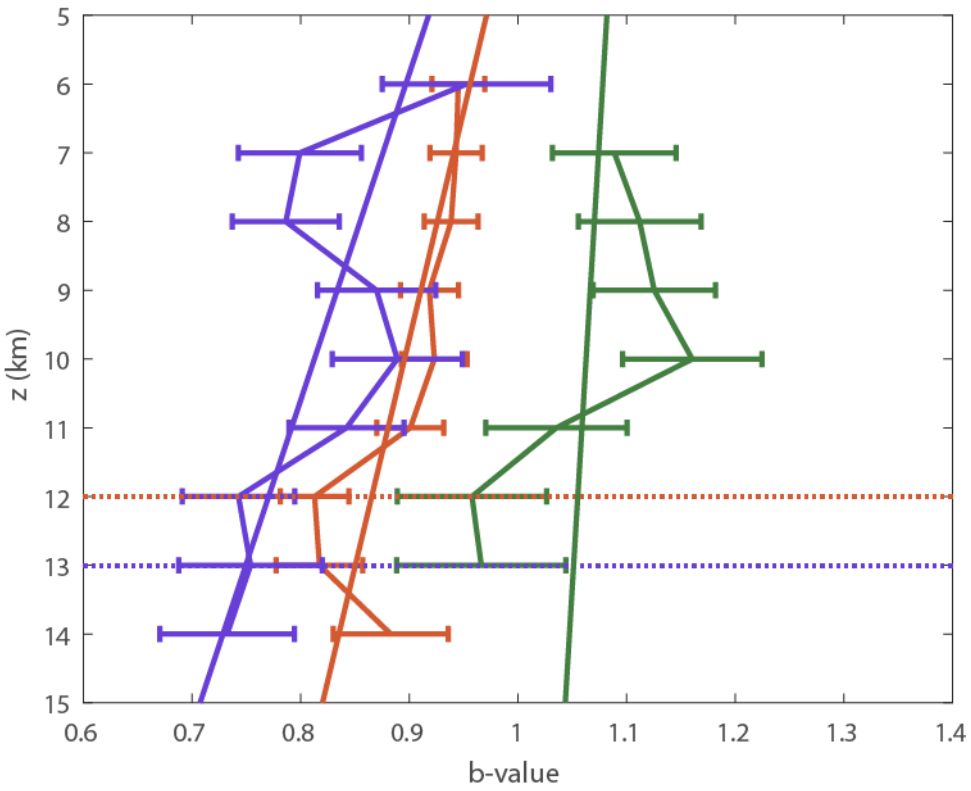

Figure 4.4: Analytical *b*-values with depth for different tectonic regimes. Models 3.0 are fitted on data. Dotted horizontal lines indicate the brittle-ductile transition for the three tectonic styles. Error-bars indicate *Shi and Bolt* [1982] uncertainty.

We also re-adopt the procedure of moving windows with depth proposed by *Spada et al.* [2013], overlapping model 3.0 equations (Fig. 4.4) on the *b*-values computed with *Aki* [1965]'s formula (eq. 1.5). In the original work, for *Hauksson et al.* (2012) 1981-2011 magnitude dataset, *Spada et al.* (2013) used depth layers of 2.5 km. We enlarge these selections to 4 km for NR and reduce to 2 km for SS and TH, with a moving step of 1 km and with a minimum number of 50 events per selection.

The increase of *b*-value in correspondence of the brittle-ductile transition (dotted horizontal lines) can be explained, according to *Spada el al.* [2013], with a change in the rheological properties of the crust. In fact, according to the generic strength profile of the crust proposed by *Scholz* [2002], the non-linear decrease of shear-stress after the brittle-ductile transition would result in increasing *b*-values. However, the inversion in *b*-value with depth is only well detectable for SS regime, and partially for NR one. The absence of such behavior for TH regime might indicate that the linearity of *b* with stress would hold on a wider depth range for TH, i.e. a deeper brittle-ductile transition. However, there must be considered that at such depths the earthquakes occurrences are very limited (see Fig 4.3).

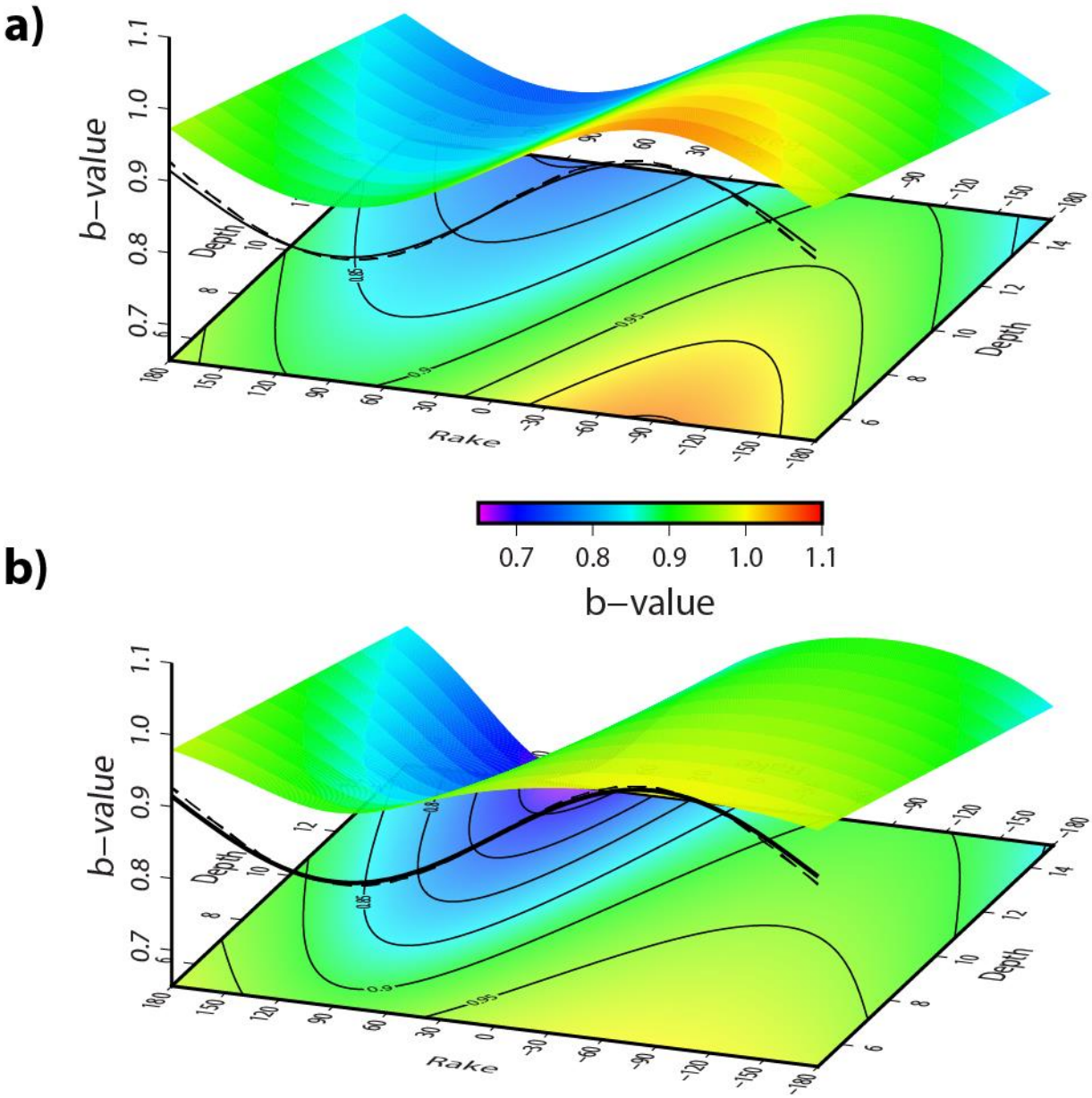

Figure. 4.5: *b* (λ, z) surfaces for models 3.1 and 3.2. With solid and dashed black lines respectively models 2.1 and 2.2 are also reported (at z=5 km).

Models 3.1 and 3.2 provide an overall and complete view of the simultaneous dependences of *b*-value on tectonic styles (e.g. rake angle λ) and depth, since they can be plotted in a 3D view (Fig. 4.5). Both of them, exhibit the harmonic fluctuation of *b* on rake angle λ and a decay of *b* with depth: *b*-value is then expected to be higher in the shallow crust (with maximum values on normal faults, $\lambda \sim -90°$) and to be lower in the deep crust (with minimum values on thrust faults, $\lambda \sim 90°$). Again, strike-slip faults ($\lambda \sim 0°, \pm 180°$) suffer intermediate variations with depth.

Model 3.1 (eq. 4.18, Fig 4.5 a) has a single depth gradient, a unique offset (identical to the one for SS of model 3.1), a single depth-gradient (consistent with the one for SS of model 3.1 and quite close to the one of model 1) and maximum amplitude (consistent with the one of the sinusoids 2.1 and 2.2).

It preserves the sinusoidal folded shape with depth: normal *b*-values ($\lambda \sim -90°$) decay from ~ 1.1 (NR upper crust) to ~ 0.9 (NR lower crust), thrust *b*-values ($\lambda \sim 90°$) from ~ 0.9 (TH upper crust) to ~ 0.7 (TH lower crust), and strike-slip from ~ 0.95/1 (upper crust) to ~ 0.85/0.8 (lower crust).

Although this model seems to be quite exhaustive, a further forward step can be made by the model 3.2 (eq. 4.21), which does not have the highest Loglikelihood but instead has the lowest *BIC*. Model 3.2, which assumes a different gradient modulation of *b*-value with depth, modeled through the $\sin \lambda$ factor in eq. (4.21), is fully consistent with models 3.0 and 3.1 (Table 4.2). In this case, maximum *b*-values (~ 1) are found in the NR upper crust ($\lambda \sim -90°$) and minimum *b*-values (~ 0.65-0.7) are found in the TH upper crust ($\lambda \sim 90°$). Intermediate *b*-values (~ 0.9) describe "harmonic" patterns in the rake-depth plane by filling the upper TH crust, the lower NR crust and the SS regimes. Note how strong is the effect of the different gradient of TH with respect to NR, resulting in a deformation of the sinusoidal surface and in a steep drop of *b*-values.

A final consideration regards the estimated friction value $\hat{\mu}$ of Model 3.2: it is lower (~ 0.5) than the usual values (0.6-1.0). In fact, differently from other major tectonic faults, SAF would represent an exception with lower values in frictional strength (~ 0.3 - 0.5). According to *Zoback et al.* [1987] and *Carpenter et al.* [2011], the fault is weaker because of a general low stress field on the fault and a lack of healing of the fault-zone material respectively. This could explain why the San Andreas Fault slips by aseismic creep and small earthquakes, rather than by large, destructive earthquakes. On the other side, fault weakening could be caused also by anomalous heat flows (thermally induced increase of fluid pressure, dehydration, etc.) [*Brune et al.*, 1969; *Lachenbruch and Sass*, 1980].

Stress gradients analysis

Scholz [2002, 2015] previously argues about three different stress gradients for different tectonic styles, ranked as $\frac{d\sigma}{dz}_{NR} < \frac{d\sigma}{dz}_{SS} < \frac{d\sigma}{dz}_{TH}$ (see Table 4.3). Such values are obtained by assuming a friction coefficient of 0.75, a rock density of 2500 $\frac{kg}{m^3}$, and vertical stress equal to lithostatic gradient minus a hydrostatic pore pressure. Stress measurements in deep boreholes for the continental crust indicate that friction values should range from 0.6 - 1.0 [*M. D. Zoback and Townend*, 2001; *M. L. Zoback and Zoback*, 2007]. As evidence before, *b*-depth and *b*-stress gradients from Model 1 are in good agreement with *Scholz* [2017], since they are sustained by the same hypotheses. The switch from one gradient to the other one is guaranteed by equation (4.9), in infinitesimal form

$$d\sigma = Cdz \tag{4.23}$$

where C is the assumed "overall" stress gradient for the crust ($15 \frac{MPa}{km}$). On the other side, equation (1.28) is differentiated as

$$db = kd\sigma \tag{4.24}$$

where k is *Scholz* [2015] estimated stress gradient of *b* ($0.0012 \pm 0.0003\ MPa^{-1}$). If we would use (4.24) to convert Model 3.0 *b*-depth gradients into stress-depth gradients,

$$\frac{d\sigma}{dz}_{3.0} = \frac{1}{k}\frac{db}{dz}_{3.0} \tag{4.25}$$

we would obtain values that are lower than the ones expected by theory (see Table 4.3). In fact, all the statistical analyses done so far point towards a different depth (i.e. stress) - behavior of the three tectonic styles, that is not expressed by (4.24).

Model 3.2, instead, provide a more reliable information for this gradients analysis. Among the final estimated parameters, we have an "overall" stress-gradient of *b*-value κ. This value is relatively close to previous estimations (it can be converted into a depth-gradient of *b*-value using 4.23). If we derive equation (4.17) with respect to depth, we get (in absolute value) an expression for the depth-gradient of *b*-values relative to different tectonic styles (for NR sin λ = -1, for SS sin λ = 0, for TH sin λ = 1)

$$\frac{db}{dz}_{3.2} = 2\rho g \frac{\kappa\mu}{\sqrt{\mu^2+1}-\mu\sin\lambda} \tag{4.26}$$

by substituting in 4.26 the final estimated parameters $\hat{\mu}$ and $\hat{\kappa}$ (see Table 4.2). The passage from *b*-depth gradients to stress-depth gradients is then

$$\frac{d\sigma}{dz}_{3.2} = \frac{1}{\hat{\kappa}}\frac{db}{dz}_{3.2} \tag{4.27}$$

For model 3.2, stress gradients are much closer to the theoretically expected values (see Table 4.3).

	Gradients	MODELS			
		Scholz [2015]	b(z)	b(z,FM)	b(λ,z)
ALL	$\frac{db}{dz}\ \left[\frac{1}{km}\right]$	0.018 ± 0.004	0.017 ± 0.001		0.0129 ± 0.0003
	$\frac{db}{d\sigma}\ \left[\frac{1}{MPa}\right]$	0.0012 ± 0.0003	0.00115 ± 0.00006		$(85.8 \pm 6.3)10^{-5}$
	$\frac{d\sigma}{dz}\ \left[\frac{MPa}{km}\right]$	15	15		15
NR	$\frac{db}{dz}\ \left[\frac{1}{km}\right]$			0.004 ± 0.004	0.0092 ± 0.0009
	$\frac{db}{d\sigma}\ \left[\frac{1}{MPa}\right]$			0.0012 ± 0.0003	$(85.8 \pm 6.3)10^{-5}$
	$\frac{d\sigma}{dz}\ \left[\frac{MPa}{km}\right]$	11.25		3.33 ± 4.16	10.7 ± 1.8
SS	$\frac{db}{dz}\ \left[\frac{1}{km}\right]$			0.015 ± 0.001	0.0135 ± 0.0015
	$\frac{db}{d\sigma}\ \left[\frac{1}{MPa}\right]$			0.0012 ± 0.0003	$(85.8 \pm 6.3)10^{-5}$
	$\frac{d\sigma}{dz}\ \left[\frac{MPa}{km}\right]$	20		12.5 ± 3.9	15.8 ± 2.9
TH	$\frac{db}{dz}\ \left[\frac{1}{km}\right]$			0.021 ± 0.003	0.0253 ± 0.0036
	$\frac{db}{d\sigma}\ \left[\frac{1}{MPa}\right]$			0.0012 ± 0.0003	$(85.8 \pm 6.3)10^{-5}$
	$\frac{d\sigma}{dz}\ \left[\frac{MPa}{km}\right]$	45		17.5 ± 6.9	29.5 ± 6.2

Table 4.3: Depth-stress gradients summary. Black bold: values from Scholz [2015]. Red bold: uniform stress gradient assumed for the crust. Green bold: MLE best estimators from Table 4.2. Blue: analytical derivations (See Appendix C).

4. Conclusions for part 4

Numerical MLE approach is a valuable alternative to the analytical one for *b*-value estimations: by using local high-quality data, we have expressed different dependences for the *b*-value (tectonic styles, depth) through models of increasing complexity levels (i.e. number of free parameters *n*) in Southern California (SC). Statistical criteria of *AICc* and *BIC* have been used to account also for model complexities.

The assumption of constant *b*-value (Model 0) results in the worst MLE score. MLE score increases if we assume a linear decay of *b*-value with depth (Model 1), since stress state is thought to linearly increase in the shallow brittle crust: we have then obtained stress-depth gradients of *b*-value consistent with *Scholz* [2015] formulation. Tectonic style differentiation with constant *b*-values (Model 2.0) has a strong effect on data with respect to depth dependence: MLE score is higher and *AICc*/*BIC* are lower than the previous ones. Again, *b*-value variations can be also modeled as $-\sin\lambda$, by assuming a unit frequency and a zero phase but, unfortunately, without improving the fit.

The «best» models, according the established criteria, are the ones that assume a simultaneous dependence of *b*-value on tectonic styles and depth (Models 3.0, 3.1, 3.2) on SC dataset. Model 3.0 assumes linearity of *b*-values with depth with different slopes for different tectonic regimes, higher for TH faults, intermediate for SS faults and lower for NR faults, as expected by theory of faulting. This model has the highest MLE and the lower AICc, but it seems unsuitable for physical compares of the stress-depth gradients. Model 3.1 assumes the validity of the sinusoidal behavior of *b*-value on rake angle λ and a simultaneous linear overall dependence on depth. However, it does not do better that 3.0, in terms of MLE and *AICc*, but it improves the description, according to *BIC*. Finally, Model 3.2 gather together into a single expression the frictional properties of the crust, expressed by the friction coefficient μ, and the differentiation among different tectonic regimes, expressed by rake angle λ: the *b*-value oscillates on rake angle λ and contemporary decay linearly on depth, with different gradients, higher for thrust faults (where $\sin\lambda > 0$) and lower for normal faults ($\sin\lambda < 0$), as expected by theory of faulting. Moreover, it results in the best model according to BIC, and it allows for different stress-gradients estimations for different tectonic styles compatible to the ones expected by theory.

Part 5

MAIN CONCLUSIONS

1. Final results

The results of this Ph. D. thesis provide a set of useful and strong evidences, physically based, for the *b*-value dependence on differential stress combining basilar faulting theory, statistical modeling and new data analysis techniques.

By resuming the simple physical model of *Anderson* [1905] for earthquake faulting, we have evidenced how differences in frequency-magnitude distributions *b*-value are expected across different tectonic styles (normal, thrust and strike-slip), since different stress levels are observed for each of them. Such differences of *b* are quite marked looking at the global spatial distribution of *b*-values: *b* tends to decrease in high-stress zones and to increase in low-stress zones, surprisingly matching with the expected locations of the main seismotectonic structures of the globe. We thereby distinguish three main categories of global *b*-values (higher *b* for normal faulting/extensive regimes, intermediate *b* for strike-slip/FMs continental mixtures and lower *b* for thrust faulting/compressive regimes) in addition to be more specific for subduction zones characterization (high *b* for old / less buoyant slabs and low *b* for young / high buoyant slabs). Instead of using nodes on regular grids, we have tested and provided a new method for collecting hypocentral data: the selection of cylinders of increasing minimum radius account for reliable M_c and *b* parameters estimations. These results simultaneously agree both with expected theory of faulting (stress concentration is much higher for subduction trenches with respect to oceanic ridges) and with previous local studies.

The physics of the phenomenon does not change if we gather together similar FMs basing our analysis on hypocentral location or on rake angle, as done by *Schorlemmer et al.* [2003]. We have re-tested and extended their procedures, taking advantage of the significantly increased number of earthquakes, obtaining a temporal invariance of the *b*-rake trends. We have also reduced the width for the selections of rake (i.e. increasing the resolution), made each *b*-estimation independent to the other ones by rake-disjointed selections of FMs, proved statistical difference of estimations coming from different tectonic styles populations, provided alternative and fully consistent choices for the selection of the fault planes (random extractions and stack) and also showed that *b*-values behave as gaussian variables. These results are also confirmed computing *b*-values through the Tapered GR model [*Kagan and Schoenberg*, 2001, *Kagan*, 2002], which assumes the finiteness of the maximum possible magnitude. Then, we have also developed a different approach for the spatial characterization of our areas: we have computed cumulate mechanisms within a regular tessellation of Earth's surface, extracted their best double-couple rake angles and finally have computed *b*-values for sub-catalogs of similar cells coming from such rakes. The coherence of these results using all such different approaches and statistical techniques strongly support the argument that the variability of *b*-value as a function of the style of faulting is due to physical reasons and not to technical artifacts.

Important steps forward have been done also for the theoretical modeling of *b*-value dependence on differential stress, by proposing a harmonic functional behavior of *b*-value on rake angle of FMs, an inverse linear equation of normalized *b* with normalized stress for dip-slip mechanisms and a heuristic model which account for a simultaneous dependence of *b*-value on tectonic styles and stress (i.e. depth). The simple harmonic function fitted on the stacked *b*-values as a function of rake has unit frequency and zero phase, so indicating that deviations from the central *b*-value are about

proportional to -sin λ. As the orientation of the gravitational force component along the fault plane is $-\pi/2$, the amplitude of the variation would correspond to the scalar product between the co-seismic displacement and the gravity force component vectors. This means that the deviation from the average is about proportional to the amount of mechanical work done by the gravitational force during the earthquake. This inference has not an obvious physical interpretation but it might represent anyhow a valuable clue to understand the physical mechanism producing such *b*-value variations. Moreover, differences in *b*-value have been also detected, within thrust and normal (dip-slip) regimes, by using the ternary representation of FMs. However, such differences are also visible in our increased resolution plots (lower γ) but unexplainable without the usage of dip fault angles and of the MT principal axis plunge angles, since the sinusoidal model of *b* with rake is only a first approximation of a more realistic one. The detailed analytical derivation of differential stress in the ternary diagram explains what is missing: as expected from faulting theory, "non-pure" normal mechanisms, since they are subjected to lower differential stresses, can dip more than the "non-pure" thrust ones, which dip less. Deviation from the "pure" definitions (dip at 45°) are due to the presence of a non-zero friction coefficient, which is the controlling parameter for the re-activation processes of dip-slip faulting model, along the fracture surfaces.

Finally, by accounting for the linearity of stress with depth, the *b*-values, quantified as inversely linear with stress [*Scholz*, 2015], relative to different tectonic regimes are expected to decay with different depth/stress gradient in the Earth's crust. In fact, since stress is much higher for compressions, the gradient of thrust-events *b* is steeper than the one for normal mechanisms, which is lower. Again, the strike-slip fit in the middle of the previous two, with an intermediate gradient. The combination of a sinusoidal model of *b*-value with rake together with a linear decay of *b* with depth, whose gradient is in turn modulated by a sin λ term (maximum for thrust and minimum for normal), ensure a description of the physical reality with a reasonable complexity level. The last analyses collect all the previous pieces into a unique and more general frame for the dependence of the GR *b*-value on differential stress.

2. "Universal" *b* or "universal" *b*-gradients?

The remarkable consistency between the systematic *b*-value variations and the well-known tectonic features reflects theoretically expected stress differences in all considered details: high stress environments (compressive regimes, young subduction zones with low dipping angles, lower crust) result in lower *b*-values while low stress environments (extensive regimes, oceanic ridges, old subduction zones with high dipping angles, shallow crust) result in higher *b*-values.

However, since they were initially proposed, *b*-value variations theories have suffered sometimes hard critics, causing perplexities on the real meaning and origin of the variation from the "universal" assumed value of ~1. In the following paragraph, we will try to answer to most of the raised criticisms by recalling some of showed results.

First of all, the type of the "right" distribution for the number of occurrences of earthquakes with magnitude is the most common critic that is moved against *b*-value variations [*Kagan*, 2002]. The simple mostly used GR distribution should be replaced by a more complicated Tapered GR model,

accounting for the presence of the corner scalar moment, and able to fit high magnitude events. The corner moment (or magnitude) parameter, above which a decay in the number of events should be observed, determines a curvature point at high moments in the occurrences curve. It is necessary to say that, using the MLE method, m_{corn} is not always computable (as we tested by changing the starting initial points of the maximization algorithm), leaving some doubts about the necessity of complicate the occurrence model. In fact, the two models (see Fig. 3.8) basically match for a wide range of magnitude, sometimes departing at the very end of it with none effective change of the slope. When it is estimable, the corner magnitude (on a global scale) tends to converge to the maximum value, where its effect become negligible, far from moment/magnitude thresholds, where upwards shifts of *b*-value might be detected [*Kagan*, 2010]. The reason of the variation does not rely on the distribution choice.

According to *Kagan* [2002], the corner moment would result to be different for different tectonic regimes (higher for thrust/compressive regimes, intermediate for strike-slip/transcurrence and lower for normal/extensive regimes). Then, mixing populations of earthquakes with different tectonic settings or M_c, as done for example selecting data according to rake angle, would determine "false increases" in *b*-value. This statement can be denied by remembering that the *b*-value global map (Fig. 2.3), in which mechanisms with similar tectonics and Mc are selected, provides consistent results with the *b*-rake analysis. Moreover, we have also shown the spatial validity of the *b*-rake relation, by using a spatial criterion (MT summation) for the rake angles determination.

Another critic regards the usage of the "right" magnitude. According to *Kagan* [1999; 2003] only the usage of moment magnitude should be used, because inappropriate usage of magnitude scales other than the moment magnitude could determine significant, systematic and random errors, making them inappropriate for statistical analyses [*Kagan*, 2010]. However, this might significative limit the seismic analyses only to mid-to-high magnitudes seismicity ranges. In this thesis, we use different types of magnitude: the original GCMT Mw, a re-computed homogenized Mw from m_b and M_s original data [*Lolli et al*., 2014; 2015] and also a local magnitude for Southern California, obtaining results that are all consistent with the *b*-value variation theory, as widely exposed.

Last point is the depth of the earthquakes, which influences the corner magnitude according to *Kagan* [1999]. Shallow seismicity might result in increasing *b*-value: in fact, shallower events of Southern California are removed from the *b*-FM-depth analysis. On global scale, instead, depth dependence is completely ignored, because of the poorness of depth resolution, by selecting a constant depth range of 50 km in all the analyses.

Therefore, in the light of what has been shown, it is more appropriate to talk about of "universal" *b*-gradients with respect to a "universal" *b* of 1. Why the word "universal"? Because it has been shown that the structure high-mid-low *b*-values vs NR-SS-TH is conservative and systematic. The physics of the phenomenon is independent from the geographical scale (global or locale), from hypocentral location, from the type of chosen magnitude (moment magnitude, local magnitude, etc.), or from the selected time windows, and it is unrelated to bias/technical artifacts. Instead, it has a precise, clear and simple physical basis, as widely shown through all the statistical and technical methods so far used.

3. Future perspectives: earthquakes forecast?

This study thus greatly improves the believes that well-assessed *b*-value variations are meaningful for physical interpretation and consequently can provide valuable information for seismic hazard assessment.

In fact, the lack of knowledge of the states of stress in the Earth's crust is probably the key point for the absence of advanced forecasting techniques. Unfortunately, mankind is still far from a deterministic forecast of earthquakes, but *b*-value might play a first determinant role in such context.

The study of temporal series of this parameter might help seismologist for a "rude" forecast. For example, the detection of low *b*-values signal would indicate an increase in crustal stress conditions, and then in an increased probability of strong events to happen, while the detection of high *b*-values signal would indicate a post stress-release phase and a lower probability of mainshocks.

How can a similar apparatus be realized? It can be ideally realized by a real-time working network and by using a uniform and homogeneous magnitude through which computing *b*-values. The network should possibly cover most of the known seismogenic sources of the territory to monitor, in order to have, at each instant of time, a "sufficiently precise" picture of the *b*-value, i.e. of the stress conditions. In this way, it should be theoretically possible to distinguish the "high-zones" risk (low *b*-value) from the "low-zones" risk (intermediate, high *b*-value), at each instant of time, and try also to think about a first system of warning system.

Appendix A

General GR and tapered TAP probability density functions and Loglikelihood functions derivation

Gutenberg and Richter [1955] law can be expressed both with the decimal logarithm both with the natural logarithm

$$\log_{10} N(m) = a - bm \quad , \quad m \geq M_c \tag{A.1}$$

$$\ln N(m) = \alpha - \beta m \quad , \quad m \geq M_c \tag{A.2}$$

where

$$\beta = \ln 10 \; b \tag{A.3}$$

$$\alpha = \ln 10 \; a \tag{A.4}$$

In the natural logarithm form

$$N(m) = \exp[-\alpha] \exp[-\beta m] \tag{A.5}$$

The probability density function writes as

$$f(m|\beta) = \frac{N(m)}{\int_{M_c}^{+\infty} N(m')dm'} = \frac{\exp[-\beta m]}{\int_{M_c}^{+\infty} \exp[-\beta m']dm'} = \frac{\exp[-\beta m]}{-\frac{1}{\beta}\exp[-\beta m']_{M_c}^{+\infty}} = \beta \frac{\exp[-\beta m]}{\exp[-\beta M_c]} = \beta \exp[-\beta(m - M_c)] \tag{A.6}$$

By substituting β with b, it is possible to return to the decimal form

$$f(m|b) = b \ln 10 \exp[-b \ln 10 \, (m - M_c)] = b \ln 10 \; 10^{-b(m-M_c)} \tag{A.7}$$

where the last passage is guaranteed from $\ln\{\exp[-\beta(m - M_c)]\} = -\beta(m - M_c) = -b \, (m - M_c) \ln 10 \; = \ln 10^{-b(m-M_c)}$ so that $\exp[-b \ln 10 \, (m - M_c)] = 10^{-b(m-M_c)}$.

The Loglikelihood function is the product of the single PDF for each single observation

$$L = \ln \prod_{i=1}^{N} f(m_i) = \sum_{i=1}^{N} \ln f(m_i) = \sum_{i=1}^{N} \ln\{b \ln 10 \; 10^{-b(m_i - M_c)}\} = \sum_{i=1}^{N} \{\ln[b \ln 10] - b(m_i - M_c) \ln 10\} = N \ln[b \ln 10] - b \ln 10 \; \{\sum_{i=1}^{N} m_i - N M_c\} \tag{A.8}$$

According to the MLE method

$$\frac{\partial L}{\partial b} = 0 \; \Rightarrow \frac{N}{b} - \ln 10 \sum_{i=1}^{N} m_i + \ln 10 \, N M_c = \frac{1}{b \ln 10} - \bar{M} + M_c = 0$$

$$\Rightarrow b = \frac{1}{\ln 10 \, (\bar{M} - M_C)} = \frac{\log_{10} e}{\bar{M} - M_c} \tag{A.9}$$

which is the analytical formula of *Aki* (1965) for the *b*-value computation.

According to *Kagan* [2002a] (and references therein) the GR relation can be transformed into a *Pareto* (1897) power-law distribution for the seismic moment m (see part 1 paragraph 3.1). The probability density function for the Pareto distribution is

$$f(m|m_T, b^*) = \frac{b^*}{m}\left(\frac{m_T}{m}\right)^{b^*} \quad \text{(A.10)}$$

where m_T is the threshold moment (the analogous for M_c) and b^* is an asymptotic slope ($b^* = \frac{3}{2}b$). The cumulative function is

$$N(m|m_T, b^*) = \int f(m|m_T, b^*)dm = \left(\frac{m_T}{m}\right)^{b^*} \quad \text{(A.11)}$$

N is the number of earthquakes with seismic moment greater or equal to m. According to *Kagan* [2002a] the Pareto function A.11 needs to be modified at the large size end of the moment scale. The distribution tails should have a strong decay in the number of events: this problem is generally solved by introducing into the distribution an additional parameter above which the decay of high moment events should occur. Then, the cumulative function becomes

$$N(m|m_T, m_c, b^*) = \left(\frac{m}{m_T}\right)^{-b^*} \exp\left(\frac{m_T - m}{m_c}\right) \quad \text{(A.12)}$$

The so called *tapered* (TAP) GR relation has an exponential tapered-term applied to the cumulative number of events: the usage of the exponential term implies the existence of a corner moment m_c, which is the parameter controlling the distribution at high moments.

The relative PDF is computed as the first derivative (absolute value) of A.12

$$f(m|m_T, m_c, b^*) = \left[\frac{b^*}{m} + \frac{1}{m_c}\right]\left(\frac{m}{m_T}\right)^{-b^*} \exp\left(\frac{m_T - m}{m_c}\right) \quad \text{(A.13)}$$

For $m_c \to \infty$ equations A.12 and A.13 the relations of *Pareto* (1897) are easily re-obtained. The computation for the loglikelihood function is then straightforward

$$L = \ln \prod_{i=1}^{N} f(m_i) = \sum_{i=1}^{N} \ln\left\{\left[\frac{b^*}{m_i} + \frac{1}{m_c}\right]\left(\frac{m_i}{m_T}\right)^{-b^*} \exp\left(\frac{m_T - m_i}{m_c}\right)\right\} = \sum_i \ln\left[\frac{b^*}{m_i} + \frac{1}{m_c}\right] + \sum_i \ln\left[\frac{m_i}{m_T}\right]^{-b*} + \sum_i \left[\frac{m_T - m_i}{m_c}\right] = \sum_i \ln\left[\frac{b^*}{m_i} + \frac{1}{m_c}\right] + Nb^* \ln m_T - b^* \sum_i m_i + \frac{1}{m_c}\{Nm_T - \sum_i m_i\} \quad \text{(A.14)}$$

Appendix B

Dip-slip faulting model: quantitative analysis

According to Anderson's theory, for dip-slip faults the applied shear stress $\Delta\tau$ is (in absolute value)

$$|\Delta\tau| = \frac{1}{2}\Delta\sigma \sin 2\theta \tag{B.1}$$

where $\Delta\sigma$ is the differential (tectonic) stress and the angle θ is the complementary of the dip angle β = $\pi/2$ - θ. Then, it results the same in terms of β

$$|\Delta\tau| = \frac{1}{2}\Delta\sigma \sin 2\theta = \frac{1}{2}\Delta\sigma \sin[\pi - 2\beta] = \frac{1}{2}\Delta\sigma \sin 2\beta \tag{B.2}$$

We want to express the Anderson's faulting criterion for dip-slip faults in terms of δ_T along the bottom of the ternary diagram. The plunge angle δ_T is [*Gasperini and Vannucci*, 2003]

$$\delta_T = \arcsin(t_z) \tag{B.3}$$

t_z is the vertical component of the T-axis versor and can be computed by summing the vertical components of the outward normal n_z and of the slip vector d_z

$$t_z = \frac{n_z + d_z}{\sqrt{2}} \tag{B.4}$$

Such vectors are function of the dip angle β and of the rake angle λ

$$n_z = -\cos\beta \tag{B.5}$$

$$d_z = -\sin\beta \sin\lambda \tag{B.6}$$

Then, the plunge angle δ_T as function of dip and rake is

$$\delta_T = \arcsin\left[\frac{-\cos\beta - \sin\beta \sin\lambda}{\sqrt{2}}\right] \tag{B.7}$$

Along the bottom line connecting the normal vertex and the thrust vertex, the rake angle $\lambda = \pm 90°$ (see rake level curves in *Celerier* [2010] and Fig. 2.8b)

$$\delta_T = \arcsin\left[\frac{-\cos\beta \mp \sin\beta}{\sqrt{2}}\right] \tag{B.8}$$

where upper sign (-) applies to thrust faulting and lower sign (+) applies to normal faulting. Equation (2.8) can be rewritten as

$$\sqrt{2}\sin\delta_T = \begin{cases} -\cos\beta - \sin\beta & normal\ faulting \\ -\cos\beta + \sin\beta & thrust\ faulting \end{cases} \tag{B.9}$$

The linear combination, or harmonic addition, of sine and cosine waves is equivalent to a single sine wave with a phase term φ and an amplitude factor A

$$a\sin\alpha + b\cos\alpha = A\sin(\alpha + \varphi) \tag{B.10}$$

where the original amplitudes a and b summed in quadrature provide A

$$A = \sqrt{a^2 + b^2} \tag{B.11}$$

while

$$\varphi = \text{atan}\left(\frac{b}{a}\right) \tag{B.12}$$

Hence, thrust faulting provides two solutions for β as a function of δ_T (remembering that $\sin\alpha = \sin(180° - \alpha)$)

$$\sqrt{2}\sin\delta_T = \sqrt{2}\sin(\beta + 45°) \Rightarrow \beta = \delta_T - 45° \tag{B.13}$$

$$\sqrt{2}\sin\delta_T = \sqrt{2}\sin[180° - (\beta + 45°)] = \sqrt{2}\sin(135° - \beta) \Rightarrow \beta = 135° - \delta_T \tag{B.14}$$

Similarly, for normal faulting regimes the phase terms are -45° and 135°

$$\sqrt{2}\sin\delta_T = \sqrt{2}\sin(\beta - 45°) \Rightarrow \beta = \delta_T + 45° \tag{B.15}$$

$$\sqrt{2}\sin\delta_T = \sqrt{2}\sin(\beta + 135°) = \sqrt{2}\sin[180° - (45° - \beta)] = \sqrt{2}\sin(45° - \beta) \Rightarrow \beta = 45° - \delta_T \tag{B.16}$$

The 4 solutions (B.13-B.16) for β (two dips angles for two nodal planes and two tectonic styles), which describe how to pass from plunge δ_T to β (and viceversa) through linear relations, can be summarized as:

Normal faulting ($0° \leq \delta_T \leq 45°$) $$\beta(\delta_T) = \begin{cases} 45° - \delta_T \\ 45° + \delta_T \end{cases} \tag{B.17}$$

Thrust faulting ($45° \leq \delta_T \leq 90°$) $$\beta(\delta_T) = \begin{cases} \delta_T - 45° \\ 135° - \delta_T \end{cases} \tag{B.18}$$

So, "pure" normal and thrust dip at 45° while, as going toward the center, dip of one plane increases to 90° while the other decreases to 0° (see Fig. 2.9 b).

Moreover, the tectonic stress accompanying thrust faulting is about three times more the one required for normal faulting (*Turcotte and Schubert*, 2002). We can hence assume that

$$\Delta\sigma_{THR} = 3\Delta\sigma_{NORM} \tag{B.19}$$

The Anderson's faulting criterion for normal and thrust faulting regimes provide

$$|\tau_{NORM}| = \frac{1}{2}\Delta\sigma_{NORM}\sin[2(45° - \delta_T)] = \frac{1}{2}\Delta\sigma_{NORM}\sin[90° - 2\delta_T] = \frac{1}{2}\Delta\sigma_{NORM}\cos 2\delta_T \tag{B.20}$$

$$|\tau_{THR}| = \frac{1}{2}\Delta\sigma_{THR}\sin[2(\delta_T - 45°)] = \frac{1}{2}\Delta\sigma_{THR}\sin[2\delta_T - 90°] = -\frac{1}{2}\Delta\sigma_{THR}\cos 2\delta_T = -\frac{3}{2}\Delta\sigma_{NORM}\cos 2\delta_T \tag{B.21}$$

Pure (β= 45°) normal faulting mechanisms are under lower stress conditions with respect to thrust faulting regimes. As such mechanisms become more vertical/horizontal (i.e. as δ_T tends to 45° from both vertices) the requested tectonic stress $\Delta\sigma$ for faulting becomes always greater (Fig. 2.10 a).

We can assume that the vertical stress (σ_{zz}) is always the lithostatic pressure, while the horizontal stress (σ_{xx}) is altered by a tectonic stress $\Delta\sigma$ (assuming stresses are positive for compression):

$$\sigma_{zz} = \rho g z \tag{B.22}$$

$$\sigma_{xx} = \rho g z + \Delta\sigma \tag{B.23}$$

The tectonic stress ($\Delta\sigma$) is positive for thrust faulting regime, and negative for normal faulting. Since the vertical and horizontal stress are, in this case, also the maximum and minimum principal stress, the tectonic stress ($\Delta\sigma$) is also the differential stress (i.e. $\Delta\sigma = \sigma_1 - \sigma_3$).

Assuming this configuration, the derivation of the normal and shear stress along the fault zone is quite straight forward (e.g. *Zoback*, 2007; *Turcotte & Schubert*, 2002):

$$\sigma_n = \frac{\sigma_{zz}+\sigma_{xx}}{2} + \frac{\sigma_{zz}-\sigma_{xx}}{2}\cos(2\beta) = \rho g z + \frac{\Delta\sigma}{2}(1 - \cos(2\beta)) \tag{B.24}$$

$$\tau = \frac{\sigma_{zz}-\sigma_{xx}}{2}\sin(2\beta) = -\frac{\Delta\sigma}{2}\sin(2\beta) \tag{B.25}$$

again, with $\Delta\sigma$ positive for thrust faults and negative for normal faults.

Using a Mohr-Coulomb criterion defined as:

$$|\tau| = C + \mu(\sigma_n - p) \tag{B.26}$$

where *C* is the cohesion, μ is the frictional coefficient (between 0.6 and 1 for most rocks – *Turcotte & Schubert*, 2002) and p is the pore pressure (considered here as hydrostatic, and used for completeness).

Substituting the values for σ_n and τ as function of $\Delta\sigma$ we have:

$$|\tau| = \left|-\frac{\Delta\sigma}{2}\sin(2\beta)\right| = \begin{matrix} for\ thrust\ \Delta\sigma > 0\ then: \frac{\Delta\sigma}{2}\sin(2\beta) \\ for\ normal\ \Delta\sigma < 0\ then: -\frac{\Delta\sigma}{2}\sin(2\beta) \end{matrix} = \pm\frac{\Delta\sigma}{2}\sin(2\beta) \tag{B.27}$$

with the upper sign (+) for thrust and lower sign (-) for normal faulting regime. Then:

$$\pm\frac{\Delta\sigma}{2}\sin(2\beta) = C + \mu(\rho g z - p) + \mu\frac{\Delta\sigma}{2}(1 - \cos(2\beta)) \tag{B.28}$$

Finally solving for $\Delta\sigma$ we get equation (2.1):

$$\Delta\sigma = \frac{C + 2\mu(\rho g z - p)}{\pm\sin(2\beta) - \mu(1 - \cos(2\beta))} \tag{B.29}$$

If we assume a lithostatic stress $\sigma_{lith} = \rho g z - p \approx 83$ MPa (with density 2700 kg/m^3 and depth of 5000 m with hydrostatic pressure), a coefficient of friction of 0.6, and cohesionless fault (i.e. *C* = 0 MPa), we obtain the plot in Fig. 2.9 a.

Each *i*-th point in Fig. 2.9 c is *b*-stress normalized as

$$b_i' = \frac{b_i - b_{min}}{b_{max} - b_{min}} \tag{B.30}$$

$$\Delta\sigma_i' = \frac{1}{\sigma_{norm}}\Delta\sigma_i \tag{B.31}$$

where b_{min}=0.6, b_{max}=1.4, σ_{norm} is the stress normalization factor, which is the lithostatic pressure (83 MPa) for normal faulting and 400 MPa for thrust faulting.

Equation (B.29) admits real values if

$$\pm\sin(2\beta) - \mu(1 - \cos(2\beta)) \neq 0 \tag{B.32}$$

which can be rewritten as

$$\pm\sin(2\beta) + \mu\cos 2\beta \neq \mu \tag{B.33}$$

According to harmonic addition, the left term can be separated in (remembering that tangent is 180° periodic)

$$\sqrt{1+\mu^2}\sin[\pm 2\beta + \operatorname{atan}\mu] \neq \mu \tag{B.34}$$

$$\sqrt{1+\mu^2}\sin[\pm 2\beta + \operatorname{atan}\mu - \pi] \neq \mu \tag{B.35}$$

But, remembering that $\sin[\operatorname{atan}\mu] = \frac{\mu}{\sqrt{1+\mu^2}}$

$$\begin{cases} \sin[\pm 2\beta + \operatorname{atan}\mu] \neq \sin[\operatorname{atan}\mu] \\ \sin[\pm 2\beta + \operatorname{atan}\mu - \pi] \neq \sin[\operatorname{atan}\mu] \end{cases} \Rightarrow \begin{cases} \beta \neq 0° \\ \beta \neq 90° \end{cases} \tag{B.36}$$

for both tectonic styles. Using (B.17-B.18) these values correspond to $\delta_T \neq 45°$. $\delta_T = 45°$ hence represent a singularity of the problem.

Appendix C

b-value stress gradients: quantitative analysis

For strike-slip faulting, the state of stress describes horizontal motion in the xy plane while the lithospheric load lies along the vertical direction

$$\begin{cases} \sigma_x = \rho g z + \Delta\sigma_x \\ \sigma_y = \rho g z - \Delta\sigma_y \\ \sigma_z = \rho g z \end{cases} \quad \text{(C.1)}$$

By assuming that stresses are positive for compressions, along one of the horizontal directions (y) extension occurs while on the other one (x) compression occurs (see Figure C.1). For simplicity, we assume that the horizontal tectonic stresses $\Delta\sigma_x$ and $\Delta\sigma_y$ has the same value $\Delta\sigma/2$ ($|\Delta\sigma| > 0$), so that the maximum allowed tectonic stress is $\Delta\sigma = \Delta\sigma_x + \Delta\sigma_y$. We also hypothesize that horizontal directions (x and y) correspond to the maximum (σ_1) and minimum (σ_3) principal directions respectively. With this assumption, the tectonic stress is also the differential stress $\Delta\sigma = \sigma_1 - \sigma_3$.

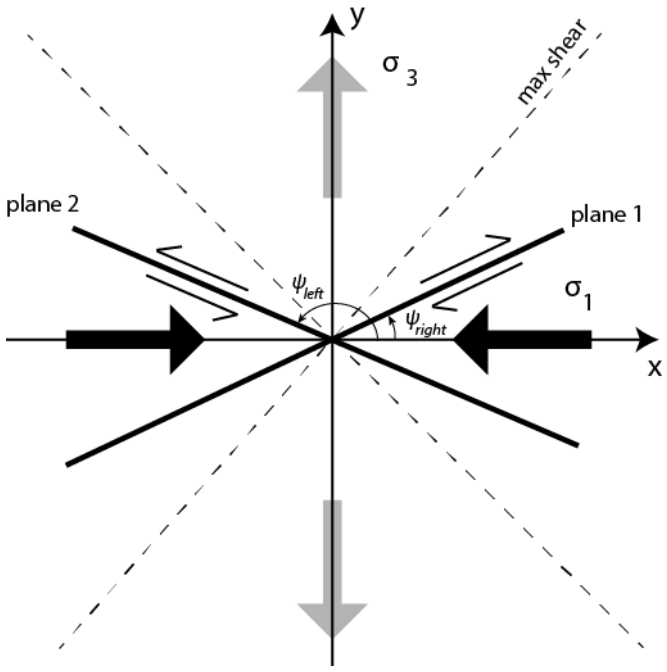

Figure C.1: Horizontal stress state for strike-slip faulting. Dashed lines indicate plane of maximum shear ($\psi = \pm 45°$)

We now consider a fault plane oriented of an angle ψ with respect to the σ_1 direction, where ψ ranges from 0 to 180°. With such scheme, the shear stress τ and the normal stress σ_n are

$$\begin{cases} \tau = -\frac{1}{2}(\sigma_x - \sigma_y)\sin 2\psi = -\frac{\Delta\sigma}{2}\sin 2\psi \\ \sigma_n = \frac{1}{2}(\sigma_x + \sigma_y) - \frac{1}{2}(\sigma_x - \sigma_y)\cos 2\psi = \rho g z - \frac{\Delta\sigma}{2}\cos 2\psi \end{cases} \quad \text{(C.2)}$$

The Mohr-Coulomb criterion is

$$|\tau| = \mu(\sigma_n - p) \tag{C.3}$$

where p is the hydrostatic pressure. By substituting previous expressions, the criterion becomes

$$\pm\frac{\Delta\sigma}{2}\sin 2\psi = \mu\left(\rho g z - \frac{\Delta\sigma}{2}\cos 2\psi - p\right) \tag{C.4}$$

which can be rearranged as an expression of the tectonic stress for strike-slip faulting

$$\Delta\sigma_{SS} = \frac{2\mu(\rho g z - p)}{\pm sin2\psi + \mu cos(2\psi)} \tag{C.5}$$

Upper sign applies if $\sin 2\psi > 0 \iff 0 < \psi < \frac{\pi}{2}$, compatible with a right-lateral transcurrent fault, lower sign if $\sin 2\psi < 0 \iff \frac{\pi}{2} < \psi < \pi$, compatible with a left-lateral transcurrent fault.

A strike-slip fault ruptures as soon as the instability condition $\frac{d(\Delta\sigma_{SS})}{d\psi} = 0$ holds, i.e. when

$$\pm\cos 2\psi - \mu\sin 2\psi = 0 \implies \tan 2\psi = \pm\frac{1}{\mu} \implies \begin{cases} \psi_{right} = \frac{1}{2}\text{atan}\left(\frac{1}{\mu}\right) \\ \psi_{left} = \frac{1}{2}\left(\pi + \text{atan}\left(-\frac{1}{\mu}\right)\right) = \frac{1}{2}\left(\pi - \text{atan}\left(\frac{1}{\mu}\right)\right) \end{cases} \tag{C.6}$$

Upper sign applies to right-lateral transcurrent faults with ψ lying in the first quadrant ($0 < \psi < \pi/2$),

$$\tan 2\psi = \frac{1}{\mu} \Rightarrow \psi_{right} = \frac{1}{2}\text{atan}\left(\frac{1}{\mu}\right) \tag{C.7}$$

Lower sign applies to left-lateral transcurrent faults with ψ lying in the second quadrant ($0 < \psi < \pi/2$), according to ψ definition. However, $\psi_{left} = -\frac{1}{2}\text{atan}\left(\frac{1}{\mu}\right)$ would result in an angle lying in the fourth quadrant (for which $\tan(2\pi - \alpha) = -\tan\alpha$), then

$$\tan 2\psi = -\frac{1}{\mu} \Rightarrow -\tan 2\psi = \tan(2\pi - 2\psi) = \frac{1}{\mu} \Rightarrow \psi_{left} = \pi - \frac{1}{2}\text{atan}\left(\frac{1}{\mu}\right) \tag{C.8}$$

Resuming

$$\tan 2\psi = \pm\frac{1}{\mu} \Longrightarrow \begin{cases} \psi_{right} = \frac{1}{2}\text{atan}\left(\frac{1}{\mu}\right) \\ \psi_{left} = \pi - \frac{1}{2}\text{atan}\left(\frac{1}{\mu}\right) \end{cases} \tag{C.9}$$

For a friction coefficient of $\mu = 0.6$, $\psi_{right} \approx 30°$ and $\psi_{left} \approx 150°$.

The equation which linearly links b-value and differential stress $\Delta\sigma$ (expressed in MPa) is eq. (1.28)

$$b(\Delta\sigma) = b_r - k\Delta\sigma$$

and consequently, for a strike-slip (SS) fault,

$$b_{SS} = b_r - k\frac{2\mu(\rho g z - p)}{\pm sin2\psi + \mu cos(2\psi)} \tag{C.10}$$

The depth gradient db/dz of b-value for a (right-lateral) strike-slip mechanisms is then

$$\left.\frac{db_{SS}}{dz}\right|_{right} = -k\frac{2\mu\rho g}{\pm sin2\psi + \mu cos(2\psi)} \tag{C.11}$$

Considering that $k = 0.0012\ MPa^{-1}, \mu = 0.6\,, \rho = 2700\,\frac{kg}{m^3}, g = 10\,\frac{m}{s^2}$ and $2\psi = 60°$

$$\frac{db_{SS}}{dz[km]_{right}} \sim -3.34 * 10^{-2} = -0.0335\ [km^{-1}]$$

For a left-lateral fault (lower sign and $2\psi = 120°$), the depth gradient of b-value has the same value

$$\frac{db_{SS}}{dz[km]_{left}} = -k\frac{2\mu\rho g}{-sin2\psi + \mu cos(2\psi)} \sim -3.34 * 10^{-2} = -0.0335\ [km^{-1}]$$

Equation (C.11) can be also expressed, by using (C.9) and remembering that $\sin(\text{atan}\ x) = \frac{x}{\sqrt{1+x^2}}$ and $\cos(\text{atan}\ x) = \frac{1}{\sqrt{1+x^2}}$, as a function of the friction only

$$\frac{db}{dz[km]_{SS}} = -k\frac{2\mu\rho g}{\sqrt{\mu^2+1}} \tag{C.12}$$

The derivation of the differential stress for dip-slip (normal and thrust, see Figure C.2) faults is similar (Appendix B) to the strike-slip case

$$\Delta\sigma_{dip-slip} = \frac{2\mu(\rho g z - p)}{\pm sin2\theta - \mu(1+\cos 2\theta)} \tag{C.13}$$

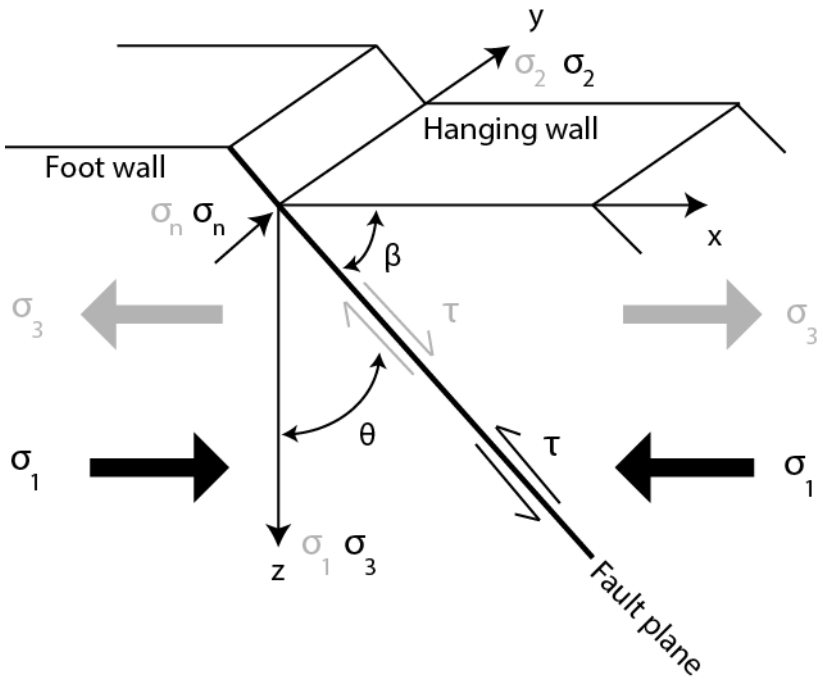

Figure C.2: Faulting schemes and principal stress axes orientations for dip-slip mechanisms: normal faulting (indicated with gray color) accompanies extensions (σ_3 is horizontal and σ_1 is vertical) while thrust faulting (black) determines compressions (σ_1 is horizontal and σ_3 is vertical).

Upper sign applies to thrust faults and lower sign to normal faults. The angle θ (with $0 < \theta < \pi/2$) is the complementary of the dip angle β, $\theta = 90° - \beta$. The value of θ that gives the minimum value of $|\Delta\sigma_{dip-slip}|$ is determined setting $\frac{d\Delta\sigma_{dip-slip}}{d\theta} = 0$ with the result

$$\tan 2\theta = \mp\frac{1}{\mu} \Rightarrow \begin{cases} \theta_{thrust} = \frac{1}{2}\left(\pi - \text{atan}\left(\frac{1}{\mu}\right)\right) \\ \theta_{normal} = \frac{1}{2}\text{atan}\left(\frac{1}{\mu}\right) \end{cases} \tag{C.14}$$

For normal faulting regime and keeping a coefficient of friction of 0.6

$$\tan 2\theta = \frac{1}{\mu} \Rightarrow \theta_{normal} = \frac{1}{2}\operatorname{atan}\left(\frac{1}{\mu}\right) \approx 30°\,, \beta \approx 60°$$

For thrust faulting regime, instead, $\tan 2\theta = -\frac{1}{\mu}$ would result in a negative angle *-2θ* lying in the fourth or, equivalently, in the second quadrant shifted of π. Then, rearranging (C.14) and using μ=0.6

$$-\tan 2\theta = \tan(\pi - 2\theta) = \frac{1}{\mu} \Rightarrow \theta_{thrust} = \frac{\pi}{2} - \frac{1}{2}\operatorname{atan}\left(\frac{1}{\mu}\right) \approx 60°\,, \beta \approx 30°$$

Normal faults dip more than thrust faults, as expected by *Anderson* (1905).

Then, the depth gradient of *b*-value for normal faults is (tectonic stress is negative for extension, so we set the absolute value)

$$\frac{db_{NR}}{dz} = -k\left|\frac{2\mu\rho g}{-sin2\theta - \mu(1+cos(2\theta))}\right| \qquad \text{(C.15)}$$

For normal (NR) faulting regimes, if $\mu = 0.6$, $\theta \approx 30°$ (or $\beta \approx 60°$), giving

$$\frac{db_{NR}}{dz\,[km]} \sim -0.022\ [km^{-1}]$$

Similarly, the depth gradient of *b*-value for thrust (TH) faults is

$$\frac{db_{TH}}{dz} = -k\left|\frac{2\mu\rho g}{sin2\theta - \mu(1+cos(2\theta))}\right| \qquad \text{(C.16)}$$

For thrust faulting regimes, if $\mu = 0.6\,, \theta \approx 60°$ (or $\beta \approx 30°$), giving

$$\frac{db_{TH}}{dz\,[km]} \sim -0.0687\ [km^{-1}]$$

Again, equations C.15 e C.16 can be reduce to a form only friction dependent, as done for SS case

$$\frac{db}{dz}_{NR} = -k\frac{2\mu\rho g}{\sqrt{\mu^2+1}+\mu} \qquad \text{(C.17)}$$

$$\frac{db}{dz}_{TH} = -k\frac{2\mu\rho g}{\sqrt{\mu^2+1}-\mu} \qquad \text{(C.18)}$$

Stress-depth gradients: errors estimation for Table 4.3

Scholz [2015] model

Scholz [2015] provides a value for the *b*-stress gradient for the entire crust

$$\frac{db}{d\sigma} = k = (0.0012 \pm 0.0003)\ MPa^{-1} \tag{C.19}$$

Then, the *b*-depth gradient can be estimated as

$$\frac{db}{dz} = \frac{db}{d\sigma}\frac{d\sigma}{dz} = C\frac{db}{d\sigma} = C\ k \tag{C.20}$$

if a uniform depth gradient of stress C = 15 MPa is assumed for the entire crust (see equation 4.9). Since C is a quantity assumed exact, the error on the *b*-depth gradient is

$$\delta\left(\frac{db}{dz}\right) = C\ \delta(k) \tag{C.21}$$

Model 1: b(z)

Model 1 is based on the same hypotheses of Scholz [2015]. This time, what is known from data is the *b*-depth gradient with its error (Table 4.2). Then, we can reverse the previous relation for the *b*-stress gradient

$$\frac{db}{d\sigma} = \frac{1}{C}\frac{db}{dz} \tag{C.22}$$

with error

$$\delta\left(\frac{db}{d\sigma}\right) = \frac{1}{C}\delta\left(\frac{db}{dz}\right) \tag{C.23}$$

Model 3.0: b(z, FM)

For Model 3.0, instead, from the MLE maximizations we estimate three different *b*-depth gradients with relative errors (Table 4.2). By hypotheses, we cannot extract overall stress/ depth gradients from this model. On the contrary, we can estimate the depth-gradients of differential stress and compare them to the estimations provided by Scholz [2015] for each tectonic environment (Table 4.3, first column, NR SS TH rows). We obtain

$$\frac{d\sigma}{dz} = \frac{d\sigma}{db}\frac{db}{dz} = \frac{1}{k}\frac{db}{dz} \tag{C.24}$$

where, currently, we assume for the sake of simplicity that we have a unique gradient of b with stress k, given by Scholz [2015]. Now, it is the necessary to propagate the error, because the factor k is known with its uncertainty

$$\frac{\delta\left(\frac{d\sigma}{dz}\right)}{\frac{d\sigma}{dz}} = \frac{\delta(k^{-1})}{k^{-1}} + \frac{\delta\left(\frac{db}{dz}\right)}{\frac{db}{dz}} = \frac{\delta(k)}{k} + \frac{\delta\left(\frac{db}{dz}\right)}{\frac{db}{dz}} \tag{C.25}$$

Model 3.2: b(λ,z)

Model 3.2, as it is thought, allows to compute both overall and single-style gradients. In fact, from Table 4.2, the overall stress-gradient of b results

$$\kappa = \frac{db}{d\sigma} = (85.8 \pm 6.32)10^{-5}\ MPa \tag{C.26}$$

that can be easily turned into an overall depth-gradient (to be compared with previous overall estimations, Table 4.3, first row)

$$\frac{db}{dz} = C\frac{db}{d\sigma} = C\ \kappa \tag{C.27}$$

As regarding the single-style gradients, we can refer to equation (4.26) and differentiate among different styles (sin of the rake λ) by assuming -1 for NR, 0 for SS and +1 for TH. This time, for the error estimation of each b-depth gradient, we have to take into account of two uncertainties (on friction μ and b-stress κ), so that

$$\frac{\delta\left(\frac{db}{dz}\right)}{\frac{db}{dz}} = \frac{\delta(\kappa)}{\kappa} + \frac{\delta\left(\frac{\mu}{\sqrt{\mu^2+1}-\mu\sin\lambda}\right)}{\frac{\mu}{\sqrt{\mu^2+1}-\mu\sin\lambda}} \tag{C.28}$$

where

$$\delta\left(\frac{\mu}{\sqrt{\mu^2+1}-\mu\sin\lambda}\right) = \left|\frac{d}{d\mu}\left[\frac{\mu}{\sqrt{\mu^2+1}-\mu\sin\lambda}\right]\right|\delta(\mu) = \frac{1-\mu^2}{\left[\sqrt{\mu^2+1}\right]\left[\sqrt{\mu^2+1}-\mu\sin\lambda\right]^2}\delta(\mu) \tag{C.29}$$

Then

$$\frac{\delta\left(\frac{db}{dz}\right)}{\frac{db}{dz}} = \frac{\delta(\kappa)}{\kappa} + \frac{1-\mu^2}{\mu\left[\sqrt{\mu^2+1}\right]\left[\sqrt{\mu^2+1}-\mu\sin\lambda\right]}\delta(\mu) \tag{C.30}$$

The passage to a stress-depth gradient, for a compare with Scholz [2015] 's values (Table 4.3 first column, NR, SS, TH rows), is then guaranteed from equation 4.27 with errors

$$\frac{\delta\left(\frac{d\sigma}{dz}\right)}{\frac{d\sigma}{dz}} = \frac{\delta(\kappa)}{\kappa} + \frac{\delta\left(\frac{db}{dz}\right)}{\frac{db}{dz}} \tag{C.31}$$

List of symbols and acronyms

Used symbols

b : b-value of *Gutenberg and Richter* [1944] law

b^* : asymptotic slope for tapered GR model

b_0 : offset for the sinusoidal model

b_r: offset for *Scholz* [2015] equation

f : probability density function

$\mathbf{g}$: gravity

L: loglikelihood function

k: b-stress gradient *Scholz* [2015]

M : magnitude

m : scalar moment (N m)

M_c : magnitude of completeness

M_{corn} : corner magnitude

m_C : scalar corner moment (N m)

m_{ij} : moment tensor component

MT : moment tensor

m_T : scalar threshold moment (N m)

N : number of events

$\mathbf{n}$: number of free parameters

$\mathbf{p_w}$: hydrostatic pressure

$\mathbf{z}$: hypocentral depth

$\boldsymbol{\alpha}$: amplitude of sinusoidal model

$\boldsymbol{\beta}$: dip angle

γ : window width parameter for the b- λ trend

$\boldsymbol{\delta}$: plunge angle

ΔM : magnitude binning

$\boldsymbol{\Delta\sigma}$: differential (tectonic) stress

$\boldsymbol{\theta}$: complementary of β

$\boldsymbol{\lambda}$: rake angle

$\boldsymbol{\mu}$: friction

$\boldsymbol{\varrho}$: density

$\boldsymbol{\kappa}$: estimated b-stress gradient

$\boldsymbol{\sigma}$: standard deviation

$\boldsymbol{\sigma_{1,2,3}}$: principal stresses

$\boldsymbol{\sigma_n}$: normal stress

$\boldsymbol{\sigma_{x,y,z}}$: horizontals and vertical stresses

$\boldsymbol{\tau}$: shear stress

$\boldsymbol{\varphi}$: phase term of the sinusoidal model

ψ : angle formed by the principal stresses and the fault plane for strike-slip

$\boldsymbol{\omega}$: frequency of the sinusoidal model

Acronyms

AIC: Akaike Information Criterion

ALU : Alaska-Aleutians

BIC : Bayesian Information Criterion

CAS : Cascadia

CLVD : Compensated Linear Vector Dipole

CMT : Centroid Moment Tensor

CSD : Cascadia

FM: focal mechanism

FMD: Frequency-Magnitude Distribution

GCMT: Global Centroid Moment Tensor

GR: *Gutenberg and Richter* [1944] law

IZU : Izu-Bonin

KER : Kermandec Tonga

KUR : Kamchatka/Kurils/Japan

MEX : Central America

MBS : Mc-to-B-value-Stability

MLE : Maximum Likelihood estimation

MT : Moment Tensor

NR: normal faulting regime

PDF: probability density function

PHI : Philippines

RYU : Ryukyu

SAF : San Andreas Fault

SC : Southern California

SCO : Scotia

SL : significance level

SS: strike-slip faulting regime

SOL : Solomon Islands

SUM : Sumatra

TH: thrust faulting regime

VAN: Santa Cruz Islands/Vanuatu/Loyalty Islands

List of figures and tables

Part 1

Part 2

Part 3

Part 4

Acknowledgments

All computations and plots are performed in MATLAB® while maps of Figs. 2.4 and 4.1 come from GMT (http://gmt.soest.hawaii.edu/) software [*Wessel and Smith*, 1998].

Some computations toke advantages of ZMAP package [*Wiemer*, 2001] (http://mercalli.ethz.ch/~eberhard/zmap.zip).

Thanks

A Ph. D. route is a long-way, hard and challenging experience that cannot be completed without the sustain of the many professional figures I have the honor and the pleasure to work with.

First of all, my supervisor Prof. Paolo Gasperini, who initiated me to the study of the statistical seismology, helping, suggesting and guiding me through most of the theoretical and technical aspects of the analyses.

Then, I would like to thank all the ETH staff members, especially Prof. Stefan Wiemer and Thessa Tormann, who kindly invited me to the SED for my abroad period experience in Zürich. There, I had the unique chance to interact with a new, highly-stimulant scientific environment, to extend my seismological knowledge background and to greatly improve my computational and linguistic skills.

A special thank goes to Danijel Schorlemmer, with whom I spent a very good time of work and fun in Potsdam.

Last but not least, I would like also to thank Gianfranco Vannucci, for the always-wise suggestions and the always-ready replies to my numerous drafts, and Antonio Pio Rinaldi, for the precious help in the faulting model development.

Ph. D. is not only a study path, but also the continuation of a life one supported by the people I love.

Then, I want also to thank Valentina, real engine of my life, and my family - my mom Maria and dad Gianluigi, my brothers Giovanni and Andrea, and my "second-mummy" aunt Giovanna - who has never stopped believing in me during all these years.

Thank you all

Antonio

References

Akaike, Hirotugu (December 1974). "A new look at the statistical model identification". IEEE Transactions on Automatic Control 19 (6): 716–723. doi:10.1109/TAC.1974.1100705.

Aki, K. (1965), Maximum likelihood estimate of b in the formula log N = a−bM and its confidence limits, Bull. Earthquake Res. Inst. Univ. Tokyo, 43, 237–239.

Álvarez-Gómez, J.A. (2014) FMC: a one-liner Python program to manage, classify and plot focal mechanisms. Geophysical Research Abstracts, Vol. 16, EGU2014-10887.

Amitrano, D. (2003). Brittle-ductile transition and associated seismicity: Experimental and numerical studies and relationship with the b value, J. Geophys. Res., 108(B1), 2044, doi:10.1029/2001JB000680.

Amorese, D. (2007), Applying a change-point detection method on frequency-magnitude distributions, Bull. Seismol. Soc. Am., 97, doi:10.1785/0120060181

Anderson, E. M., The dynamics of faulting, Trans. Edinburgh Geol. Soc., 8 (1905), pp. 387–402.

Bachmann, C. E., S. Wiemer, B. P. Goertz-Allmann, and J. Woessner (2012), Influence of pore-pressure on the event-size distribution of induced earthquakes, Geophys. Res. Lett., 39, L09302, doi:10.1029/2012GL051480.

Baker, E. T., R. W. Embley, S. L. Walker, J. A. Resing, J. E. Lupton, K.-I. Nakamura, C. E. J. de Ronde, and G. J. Massoth (2008), Hydrothermal activity and volcano distribution along the Mariana arc, J. Geophys. Res., 113, B08S09, doi:10.1029/2007JB005423.

Bender, B. (1983), Maximum Likelihood estimation of b values for magnitude grouped data, Bull. Seism. Soc. Am., 73, 831-851.

Bird, P. (2003) An updated digital model of plate boundaries, Geochemistry Geophysics Geosystems, 4(3), 1027, doi:10.1029/2001GC000252.

Bird, P. & Kagan, Y. Y. (2004), Plate-Tectonic Analysis of Shallow Seismicity: Apparent Boundary Width, Beta, Corner Magnitude, Coupled Lithosphere Thickness, and Coupling in Seven Tectonic Settings, Bull. Seism. Soc. Am., 94, 2380–2399.

Boettcher, M. S., and T. H. Jordan (2004), Earthquake scaling relations for mid-ocean ridge transform faults, J. Geophys. Res., 109, B12302, doi:10.1029/2004JB003110.

Bonner, J. L., Blackwell, D.D. & Herrin, E.T., 2003. Thermal constraints on earthquake depths in California, Bull. seism. Soc. Am., 93(6), 2333–2354.

Brace, W. F. and Kohlstedt, D., (1980), Limits on the lithospheric stress imposed by laboratory experiments, J. Geophys. Res., 85: 6248-6252

Brace, W. F., & Byerlee, J. D. (1966). Stick-slip as a mechanism for earthquakes. Science, 153, 990-992.

Brune, J. (1968), Seismic moment, seismicity and rate of slip along major fault zones, J. Geophys. Res., 73: 777-784

Brune, J. N., Henyey, T. L. & Roy, R. F. (1969) Heat flow, stress, and rate of slip along the San Andreas Fault, California. J. Geophys. Res. 74, 3821–3827.

Burnham, K. P.; Anderson, D. R. (2004), "Multimodel inference: understanding AIC and BIC in Model Selection" (PDF), Sociological Methods & Research, 33: 261–304, doi:10.1177/0049124104268644

Byerlee, J. D. (1978), Friction of rocks, Pure Appl. Geophys., 116: 615-626

Cao, A., and S.S. Gao (2002), Temporal variation of seismic b-values beneath northeastern Japan island arc, Geophys. Res. Lett., 29, 9, 1334, doi:10.1029/2001GL013775.

Carpenter, D. M., C. Marone & D. M. Saffer, (2011), Weakness of the San Andreas Fault revealed by samples from the active fault zone, Nat. Geosc. 4, 251–254, doi:10.1038/ngeo1089

Cavanaugh, J. E. (1997), "Unifying the derivations of the Akaike and corrected Akaike information criteria", Statistics & Probability Letters, 31: 201–208, doi:10.1016/s0167-7152(96)00128-9

Célérier, B. (2010), Remarks on the relationship between the tectonic regime, the rake of the slip vectors, the dip of the nodal planes, and the plunges of the P, B, and T axes of earthquake focal mechanisms, Tectonophysics, 482, 42–49, doi:10.1016/j.tecto.2009.03.006

Célérier, B., 1988. How much does slip on reactivated fault plane constrain the stress tensor? Tectonics 7 (6), 1257–1278.
Célérier, B., 2008. Seeking Anderson's faulting in seismicity: a centennial celebration. Rev. Geophys. 46 (RG4001), 1–34, doi:10.1029/2007RG000240.

Chen, A. T., C. Frohlich, and G. V. Latham (1982), Seismicity of the forearc marginal wedge (accretionary prism), J. Geophys. Res., 87(B5), 3679–3690, doi:10.1029/JB087iB05p03679.

Dziewonski, A. M., Ekström, G., and Maternovskaya, N. N. (1998), Centroid-moment Tensor Solutions for October–December, 1996, Phys. Earth Planet. Inter. 105, 95–108

Dziewonski, A. M., T.-A. Chou and J. H. Woodhouse, (1981), Determination of earthquake source parameters from waveform data for studies of global and regional seismicity, J. Geophys. Res., 86, 2825-2852, 1981. doi:10.1029/JB086iB04p02825.

Efron, B. (1987). Better bootstrap confidence intervals. Journal of the American Statistical Association, 82, 171–185, doi:10.2307/2289144.

Efron, B., & Tibshirani, R. J. (1993). An introduction to the bootstrap. Boca Raton, FL: Chapman & Hall.

Ekström, G., and P. England (1989), Seismic strain rates in regions of distributed continental deformation, J. Geophys. Res., 94(B8), 10231–10257, doi:10.1029/JB094iB08p10231.

Ekström, G., M. Nettles, and A. M. Dziewonski, (2012), The global CMT project 2004-2010: Centroid-moment tensors for 13,017 earthquakes, Phys. Earth Planet. Inter., 200-201, 1–9, doi:10.1016/j.pepi.2012.04.002.

Ernst, W., E. Van der Heuvel, J-W. Romeyn (2012). "'All models are wrong...': an introduction to model uncertainty". Statistica Neerlandica. 66 (3): 217–236. doi:10.1111/j.1467-9574.2012.00530.x

Farrell, J., S. Husen, R.B. Smith (2009), Earthquake swarm and b-value characterization of the Yellowstone volcano-tectonic system, J. of Volcanology and Geothermal Res., 188, 260–276.

Fisher, R.A. (1950): Contribution to Mathematical Statistics (Wiley, New York).

Fröhlich, C. (1992), Triangle diagrams: Ternary graphs to display similarity and diversity of earthquake focal mechanisms, Physics of The Earth and Planetary Interiors, 75(1), 193–198, doi: 10.1016/0031-9201(92)90130-N.

Fröhlich, C. (2001), Display and quantitative assessment of distributions of earthquake focal mechanisms. Geophysical Journal International, 144: 300–308. doi:10.1046/j.1365-246x.2001.00341.x.

Fröhlich, C., and K. D. Apperson (1992), Earthquake focal mechanisms, moment tensors, and the consistency of seismic activity near plate boundaries, Tectonics, 11(2), 279–296, doi:10.1029/91TC02888.

Fröhlich, C., S. Billington, E. R. Engdahl, and A. Malahoff, (1982), Detection and location of earthquakes in the Central Aleutian Subduction Zone using island and ocean bottom seismograph stations, J. Geophys. Res., 87(B8), 6853–6864, doi:10.1029/JB087iB08p06853.

Fuller, W. A., 1987, Measurement Error Models, Wiley, pag 440

Gasperini P. and Vannucci G. (2003). FPSPACK: A package of simple Fortran subroutines to manage earthquake focal mechanism data, Computers & Geosciences, 29/7, 893-901, doi:10.1016/S0098-3004(03)00096-7.

Gasperini P., Lolli B. and Vannucci G. (2013). Body-Wave Magnitude mb Is a Good Proxy of Moment Magnitude Mw for Small Earthquakes (mb < 4.5–5.0), Seism. Res. Lett., 84, 932-937, doi: 10.1785/0220130105.

Ghosh, A., A.V. Newman, A.M. Thomas, and G.T. Farmer (2008), Interface locking along the subduction megathrust from b-value mapping near Nicoya Peninsula, Costa Rica, Geophys. Res. Lett., 35, L01301, doi:10.1029/2007GL031617.

Goebel, T. H. W., D. Schorlemmer, T. W. Becker, G. Dresen, and C. G. Sammis (2013), Acoustic emissions document stress changes over many seismic cycles in stick-slip experiments, Geophys. Res. Lett., 40, 2049–2054, doi:10.1002/grl.50507.

Goebel, T. H. W., T. W. Becker, D. Schorlemmer, S. Stanchits, C. Sammis, E. Rybacki, and G. Dresen (2012), Identifying fault heterogeneity through mapping spatial anomalies in acoustic emission statistics, J. Geophys. Res., 117, B03310, doi:10.1029/2011JB008763.

Gulia, L., and S. Wiemer (2010), The influence of tectonic regimes on the earthquake size distribution: A case study for Italy, Geophys. Res. Lett., 37, L10305, doi:10.1029/2010GL043066.

Gulia, L., T. Tormann, S. Wiemer, M. Herrmann, and S. Seif (2016), Short-term probabilistic earthquake risk assessment considering time-dependent b-values, Geophys. Res. Lett., 43, 1100–1108, doi:10.1002/2015GL066686.

Gutenberg, R. and C. Richter (1944), Frequency of earthquakes in California, Bull. Seismol. Soc. Am., 34, 185–188.

Hardebeck, J. L., & Shearer, P. M. (2002). A New Method for Determining First-Motion Focal Mechanisms. Bulletin of the Seismological Society of America, 92(6), 2264-2276. doi: 10.1785/0120010200.

Hardebeck, J. L., & Shearer, P. M. (2003). Using S/P Amplitude Ratios to Constrain the Focal Mechanisms of Small Earthquakes. Bulletin of the Seismological Society of America, 93(6), 2434-2444. doi: 10.1785/0120020236.

Hauksson E., 2011, Crustal geophysics and seismicity in southern California, *Geophys. J. Int.* 186**,** 82–98, doi: 10.1111/j.1365-246X.2011.05042.x

Hauksson E., W. Yang and P.M. Shearer, Waveform relocated earthquake catalog for southern California (1981 - 2011), Bull. Seismol. Soc. Am., Vol. 102, No. 5, October 2012, doi:10.1785/0120120010, 2012.

Hauksson, E. (1990). Earthquakes, faulting, and stress in the Los Angeles basin, J. Geophys. Res. 95, no. B10, 15,365–15,394, doi 10.1029/JB095iB10p15365.

Hayes, G. P., Wald, D. J. & Johnson, R. L. (2012) Slab1.0: A three-dimensional model of global subduction zone geometries. J. Geophys. Res. Solid Earth 117,.

Hutton, K., J. Woessner, and E. Hauksson (2010), Earthquake monitoring in southern california for seventy-seven years (1932-2008), Bull. Seismol. Soc. Am., 100, 423{446, doi:10.1785/0120090130.
Ishimoto, M. and Iida, K., 1939. Observations sur les seismes enregistres parle microsismographe construit dernierement (1). Bull. Earthquake Res. Inst., Univ. Tokyo 17: 443-478 (in Japanese with French abstract).

Jackson, D. D., and Y. Y. Kagan (1999). Testable earthquake forecasts for 1999, Seism. Res. Lett. 70, 393–403.

Jackson, J. and McKenzie, D. (1988), The relationship between plate motions and seismic moment tensors, and the rates of active deformation in the Mediterranean and Middle East. Geophys. J., 93: 45–73. doi:10.1111/j.1365-246X.1988.tb01387.x

Kagan, Y. Y. (1997), Seismic moment-frequency relation for shallow earthquakes: Regional comparison, J. Geophys. Res., 102(B2), 2835–2852, doi:10.1029/96JB03386.

Kagan, Y. Y. (1999), Universality of the seismic moment-frequency relation ,Pure Appl. Geophys. 155: 537, doi:10.1007/s000240050277.

Kagan, Y. Y. (2002a), Seismic moment distribution revisited: I. Statistical results. Geophysical Journal International, 148: 520–541. doi:10.1046/j.1365-246x.2002.01594.x.

Kagan, Y. Y. (2002b), Seismic moment distribution revisited: II. Moment conservation principle. Geophysical Journal International, 149: 731–754. doi:10.1046/j.1365-246X.2002.01671.x.

Kagan, Y. Y. (2005), Earthquake slip distribution: A statistical model, J. Geophys. Res., 110, B05S11, doi:10.1029/2004JB003280.

Kagan, Y. Y., and D. D. Jackson (2000). Probabilistic forecasting of earthquakes, Geophys. J. Int. 143, 438–453.

Kagan, Y.Y. (2003), Accuracy of modern global earthquake catalogs, Phys. Earth planet. Inter., 135 2 3, 173-209.

Kagan, Y.Y. (2010). Earthquake size distribution: Power-law with exponent β≡1/2, Tectonophysics, 490, 103–114, doi:10.1016/j.tecto.2010.04.034.

Kagan, Y.Y. & Schoenberg, F., 2001. Estimation of the upper cutoff parameter for the tapered Pareto distribution, J. appl. Probab., 38A, 168–185.

Kanamori H (1979). A moment magnitude scale. Journal of Geophysical Research, 84 (B5): 2348-50.

Katsumata, M., and L. R. Sykes, (1969), Seismicity and tectonics of the western Pacific: Izu-Mariana-Caroline and Ryukyu-Taiwan regions, J. Geophys. Res., 74, 5923-5948

Kijko, A. & Graham, G., 1998. Parametric-historic procedure for probabilistic seismic hazard analysis—Part I: Estimation of maximum regional magnitude mmax, Pure appl. Geophys., 152, 413–442.

Kirby, S. (1980), Tectonic stress in the lithosphere: constraints provided by the experimental deformation of rock, J. Geophys. Res., 85: 6353-6363

Kostrov, V.V. (1974), Seismic moment and energy of earthquakes and seismic flow of rocks, Izv. Acad. Sci. USSR, Phys. Solid Earth, 1, 23-40.

Lachenbruch, A. H. & Sass, J. H. Heat flow and energetics of the San Andreas Fault Zone. J. Geophys. Res. 85, 6185–6223 (1980).

Lilliefors, H. W. "On the Kolmogorov-Smirnov test for normality with mean and variance unknown." Journal of the American Statistical Association. Vol. 62, 1967, pp. 399–402.

Lilliefors, H. W. "On the Kolmogorov-Smirnov test for the exponential distribution with mean unknown." Journal of the American Statistical Association. Vol. 64, 1969, pp. 387–389.

Lolli, B., Gasperini P. and Vannucci G. (2014). Empirical conversion between teleseismic magnitudes (mb and Ms) and moment magnitude (Mw) at the Global, Euro-Mediterrean and Italian scale. Geophys. J. Int., 199, 805-828.

Lolli, B., P. Gasperini, G. Vannucci (2015), Erratum: Empirical conversion between teleseismic magnitudes (mb and Ms) and moment magnitude (Mw) at the Global, Euro-Mediterranean and Italian scale, Geophys. J. Int. , 200, 199 – 199.

Main, I. (1996), Statistical physics, seismogenesis, and seismic hazard, Rev. Geophys., 34(4), 433–462, doi:10.1029/96RG02808.

McKenzie, D.P.,1969. The relation between fault plane solutions for earthquakes and the directions of the principal stresses. Bull. Seismol. Soc. Am. 59, 591–601.

Mignan, A. (2012), Functional shape of the earthquake frequency-magnitude distribution and completeness magnitude, J. Geophys. Res., 117, B08302, doi: 10.1029/2012JB009347

Mignan, A. and J. Woessner (2012), Estimating the magnitude of completeness for earthquake catalogs, Community Online Resource for Statistical Seismicity Analysis, doi: 10.5078/corssa-00180805. Available at http://www.corssa.org.

Mignan, A., M. J. Werner, S. Wiemer, C.-C. Chen and Y.-M. Wu (2011), Bayesian Estimation of the Spatially Varying Completeness Magnitude of Earthquake Catalogs, Bull. Seismol. Soc. Am., 101, 1371-1385, doi: 10.1785/0120100223

Mogi, K., 1962. Magnitude-frequency relationship for elastic shocks accompanying fractures of various materials and some related problems in earthquakes. Bull. Earthquake Res. Inst. Univ. Tokyo, 40: 831-883.

Molnar, P. & Atwater, T. (1978), Interarc spreading and Cordilleran tectonics as alternates related to the age of subducted oceanic lithosphere. Earth Planet. Sci. Lett. 41, 330–340.

Nanjo, K. Z., N. Hirata, K. Obara, and K. Kasahara (2012), Decade-scale decrease in b value prior to the M9-class 2011 Tohoku and 2004 Sumatra quakes, Geophys. Res. Lett., 39, L20304, doi:10.1029/2012GL052997.

Nanjo, K. Z., T. Ishibe, H. Tsuruoka, D. Schorlemmer, Y. Ishigaki, and N. Hirata (2010a), Analysis of the Completeness Magnitude and Seismic Network Coverage of Japan, Bull. Seismol. Soc. Am., 100, doi:10.1785/0120100077
Nazareth, Julie J. and Egill Hauksson, 2004, The Seismogenic Thickness of the Southern California Crust, Bulletin of the Seismological Society of America, v. 94, p. 940-960, doi:10.1785/0120020129

Nishikawa, T., and S. Ide (2014), Earthquake size distribution in subduction zones linked to slab bouyancy, Nat. Geosci., 7, 904–908, doi:10.1038/NGEO2279.

Ogata, Y., and K. Katsura (1993), Analysis of temporal and spatial heterogeneity of magnitude frequency distribution inferred from earthquake catalogues, Geophys. J. Int., 113, 727-738.
Ogata, Y., and K. Katsura (2006), Immediate and updated forecasting of aftershock hazard, Geophys. Res. Lett., 33, doi:10.1029/2006GL025888.
Okal, E. A., and Romanowicz, B. A. (1994), On the Variation of b-values with Earthquake Size, Phys. Earth Planet. Inter. 87, 55–76.

Pacheco, J. and L.R. Sykes, (1992), Seismic moment catalog of large shallow earthquakes, 1900 to 1989, Bulletin of the Seismological Society of America 82, 1306–1349.

Pisarenko, V.F., Lyubushin, A.A., Lysenko, V.B. & Golubeva, T.V., 1996. Statistical estimation of seismic hazard parameters—maximum possible magnitude and related parameters, Bull. seism. Soc. Am., 86, 691–700.

Pondrelli, S., A. Morelli, and E. Boschi (1995), Seismic deformation in the Mediterranean area estimated by moment tensor summation, Geophys. J. Int., 122, 938 – 952.

Pondrelli, S., A. Morelli, G. Ekström, S. Mazza, E. Boschi, and A. M. Dziewonski, 2002, European-Mediterranean regional centroid-moment tensors: 1997-2000, Phys. Earth Planet. Int., 130, 71-101, 2002

Raleigh, C.B., Healy, J.H., Bredehoeft, J.D., 1972. Faulting and crustal stress at Rangely, Colorado. In: Heard, H.C., Borg, I.Y., Carter, N.L., Raleigh, C.B. (Eds.), Flow and Fracture of Rocks. Geophysical Monograph Series. AGU, Washington, D.C., pp. 275–284.

Richter, C. F. (1958). Elementary Seismology, Freeman & Co., San Francisco.

Ringdal, F. (1975), On the estimation of seismic detection thresholds, Bull. Seismol. Soc. Am., 65, 1631-1642.

Ruff, L. & Kanamori, H. (1980), Seismicity and the subduction process. Phys. Earth Planet. Inter. 23, 240–252.

Ruff, L. & Kanamori, H. (1983), Seismic coupling and uncoupling at subduction zones. Tectonophysics 99, 99–117.

Rydelek, P.A., and I.S. Sacks, Testing the completeness of earthquake catalogs and the hypothesis of self-similarity, Nature, 337, 251-253, 1989.

Samowitz, I. R., and D. W. Forsyth (1981), Double seismic zone beneath the Mariana Island Arc, J. Geophys. Res., 86(B8), 7013–7021, doi:10.1029/JB086iB08p07013.

Scholz, C. and Cowie, P., (1990) Determination of total strain from faulting using slip measurements, Nature 346: 837-839

Scholz, C. H. (1968), The frequency-magnitude relation of microfracturing in rock and its relation to earthquakes, Bull. Seismol. Soc. Am., 58, 399–415.

Scholz, C. H. (2002). The Mechanics of Earthquakes and Faulting, 2nd edition, Cambridge University Press

Scholz, C. H. (2015), On the stress dependence of the earthquake b value. Geophys. Res. Lett., 42: 1399–1402. doi: 10.1002/2014GL062863

Scholz, C. H. & Campos (1995), J. On the mechanism of seismic decoupling and back arc spreading at subduction zones. J. Geophys. Res. 100, 22103–22115.

Schorlemmer D. Neri G. Wiemer S. Mostaccio A., (2003). Stability and significance tests for b-value anomalies: example from the Tyrrhenian Sea, Geophys. Res. Lett., 30, doi:10.1029/2003GL017335.

Schorlemmer, D., A. Christophersen, A. Rovida, F. Mele, M. Stucchi, and W. Marzocchi (2010a), Setting up an earthquake forecast experiment in Italy, Ann. Geophys., 53, doi:10.4401/ag-4844.
Schorlemmer, D., and J. Woessner (2008), Probability of detecting an earthquake, Bull. Seismol. Soc. Am., 98, doi:10.1785/0120070105
Schorlemmer, D., and S. Wiemer (2005), Microseismicity data forecast rupture area, Nature, 434(7037), 1086, doi:10.1038/4341086a.

Schorlemmer, D., S. Wiemer, and M. Wyss (2004), Earthquake statistics at Parkfield: 1. Stationarity of b values, J. Geophys. Res., 109, B12307, doi:10.1029/2004JB003234.

Schorlemmer, D., S. Wiemer, and M. Wyss (2005), Variations in earthquake-size distribution across different stress regimes, Nature, 437, 539–542, doi:10.1038/nature04094.

Schorlemmer, D., S. Wiemer, M. Wyss, and D. D. Jackson (2004), Earthquake statistics at Parkfield: 2. Probabilistic forecasting and testing, J. Geophys. Res., 109, B12308, doi:10.1029/2004JB003235.

Schurr, B., G. Asch, S. Hainzl et al. (2014), Gradual unlocking of plate boundary controlled initiation of the 2014 Iquique earthquake, Nature, 512, 299–302, doi:10.1038/nature13681.

Shi, Y. & Bolt, B. A. (1982), The standard error of the magnitude–-frequency b-value. Bull. Seismol. Soc. Am. 72, 1677–-1687.

Smith, W. D. (1981), The b-value as an earthquake precursor, Nature, 289, 136–139.

Spada, M., T. Tormann, S. Wiemer, and B. Enescu (2013), Generic dependence of the frequencysize distribution of earthquakes on depth and its relation to the strength profile of the crust, Geophys. Res. Lett., 40, 709–714, doi:10.1029/2012GL054198.

Stern, R. J., Subduction zones, Rev. Geophys., 40 (4), 1012, doi:10.1029/2001RG000108, 2002.

Stern, R.J., Fouch, M.J., and Klemperer, S.L., (2003), An overview of the Izu Bonin-Mariana subduction factory, in Eiler, J., ed., Inside the Subduction Factory: American Geophysical Union Geophysical Monograph 138, p. 175–222

Storchak, D.A, Di Giacomo, D., Bondár, I., Engdahl, E.R., Harris, J., Lee, W.H.K., Villaseñor, A., and Bormann, P., (2013). Public Release of the ISC–GEM Global Instrumental Earthquake Catalogue (1900–2009). Seism. Res. Lett., 84, 5, 810-815.

Suzuki, Z. (1959). A statistical study on the occurrence of small earthquakes, Sci. Rept. Tohoko Univ. Geophys. Ser. 11, 10-54.

Taylor, D. A., J. A. Snoke, I. S. Sacks, T. Takanami (1990). Nonlinear frequency magnitude relationship for the Hokkaido corner, Japan, Bull. Seism. Soc. Am. 80, 340–353.

Tormann, T., Enescu, B., Woessner, J., Wiemer, S. (2015), Randomness of megathrust earthquakes implied by rapid stress recovery after the Japan earthquake, Nat. Geosci., 8:152–158., doi:10.1038/ngeo2343.

Tormann, T., S. Wiemer, and A. Mignan (2014), Systematic survey of high-resolution b value imaging along Californian faults: inference on asperities, J. Geophys. Res. Solid Earth, 119, 2029–2054, doi:10.1002/2013JB010867.

Tormann, T., S. Wiemer, and J. L. Hardebeck (2012), Earthquake recurrence models fail when earthquakes fail to reset the stress field, Geophys. Res. Lett., 39, L18310, doi:10.1029/2012GL052913.

Tormann, T., S. Wiemer, B. Enescu, and J. Woessner (2016), Normalized rupture potential for small and large earthquakes along the Pacific Plate off Japan, Geophys. Res. Lett., 43, 7468–7477, doi:10.1002/2016GL069309.

Tormann, T., S. Wiemer, S. Metzger, A. J. Michael, and J. L. Hardebeck (2013), Size distribution of Parkfield's microearthquakes reflects changes in surface creep rate, Geophys. J. Int., 193, 1474–1478, doi:10.1093/gji/ggt093.

Turcotte, D. L., & Schubert, G. (2002), Geodynamics- Second Edition. Cambridge, UK: Cambridge University Press

Utsu, T. (1965), A method for determining the value of b in a formula log n = a – bM showing the magnitude-frequency relation for earthquakes, Geophys. Bull., Hokkaido Univ., Hokkaido, Japan, 13, 99-103 (in Japanese).

Utsu, T. (1999), Representation and analysis of the earthquake size distribution: A historical review and some new approaches, Pure Appl. Geophys., 155, 509–535.

Uyeda, S. & Kanamori, H. Back-arc opening and the mode of subduction. J. Geophys. Res. 84, 1049 (1979).
Uyeda, S., (1982), Subduction zones: An introduction to comparative subductology, Tectonophysics, 81 (3–4), pp. 133–159, doi.org/10.1016/0040-1951(82)90126-3.

Vannucci, G., Pondrelli, S., Argnani, A., Morelli, A., Gasperini, P. and Boschi, E. (2004), An Atlas of Mediterranean seismicity, Annals of Geophysics 47, 1, 247-306.

Warren, N.W. and Latham, G.V., 1970. An experiment study of thermal induced microfracturing and its relation to volcanic seismicity. J. Geophys. Res., 75: 4455-4464.

Wessel, P. and W. H .F. Smith (1991): Free software helps map and display data, EOS, Trans. Am. Geophys. Un., 72, 441.

Westaway, R. (1992), Seismic moment summation for historical earthquakes in Italy: Tectonic implications, J. Geophys. Res., 97(B11), 15437–15464, doi:10.1029/92JB00946

Wiemer S. (2001), A Software Package to Analyze Seismicity: ZMAP, Seism. Res. Lett., 72, 373-382.

Wiemer S., Wyss M., (2000), Minimum magnitude of complete reporting in earthquake catalogs: examples from Alaska, the Western United States, and Japan, Bull. seism. Soc. Am. , 90, 859–869.

Wiemer, S., and D. Schorlemmer (2007), Alm: An asperity-based likelihood model for california, Seismol. Res. Lett., 78, 134-140.

Wiemer, S., and J. P. Benoit (1996), Mapping the b-value anomaly at 100 km depth in the Alaska and New Zealand subduction zones, Geophys. Res. Letts., 23, 1557–1560, doi: 10.1029/96GL01233.

Wiemer, S., and M. Wyss (1997), Mapping the frequency-magnitude distribution in asperities: An improved technique to calculate recurrence times?, J. Geophys. Res., 102(B7), 15115–15128, doi:10.1029/97JB00726.

Wiemer, S., and Wyss, M., (2002). Mapping spatial variability of the frequency-magnitude distribution of earthquakes, Adv. Geophys. 45, 259–302.

Wiemer, S., D. Giardini, D. F◎ah, N. Deichmann, and S. Sellami (2009), Proababilistic seismic hazard assessment for Switzerland: best estimates and uncertainties, J. of Seismology, doi:10.1007/s10950-008-9138-7.

Wiemer, S., McNutt, S.R. and Wyss, M. (1998), Temporal and three-dimensional spatial analysis of the frequency-magnitude distribution near Long Valley caldera, California, Geophys. J. Int., 134, 409–421.

Wilcoxon, Frank (1945). "Individual comparisons by ranking methods" Biometrics Bulletin. 1 (6): 80–83.

Woessner, J., and S. Wiemer (2005), Assessing the quality of earthquake catalogs: Estimating the magnitude of completeness and its uncertainties, Bull. Seismol. Soc. Am., 95(2), 684–698, doi:10.1785/0120040007.

Wyss, M. (1973), Towards a physical understanding of the earthquake frequency distribution. Geophys. J. R. Astron. Soc. 31, 341–-359.

Wyss, M. (2001), Locked and creeping patches along the Hayward Fault, California. Geophys. Res. Lett., 28: 3537–3540. doi:10.1029/2001GL013499.

Wyss, M. F. W. Klein, K. Nagamine, and S. Wiemer (2001), Anomalously high b-values in the south flank of Kilauea volcano, Hawaii: evidence for the distribution of magma below Kilauea's east rift zone, J. Volc. Geotherm. Res., 106, 23–37, 2001, doi: 10.1016/S0377-0273(00)00263-8.

Wyss, M., A. Hasegawa and J. Nakajima (2001), The source and path of magma for volcanoes in the subduction zone of northeastern Japan, Geophys. Res. Letts., 28, 1819–1822, doi: 10.1029/2000GL012558.

Wyss, M., A. Hasegawa, S. Wiemer, and N. Umino (1999), Quantitative mapping of precursory seismic quiescence before the 1989, m7.1 Osanriku earthquake, japan, Annali Di Geofisica, 42, 851-869

Wyss, M., D. Schorlemmer, S. Wiemer, (2000) Mapping asperities by the minima of local recurrence time: San Jacinto-Elisnore fault Zones, J. Geophys. Res., 105, 7829-7844

Yang, W., E. Hauksson and P. M. Shearer, Computing a large refined catalog of focal mechanisms for southern California (1981 - 2010): Temporal Stability of the Style of Faulting, Bull. Seismol. Soc. Am., June 2012, v. 102, p. 1179-1194, doi:10.1785/0120110311, 2012.

Zoback, M. D. (2007). Reservoir Geomechanics, University Press, Cambridge

Zoback, M. D., and J. Townend (2001), Implications for hydrostatic pore pressures and high crustal strength for the deformation of intraplate lithosphere, Tectonophysics, 336, 19–30.

Zoback, M. L., and M. D. Zoback (2007), Lithospheric stress and deformation, in Treatise on Geophysics, edited by A. B. Watts, pp. 253–274, Elsevier, Amsterdam.

Zoback, M., Hickman, S. & Ellsworth, W. (2010) Scientific drilling into the San Andreas fault zone. Eos Trans. Am. Geophys. Union 91, 197–198.